

Structure, Aggregation and Characterization of Nanoparticles

Glenn A. Waychunas

*Geochemistry Department
Earth Sciences Division, MS 70-108B
E.O. Lawrence Berkeley National Laboratory
One Cyclotron Road
Berkeley, California 94720*

INTRODUCTION

Structural aspects of natural nanomaterials

A large number of mineral species occur only as micron-sized and smaller crystallites. This includes most of the iron and manganese oxyhydroxide minerals, and other species whose formation processes and growth conditions limit ultimate size. Microscopic investigation of these species generally reveals sub-micron structure down to the nanometer level, including evidence of aggregation, agglomeration and assembly of nanometer units into larger crystals and clots. The bulk of studies in the literature dealing with nanoparticle structure and growth deal with metals, silicon, and other semiconductor materials. A great deal of attention has been given to the electronic properties of such solids, owing to both new commercial applications and new fundamental physics and chemistry tied to this area. Most applicable mineralogical or geochemical studies have not addressed the same issues, instead being more concerned with relatively bulk chemical properties. Very little has been done to understand how natural nanoparticulates (and related types of natural nanomaterials) form, how their microstructure is related to the growth process, and how their structure varies from larger crystallites or bulk material of the same composition. Magnetic and electronic properties of natural nanomaterials are similarly understudied.

In this chapter aspects of nucleation, aggregation and growth processes that give rise to specific microstructures and forms of nanomaterials are considered. Next the way in which the surface structure of nanoparticulates may differ from the interior, and how physical structure may be modified by reduced particle size is examined. The various techniques by which nanoparticle structure, size, microstructure, shape and size distribution are determined are then considered with examples. Finally some of the outstanding problems associated with nanoparticle structure and growth are identified, emphasizing natural processes and compositions.

Definitions

Naturally occurring nanomaterials exist in a variety of complex forms. In this chapter a short set of definitions will be stated for clarity. *Nanocrystals* are single crystals with sizes from a few nm up to about 100 nm. They may be aggregated into larger units with a wide spectrum of microstructures. *Nanoparticles* are units of minerals, mineraloids or solids smaller in size than 100 nm, and composed of aggregated nanocrystals, nanoclusters or other molecular units, and combinations of these. *Nanoclusters* are individual molecular units that have well-defined structure, but too small to be true crystals. Al_{13} and Zn_3S_3 solution complexes are types of nanoclusters with sizes from sub nanometer to a few nm. *Nanoporous* materials are substances with pores or voids of nanoscale dimensions. These materials can be single crystals, such as zeolites or

molecular sieves with cage-like nanopores; amorphous materials with nanoscale voids; poorly crystalline solids with grain-boundary or defect pores; or composite materials. Some of the literature treats clay and similar layer minerals as nanoporous solids.

These categories of nanomaterials are useful due to the rather different physical behavior, growth and structure of each type. For example, nanoclusters are closely akin to molecules in terms of transport and reactive processes. Nanoparticles are somewhat like classical colloids, but in a smaller size regime. Nanoporous solids have unique abilities to encapsulate, bind and react with other nanoparticles and nanoclusters, as well as molecules. Nanocrystals can have relaxed or contracted lattices, and unusual reactivity relative to their larger counterparts.

Colloidal particles can have dimensions from small clusters of atoms up to about 10 μm in diameter. They are classically defined as any suspended fine particles in water. Hence smaller colloidal particles are the same as nanoparticles. In the formation of nanoparticles one often speaks of polymer and monomer units. *Monomers* refer to the smallest growth unit, either a single atom, ion or molecule. *Polymers* are units consisting of two or more monomers.

The *bulk* of a nanomaterial will refer to that portion that is not clearly defined as part of the surface, i.e., not within several atomic layers of the surface. This implies that 1-nm nanomaterials consist only of surface. *Surface volume* will refer to the volume of a nanocrystal or nanoparticle that is assumed to be part of the surface. The *habit* of a crystal is the particular external form that is presented within the options allowed by the point group symmetry. Common descriptive terms are tabular (tablet-like), cubic, acicular, and so forth. Occasionally, habits inconsistent with point group symmetry can occur from kinetic phenomena.

GROWTH AND AGGREGATION PROCESSES

Growth processes

The growth of nanomaterials is a rich field of research that can only be treated in a selective fashion in this chapter. The main concerns are the principle issues that determine formation and growth in the nanoscale range, how growth influences microstructure, the stability of particular sizes, shapes and phases, and structure-property relationships. Unlike most nanomaterials, natural nanomaterials can be formed by either inorganic or biologically-connected (enzymatic) processes. In some cases, the same composition nanomaterials can be formed by either pathway.

Inorganic vs. organic (enzymatic)

Inorganic growth processes generally are treated as near equilibrium, i.e., at low supersaturation in a solution, or at moderate undercooling in a melt-solid system. This situation can give rise to slow growth and a decreased rate of nucleation. Hence it is ideal for the formation of large crystallites. On the other hand, extreme undercooling or sudden generation of high supersaturation levels can lead to very high nucleation rates creating small crystallites or particulates. In non-homogeneous systems, e.g., those where nanomaterials are formed on substrates, the nanomaterial-substrate interface can act to enhance nucleation rate, or influence local concentration (and thus supersaturation) due to surface complexation. In contrast to these processes, enzymatic pathways for nanomaterial growth may take place far from equilibrium, and often under conditions for which nanoparticle growth could otherwise not occur. For example, oxidation of Fe^{2+} in natural waters is much more rapid in the presence of specific bacteria. The organism *Thiobacillus ferrooxidans* can increase this rate by as much as six orders of magnitude

(Singer and Stumm 1970). The oxidized iron can precipitate not only in the surroundings of the bacteria, but also on the bacteria surfaces or exopolymers, so that both catalysis and heterogeneous nucleation effects obtain. Analogous reactions occur for dissolved manganese, oxidizing it into extremely insoluble Mn^{4+} , and for many other metals including uranyl species (Suzuki and Banfield 1999). Further, the process may be controlled by the electron transfer at the cell enzyme/solution interfaces, to restrict growth rate even perhaps to atom by atom. These differences in growth pathway can potentially be utilized to prepare nanomaterials of unique composition, structure and properties.

NUCLEATION AND GROWTH

Classical nucleation theory (CNT)

Classical theory assumes that the formation of a condensed phase commences with the development of a “critical nucleus”. This nucleus is assumed to form by random fluctuations from smaller units, generally single atoms or molecules. Once formed this nucleus has a greater probability of growing further than of losing mass, and the system can enter into a growth stage.

The nucleus is assumed to have the same structure, density, etc. as the bulk phase, and have the same interaction energies with adjacent phases (surface tension, etc.). This conception has proved valuable in general, but a few of its assumptions are difficult to prove or incorrect on the molecular level (Talanquer and Oxtoby 1994). Other assumptions are practically impossible to test (ten Wolde and Frenkel 1997), as critical nucleus formation is a fleeting event that may not be amenable to any direct imaging method. However, as nanoparticles are of the same size domain as theoretical critical nuclei, an understanding of the nucleation process is essential to defining and possibly controlling the pathways for nanoparticle formation.

Homogeneous nucleation

The classical model of random homogeneous nucleation is due to Volmer and Weber (1926) and Becker and Doring (1935), who developed a theory for the formation of nuclei of liquid droplets in supersaturated vapors. Figure 1 shows the free energy of formation for a given nucleus as a function of size and temperature. Using spherical particles of radius r , the free energy is given by:

$$\Delta G = 4/3 \pi r^3 \Delta g + 4\pi r^2 \sigma \quad (1)$$

where Δg is the free energy change per unit volume of the nucleus, and σ is the free energy per unit area of the interface. It is clear that if Δg is negative (the case for supersaturation) then the free energy change is a maximum for some size nucleus depending on the temperature. The lower the temperature the smaller this nucleus, and the smaller the needed change in free energy to stabilize it. If the temperature-dependence of the interface energy is neglected, the critical values $r = -2\sigma/\Delta g$, and $\Delta G = 16\pi\sigma^3/3(\Delta g)^2$ are obtained by solving the derivative $[d(\Delta G)/dr = 0]$ of Equation (1). With a few other assumptions, it is possible to quantify the number of critical nuclei and the rate of nucleation for this model (see e.g., Raghavan and Cohen 1975). We assume that the addition of a single atom defines the boundary between a sub- and super-critical nucleus, and that we can use Maxwell-Boltzmann statistics. If the total number of atoms be N_T , then the number of critical-sized nuclei is approximately:

$$N = N_T \exp(-\Delta G/kT) \quad (2)$$

If the largest subcritical nucleus is surrounded by s atoms in the system, the frequency ν_1

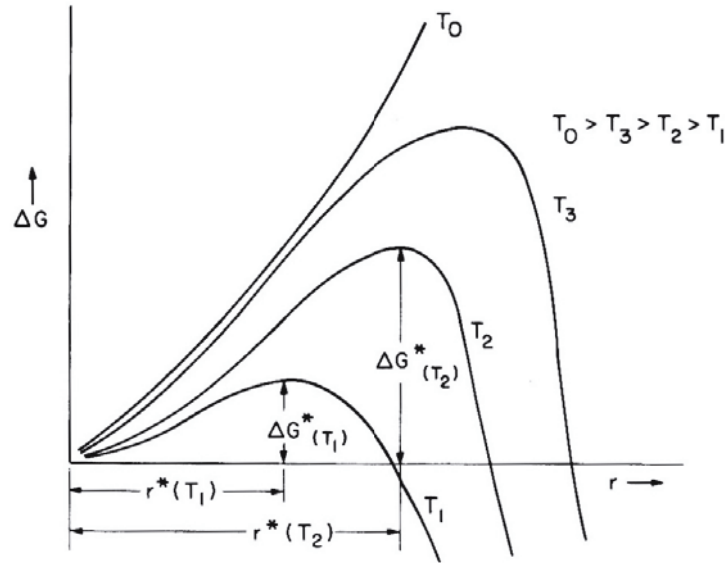


Figure 1. Free energy required for the stability of a critical nucleus. At the lowest temperature both the energy barrier and the critical radius for a nucleus is the smallest, and both increase with increasing temperature. At some temperature T_0 , the critical radius is too large for a stable nucleus to form. This corresponds to a system that is not supersaturated. After Raghaven and Cohen (1975).

for which these atoms can join the particle is:

$$v_1 = sv \exp(-\Delta G_D/kT) \quad (3)$$

where v is the frequency of lattice vibrations and ΔG_D is the free energy for atomic diffusion across the interface. The nucleation rate is then (events per unit time and unit volume):

$$I = N_T s v \exp[-(\Delta G + \Delta G_D)/kT] \quad (4)$$

Heterogeneous nucleation

Clem and Fisher (1958) use a similar treatment as above to derive the solid state nucleation kinetics for new phases at grain boundaries. They neglect orientation of the critical nucleus with respect to the host, strain energy, and coherency effects. Nucleation at the grain boundary interface removes boundary energy. Their treatment yields the following critical values:

$$R = -2\sigma_{\alpha\beta}/\Delta g \quad (5)$$

$$r = -2\sigma_{\alpha\beta}(\sin\theta)/\Delta g \quad (6)$$

$$\Delta G = 8\pi\sigma_{\alpha\beta}^3(2-3\cos\theta+\cos^3\theta)/3(\Delta g)^2 \quad (7)$$

where R is the radius of curvature of the spherical surfaces of the nucleus, 2θ is the included angle of the nucleus edge as controlled by surface tension (Fig. 2), $\sigma_{\alpha\beta}$ is the matrix-nucleus interfacial energy, and $\sigma_{\alpha\beta}$ is the grain boundary interfacial energy.

Using assumptions as before a nucleation rate can be derived:

$$I_{\text{hetero}} = \sum N_i v \sigma_i \exp[-(\Delta G_i + \Delta G_D)/kT] \quad (8)$$

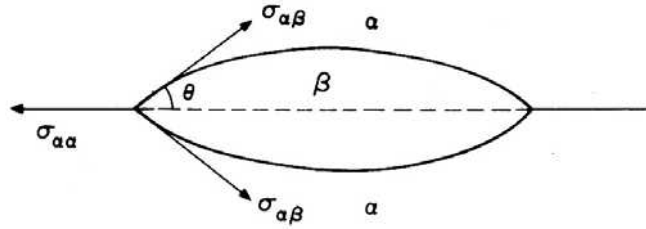


Figure 2. Model geometry for the nucleation of a new phase at a grain boundary. After Raghaven and Cohen (1975).

where N_i is the number of sites per unit volume having nucleation barrier ΔG_i . The main difference between Equations (4) and (8) is that N_i is orders of magnitude smaller than N_T , and ΔG_i is usually significantly smaller than ΔG . In general the exponential dominates so that I_{hetero} is much greater than I .

PROBLEMS WITH CLASSICAL MODELS

These classical approaches (later modified with energy terms including strain, coherency with a substrate, temperature-dependence, interface volume changes, and so on) all assume that random fluctuations somehow create the subcritical nucleus, and that the step from subcritical to supercritical is the addition of a single atom. However no aspect of classical theory takes into account molecular level phenomena. The theory is thus a macroscopic theory, and hence it is not surprising that different types of molecular bonding in physical systems gives rise to large deviations from classically predicted nucleation rates (Talanquer and Oxtoby 1994; Marasli and Hunt 1998; Auer and Frenkel 2001).

Dynamical nucleation processes: Smoluchowski's approach

One of the assumptions of CNT is that formation of the critical nucleus occurs by aggregation of monomer units to the sub-critical nucleus, i.e., the concentration of polymer clusters below critical nucleus size is negligible. This neglects cluster-cluster aggregation as a nucleation process, which seems to go against intuition. However Alexandrowicz (1993) has shown via scaling theory that, given reasonable assumptions, monomer addition/subtraction is by far the most important process. An entirely different way of considering nucleation utilizes a summation over all of the competing processes that can produce critical-size nuclei and further growth. This approach was first suggested by Smoluchowski (1917), and is generally employed today in aggregation processes. This approach yields direct insight into the dynamical aspects of nucleus formation as it considers each discrete type of aggregation/disaggregation rate (from atom and molecule monomers adding to a given size cluster, to larger cluster addition/breakup). It has been termed a "kinetic" approach to nucleation and growth as discrete energies and thermodynamic equilibria are replaced by probabilistic terms for cluster formation (Hetteema and McFeaters 1996). Hence the concept of a critical nucleus is replaced by particle size distributions as a function of time.

Smoluchowski's equation in its simplest form describes rates of cluster formation and reduction:

$$\frac{dn_k}{dt} = \frac{1}{2} \sum_{i+j=k} K(i, j)n_i n_j - n_k \sum_{i=1}^{\infty} K(i, k)n_i$$

The first term represents the rate of creation of clusters of a given size from smaller

clusters, while the second term represents the loss of such clusters via reactions with other clusters. The equation is thus a description of a set of coupled rate equations. The K terms are reaction rate coefficients and may themselves be complex mathematical expressions. For example, cluster rearrangement, fragmentation into multiple smaller clusters, and sticking probability can all be embedded in a given K term. As fractal theory can be used to describe the results of aggregating clusters (see below), the K terms are often referred to as “kernels” in keeping with fractal notation. The scaling behavior of kernels as a function of cluster size is a focus of such treatments.

Classical growth mechanisms vs. aggregation processes

The contrasting treatments of nucleation have consequences for the initial formation of nanoscale particles. If CNT is accurate on a molecular scale, then nanoparticles below the critical nucleus size would be difficult to preserve. Attachment of molecules to a subcritical nanoparticle surface could be used to alter surface energy and produce stability. Still other technological tricks could be used to reduce the degradation rate of metastable nanoparticles, e.g., fast trapping in noble gas solids. But CNT allows for the formation of a narrow size distribution of nanoparticles if formation conditions can be controlled. On the other hand, aggregation processes would make it difficult to prepare nanoparticles with a narrow size distribution, let alone shape, even through the suitable adjustment of reaction rates. The size distribution is a crucial issue in any description of crystal growth via aggregation, as typical processes of self assembly and superlattice formation require building units of nearly identical size and shape. However, subcolloidal aggregation of nanoclusters to form zeolites (Nikolakis et al. 2000) has been described and modeled, and superlattice formation of metallic clusters has been described in several systems (e.g., Sun and Murray 1999). An important concept is *oriented aggregation* of nanoparticles, which allows for growth without recrystallization on a local scale. This process has been studied in detail by Banfield and co-workers (Banfield et al. 2000; Penn and Banfield 1998; Zhang and Banfield 2000)).

Classical growth mechanisms and laws

Much as CNT assumed monomer attachment, most classical theories of crystal growth assume that material is added to a growing crystal face essentially atom-by-atom (Fig. 3). The most common type of growth is layer-by-layer growth (also called Frank-Van der Merwe growth in cases of epitaxy (Zangwill 1988)). In this type of growth the energy reduction by the nucleation of another layer is small compared to monomer attachment within a layer, e.g., if forming a new layer forms only a single bond, while intralayer attachment forms 2 or more. Hence new layers are unlikely to start until underlying ones are essentially complete. A modification of this type of growth occurs if there is a screw dislocation exiting at the surface of the growth face. In that case the layer need not be nucleated once growth is initiated. Many crystals grow by this sort of process (Fig. 4).

It is assumed in classical growth models that all added monomers are attached permanently and do not diffuse off into the fluid, solution or gas state once attached. In the layer-by-layer case a newly attached atom or molecule will diffuse along the layer surface until it finds the edge of the currently growing layer. It will then take a position corresponding to the maximum number of interatomic bonds that it can make. The layer will then fill in according to the trade off between surface diffusion rates, bonding energies and availability of multibond attachment sites. Although this type of growth is highly idealized, it is appropriate for many systems, and can predict growth variations produced by ionic strength variations, temperature, surface impurities and other factors.

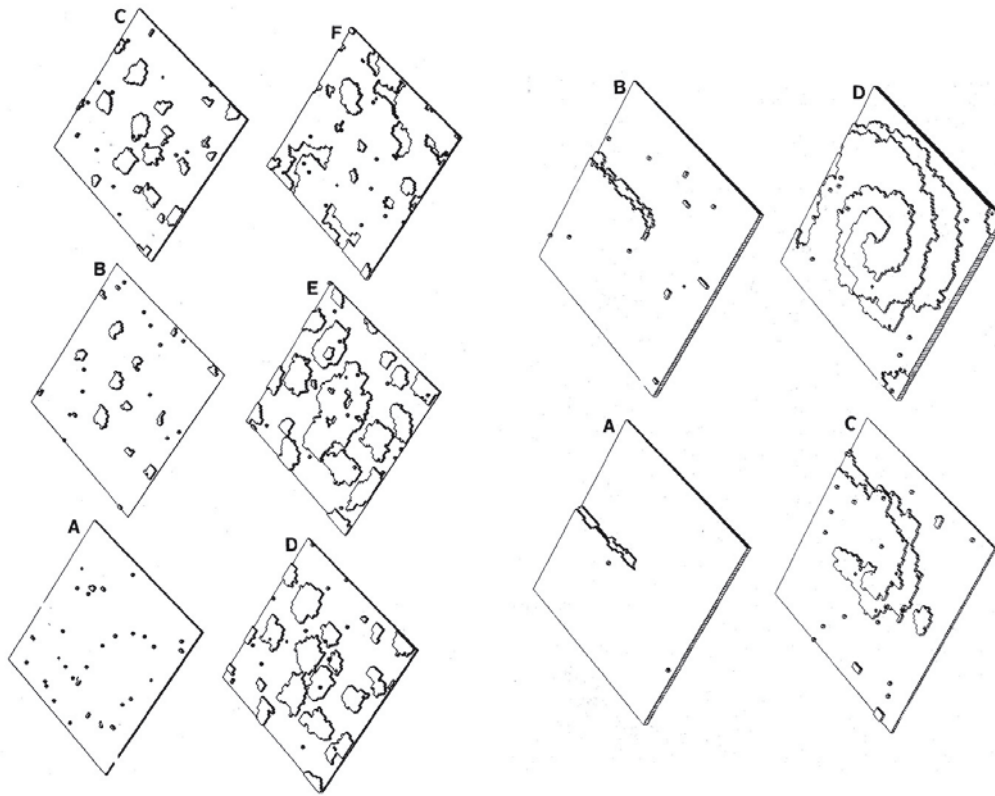


Figure 3. Left side: A to F, atom-by-atom simulated growth. New growth layer initiation occurs only when most sites at the edges of the layer are filled. Right side: A to D, growth at a surface having a screw dislocation. New layers continuously form. After Kirkpatrick (1981).

Growth topologies

The habit of a euhedral crystal is due to the rate at which particular faces grow, while the equilibrium faces (those nominally appearing initially on a crystal surface) are dictated by surface energy considerations. The greatest reduction in surface free energy will occur when the highest energy faces are reduced in size. This leads in general to the faster growth at high energy faces. Quite unusual crystal habits can be produced by rapid growth from supersaturated systems. In such case both equilibrium and kinetic considerations play a role in determining the type of crystallization. A construction which predicts equilibrium crystal faces based on a knowledge of surface energies and crystal symmetry is due to Wulff (1901), and has been examined in detail by Herring (1951). An example is shown in Figure 5. The basis of this construction is the minimum energy for the surface of a crystal with fixed volume (see Hartman 1973 for derivation), where it can be shown that:

$$\gamma_i = \lambda h_i \quad (10)$$

for each distinct crystallographic face with normal h_i and surface energy γ_i , and λ depending only on absolute volume. An equivalent formulation is:

$$\gamma_1:\gamma_2:\gamma_3:\dots = h_1:h_2:h_3:\dots \quad (11)$$

The construction takes the form (in two dimensions) of a plot of surface energies as a function of directions using polar coordinates. For each plane a normal is defined, and then a perpendicular line segment where the normal strikes the energy curve. The distance of a given surface plane from the crystal center of mass turns out to be proportional to the surface energy of that plane. For particular directions corresponding to

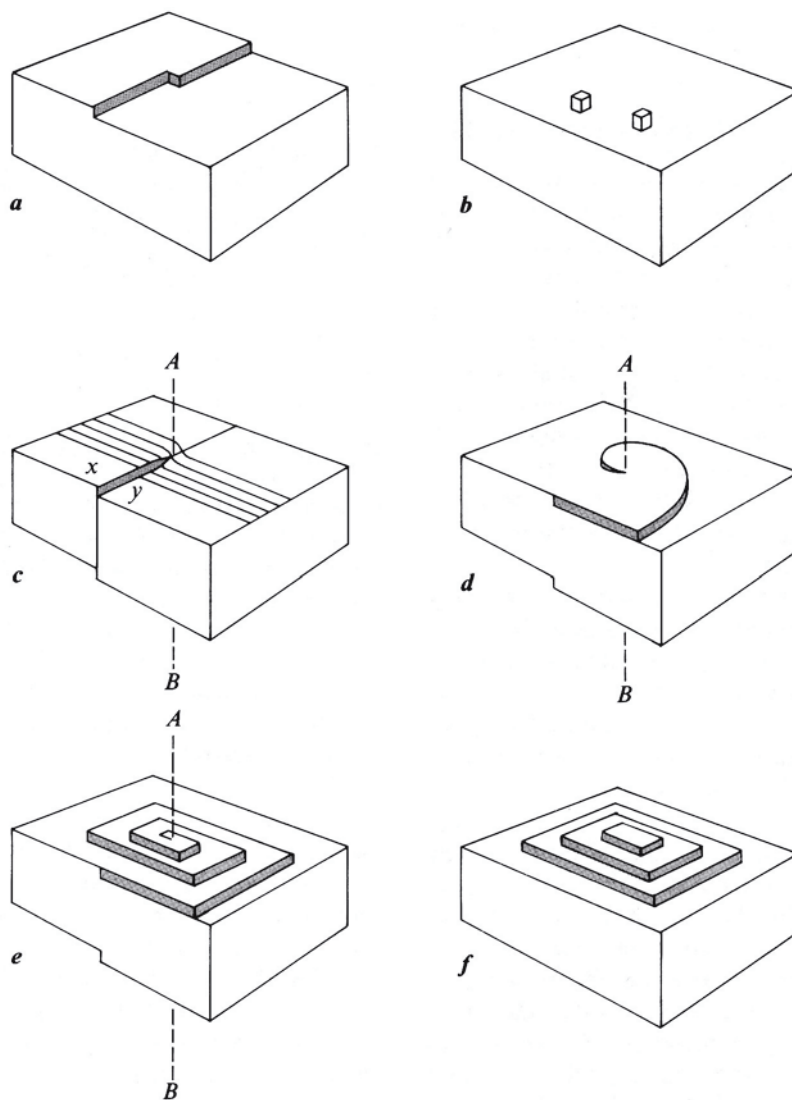


Figure 4. Surface growth features and habits. (a) Single layer growth showing lowest energy attachment site. (b) New layer nucleation via single atoms. (c) Presence of screw dislocation with axis normal to plane of surface. (d) Attachment sites on growing spiral. (e) Truncation of layers in response to anisotropic surface attachment energies. (f) ‘Pyramidal’ habit induced by spiral growth. From Zoltai and Stout (1984) with permission from Burgess Publishing Company.

principal crystal faces there are cusps in this plot. The smallest enclosed area within this line segment construction is the equilibrium crystal form. This process must be done in three dimensions to assuredly predict the equilibrium form for a lower symmetry crystal. The three dimensional Wulff plot can be sectioned to show the relative energy of faces in particular planes.

The competition between equilibrium and kinetic factors are shown in Figure 6 using two dimensional crystal growth. Three orientations of the Wulff construction sections are shown for crystals of CBr_4 -8% C_2Cl_6 along with corresponding dendritic growth patterns. Dendritic patterns develop when crystallization is too rapid to allow solvent to flow away from growing faces, or heat of crystallization to dissipate. Hence solvent can be trapped between elements of growth, or local heating raises solubility and decreases supersaturation. Two dimensional growth is markedly prone to complex patterning

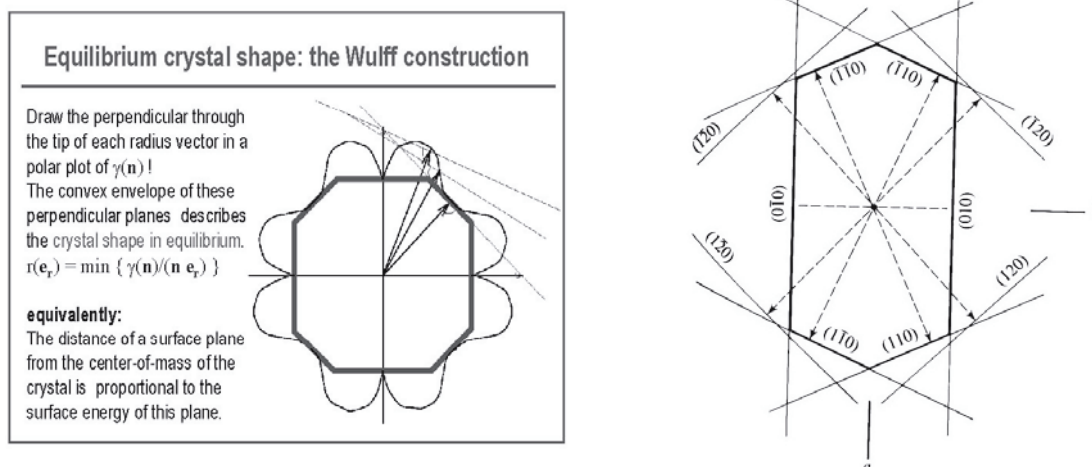


Figure 5. Wulff construction. Left: definition and general form of construction. Right: Wulff construction showing the equilibrium form of a forsterite crystal. After Zoltai and Stout (1984).

caused by various kinds of growth instabilities. For slow growth crystallites closely approximate Wulff construction predictions.

Skeletal crystals are examples of very rapid growth in particular directions most commonly due to crystallographically controlled screw dislocations and diffusion-limited growth conditions. These crystals fill in with lateral growth of dendrites as growth conditions change. Hopper-growth crystals, generally produced by vapor-solid crystallization, are formed when the edges of the crystal grow much faster than new nutrients can diffuse to the interior of the growth faces (Fig. 7). In dramatic contrast, crystals grown from a melt may have little exterior face development. An example are the “boules” produced when pulling single crystals from their melts in the Czochralski crystallization process. In this case the surface energy of different faces of the crystal is similar enough so that no face is favored for growth and the surface form is determined by diffusion rates in the melt. A final issue associated with Wulff constructions is the treatment of vicinal faces, i.e., planes slightly misoriented from a major (hkl) plane such as $(1\ 1\ 23)$ adjacent to (001) but tilted toward $(1\ 1\ 1)$. A detailed Wulff construction shows cusp structures corresponding to non-equilibrium but metastable suites of vicinal faces (Fig. 8). Cusps exist for all rational ratios of Miller indices. The vicinal faces will tend to reorganize into microfacet-terrace structures if $\gamma(\alpha) > [\gamma_0 \sin(\beta - \alpha) + \gamma_1 \sin \alpha] / \sin \beta$, where the microfacet inclination angle is β with surface energy γ_1 , and the terrace surface energy is γ_0 . (Fig. 8).

Inorganic vs. biologically produced crystallites

Hydrothermal, low temperature precipitation, and vapor deposition produce different crystal habits and sizes due to differences in growth rates, diffusion rates, and surface energy. Most Fe-Mn oxide-hydroxide phases are formed at low temperatures (below 100°C), but several are known to form under hydrothermal conditions (above 100°C and up to several kbars pressure). Larger crystals are produced from hydrothermal processes as transport is much more rapid, and solubility of the growing phase in the growth medium (solution) is high. The latter growth process can produce crystals up to 10 cm in size. Ice crystals (snowflakes) are the most commonly observed vapor deposition-produced natural phases. These usually show complex dendritic patterns caused by rapid

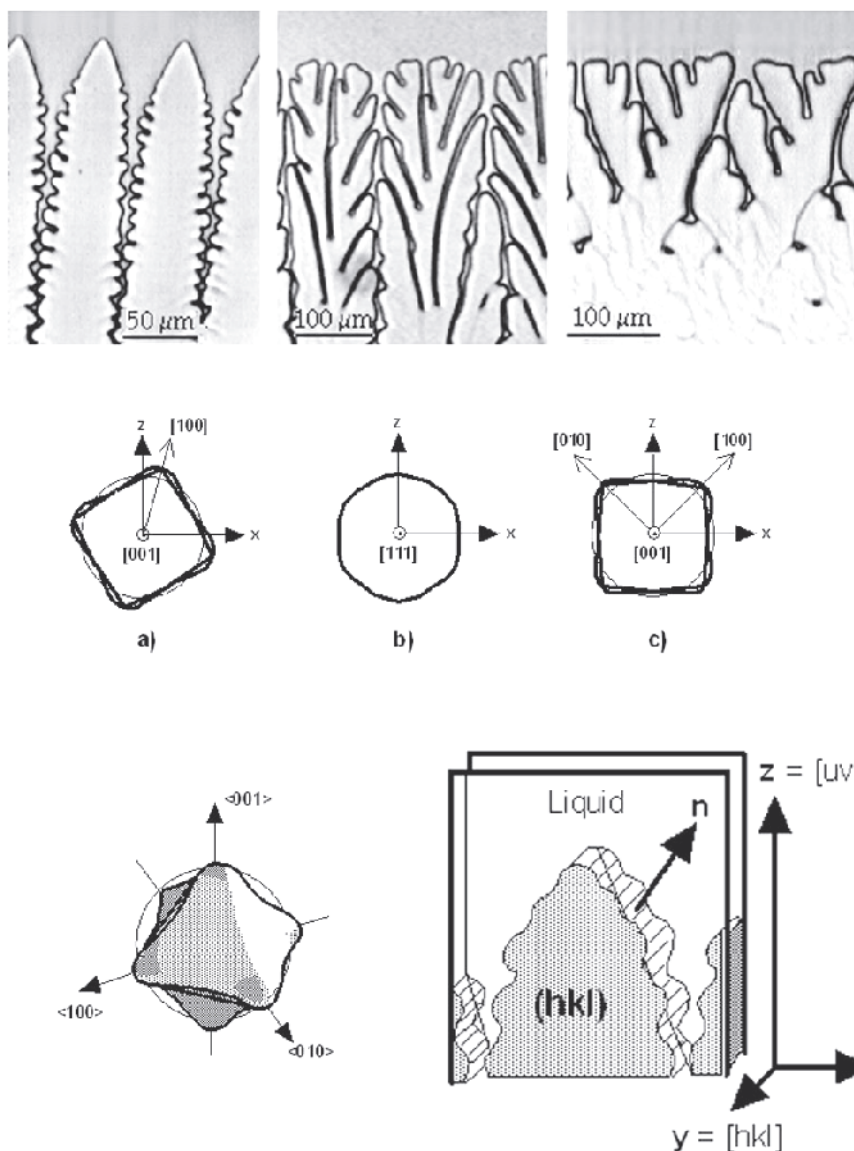


Figure 6. Dendrite formation. Top: Rapid two dimensional crystal growth in halocarbons. Different degrees of supersaturation (or undercooling) lead to fluctuations and limitations in nutrient supply to growing faces. Center: Wulff plots with orientation appropriate for each type of dendrite. Bottom left: three dimensional Wulff plot for this system. Bottom right: diagram of dendrite head structure showing equilibrium face and fluctuations in growth rate. From www.gps.jussieu.fr/engl/cell.htm.

growth as well as rapid changes in growth conditions during formation. Figure 9 shows microscopic images of synthetic vapor grown ice crystals.

In the case of biologically produced crystallites, low temperatures that normally restrict solubility of oxides, hydroxides and sulfides (except in strongly acidic solutions) can be affected by the presence of organic ligands and enzymes that alter the energy of growing crystal surfaces and increase or control solubility. This can result in modified habits, unusual growth patterns, complex microstructure, and dramatically increased crystallite size. An example from nature is the alteration of calcium carbonate growth to form complex microporous (or nanoporous) composite structures in the skeletons of sea organisms. This has been remarkably well modeled by the self assembly of liquid crystal materials, leading to suggestions that suitably surfactant-controlled CaCO_3 nanocrystal

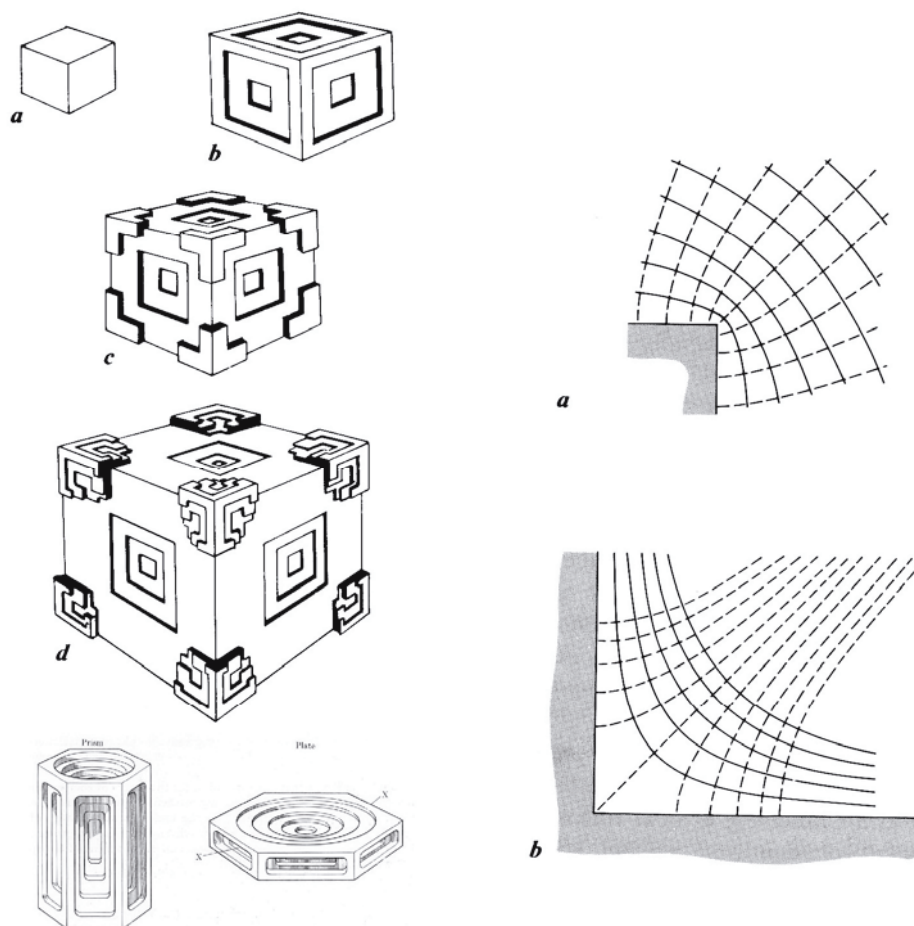


Figure 7. Hopper growth. Left: (a-d) successive growth stages with relatively slow nutrient transport to face centers. This type of growth is very common in halite and fluorite. Left bottom: two examples of hopper growth in ice crystals. Right: Flow density maps for nutrient transport near corners and reentrant angles. Highest flow is for closest grid spacings. From Zoltai and Stout (1984) with permission from Burgess Publishing Company.

growth could produce such structures in the laboratory (McGrath 2001). Another example is the development of iron oxyhydroxide nanoparticle aggregates formed via microorganism-catalyzed iron oxidation (Banfield et al. 2000). In this case nucleation of organized aggregates with well-defined nanocrystallite-nanocrystallite orientation occurs within a mass of randomly oriented nanoparticles. This suggests an initial assembly of nanocrystals by rotation and subsequent surface attachment when favorable orientations are presented. Under certain conditions several stages of such assembly may occur, allowing successively larger crystalline grains to form without a continuous classical growth process.

As inorganic crystal surfaces, growth patterns and growth rates can be strongly affected by organic and trace inorganic surface species, it is not fanciful to imagine the eventual intentional construction of inorganic structures with practically any desired degree and dimensionality of nanoporosity, density, surface area and shape.

How do these growth considerations apply to nanoparticles and nanocrystals?

Examples of the crystal forms of several types of natural and synthetic nanocrystals are shown elsewhere in this volume. Due to their small size, diffusion even through the

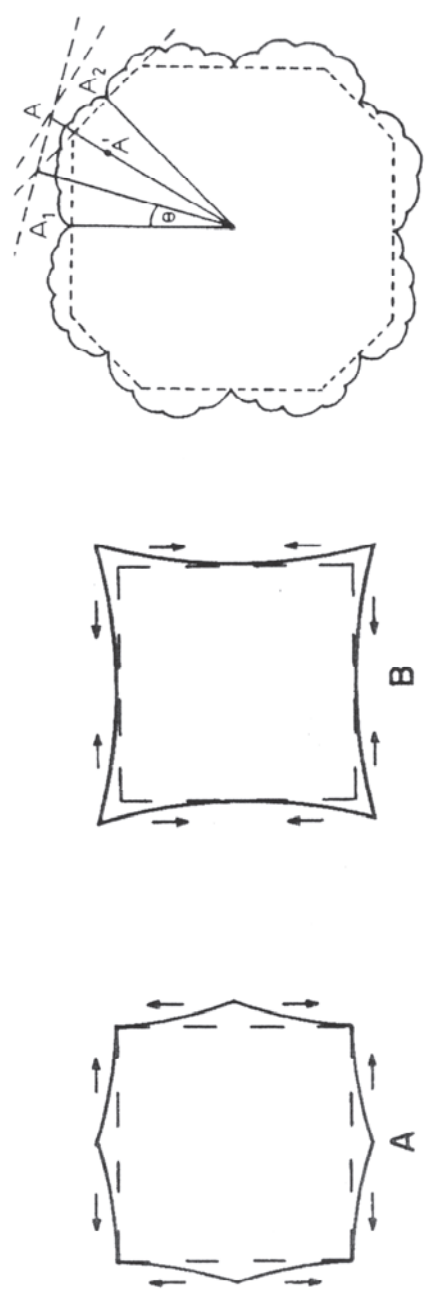
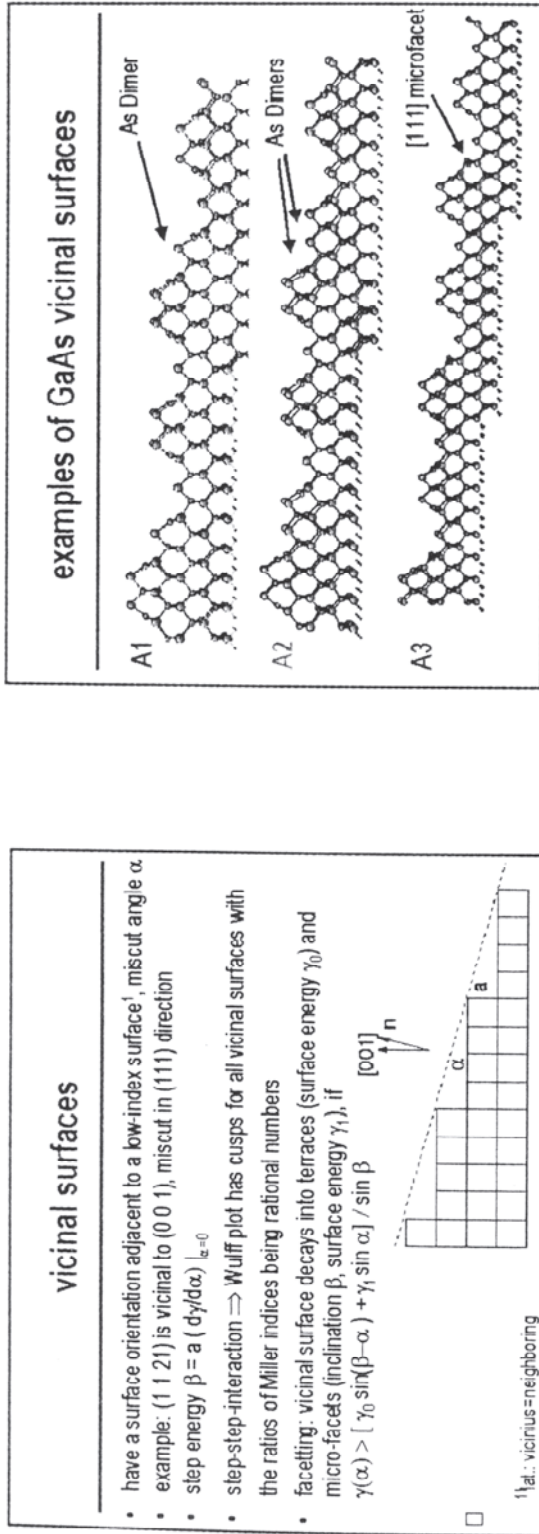


Figure 8. Top right: Definition of vicinal faces. Bottom right: Development of vicinal faces due to nutrient flow. Bottom left: Wulff construction showing possible metastable low angle faces near principle directions, A_1 and A_2 . From www.fh-berlin.mpg.de/th/member/kratzer_p.html.

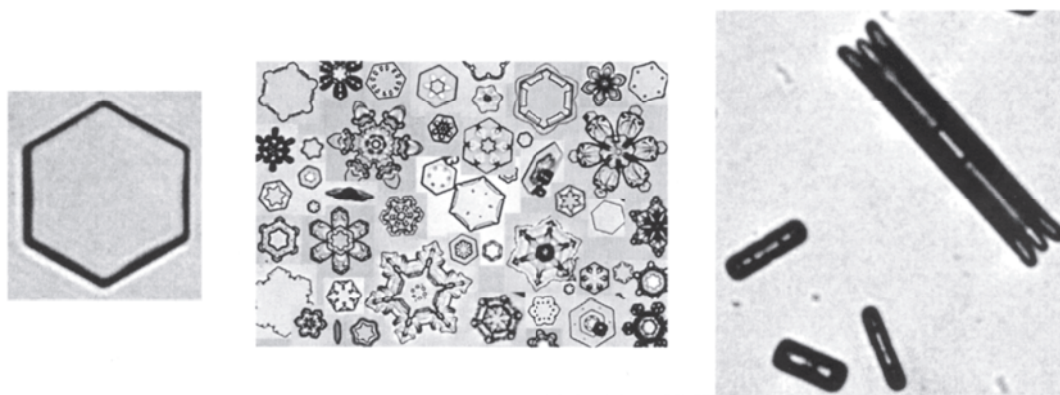


Figure 9. Habits for ice crystals grown under slightly different temperature (supersaturation) conditions. Left: perfect hexagonal crystals grown at low supersaturation. Right: rod-like hopper crystals grown at high supersaturation. Middle: Mosaic of various kinds of ice crystals with varying degrees of supersaturation and changes in conditions during growth. Crystals range from tens to hundreds of microns in diameter. From www.its.caltech.edu/~atomic/snowcrystals/.

interior of a nanocrystal ought to be rapid. Hence for individual nanocrystals, dendritic or other diffusion-limited forms should either not form, or be quickly converted into more stable surfaces. However, alteration of growth conditions to enhance surface energy anisotropy could conceivably be done to dramatically alter nanocrystal habits. On the other hand, the nature of well-defined surface terraces breaks down as nanocrystal diameter decreases. The surface can be considered in the small size limit as consisting only of microfacets. A complicating aspect of natural nanocrystals is that the surfaces will be in contact with an aqueous growth solution, and many types of surface species or impurities will be present. This will tend to affect surface energy and could lead to selective poisoning of particular face or surface feature development. All of these aspects present opportunities and challenges for the controlled development of special nanocrystal habits suited for particular chemical or environmental applications.

AGGREGATION MECHANISMS

The alternative to classic growth mechanisms is growth by aggregation reactions. In this case growth occurs from the attachment of clusters of atoms, critical nuclei, or larger units. A large body of research has been developed that explores the many diverse types of aggregation motifs and mechanisms. We have already noted the Smoluchowski approach to growth kinetics, and this formalism is sufficiently flexible to model many types of aggregation behavior. Before treating this further we now introduce other topics that will be of use in discussing surface structure and nanoparticle properties later in the chapter, and which clarify aspects of aggregation behavior.

Particle-particle interaction forces

Aggregation occurs because of a net attractive forces between particles. Besides varying in type, these forces also have specific ranges of action. A most thorough and approachable summary of all types of intermolecular and surface forces has been compiled by Israelachvili (1992). Here we briefly discuss only the most important forces on mineralogical nanoparticles: Covalent bonding, electrostatic interactions, dipole-charge, dipole-dipole, van der Waals and hydrophobic. Table 1 shows a comparison of these forces. The range of the force is defined as the distance where the force falls to kT . Interaction energies are given in kJ/mol for a vacuum interaction, unless otherwise indicated. *Covalent* forces are the strongest binding forces between atoms, but they have a short range as direct orbital overlap is required. Hence aggregation is only indirectly connected with covalent forces through particle-particle binding via sorbed molecular

Table 1. Interaction forces.

<i>Interaction</i>	<i>Energy (vacuum)</i>	<i>Directionality</i>	<i>Range (nm)</i>	<i>Example</i>
Covalent	100-900 kJ/mol	high	0.1-0.2	C-H (CH ₄) [430] Si-O (Silicates) [370] C=O (HCHO) [690]
Coulombic	100-1000 kJ/mol	zero	100	NaCl [880] Na ⁺ Cl ⁻ in water [11.2]
Dipole-charge (fixed)	30-400 kJ/mol	high	0.5	Na ⁺ H ₂ O [1.2] Mg ²⁺ H ₂ O [3.2]
Dipole-dipole (fixed)	up to ~200 kJ/mol	high	0.4	O ⁻ H ⁺ O ⁻ H ⁺ [2.6]
H Bond	10-40 kJ/mol	moderate	0.2	OH ⁻ ··OH [0.5]
Van der Waals ¹				
<i>Dipole-dipole (free rotation/ Keesom or orientation force)</i>	0-101 10 ⁻⁷⁹ Jm ⁶	weak	0.4	H ₂ O-H ₂ O [96] HCl-HCl [11] CH ₃ Cl-CH ₃ Cl [101]
<i>Dipole-induced dipole (free rotation/Debye or induction force)</i>	0-32 10 ⁻⁷⁹ Jm ⁶	weak	0.4	H ₂ O-H ₂ O [10] HCl-HCl [6] CH ₃ Cl-CH ₃ Cl [32]
<i>Induced dipole-induced dipole (London or dispersion force)</i>	2-400 10 ⁻⁷⁹ Jm ⁶	weak	0.2-10	CH ₃ Cl-CH ₃ Cl [282] H ₂ O-H ₂ O [33] HCl-HCl [106]
<i>Total van der Waals</i>	2-415 10 ⁻⁷⁹ Jm ⁶	weak	0.2-10	H ₂ O-H ₂ O [139] (50) CH ₄ -CH ₄ [102] (10) CH ₄ -CH ₄ in H ₂ O (56)
Hydrophobic	0-20 kJ/mol	weak	10	CH ₄ -CH ₄ in H ₂ O (56)

¹ The contributing energies are scaled by the magnitude of the van der Waals energy coefficients in units of 10⁻⁷⁹ Jm⁶. For total van der Waals energies (nn) the units are kJ/mol. Converting between these units requires accurate knowledge of van der Waals radii as the interactions scale as r⁻⁶.

units. *Coulombic* forces are almost as strong as covalent forces, and have a long interaction range in water so that they have major effects on particle aggregation. At long distances (> nm) mixed charges on a surface average out, but for very near interactions the alternating charges of ionic solids become significant, and can lead to attractive interactions between similarly net charged surfaces. *Fixed dipole-charge* interactions can be about half as strong as covalent bonding, and are very important in ion solvation. The force varies as r⁻². At room temperature and typical ion-water molecule distances the dipole-charge interaction is much larger than kT and thus creates a solvation sphere about the ion that can behave practically like a molecular unit. This is especially true for small highly charged species such as Al³⁺. *Fixed dipole-dipole* interactions can be as large as

1/5 to 1/10 of covalent bonding forces, but are only significantly larger than kT for molecules with large dipole moments. This is a crucial consideration as water has a relatively large dipole moment and the small proton allows for short interaction distances with other dipoles and thus strong dipole-dipole attraction. This strongly directional type of bond is usually called a *hydrogen bond*, and is responsible for many unique properties of water.

Van der Waals forces are actually composed of three components: freely rotating dipole-dipole, freely rotating dipole-induced-dipole, and induced dipole-induced dipole (dispersion or London) interactions. Net van der Waal forces are almost always attractive, as opposed to Coulombic and dipolar forces which can be strongly repulsive. The fall off with distance is by r^{-6} , so the interaction distance is crucial. It might seem as though freely rotating dipole interactions ought to cancel out, but this does not happen due to Boltzmann weighting factors which favor the lowest energy orientations. The interaction energy of two permanent dipoles is inversely dependent upon the temperature, while the interaction energy of dipole-induced dipole is independent of temperature. The magnitude of induced dipole interactions depends on the polarizability of the molecule. The dispersion component is due to the finite instantaneous dipole moment of any atom's electron distribution. It is always attractive. The effect is called the dispersion effect since the electronic movement that gives rise to it also causes dispersion of light, i.e., the variation of refractive index of a substance with the frequency (color) of the light. Van der Waals forces are quite weak, but are usually equal to a few kT at room temperature. As might be expected, van der Waals forces are difficult to calculate in complex systems, as other nearby atoms affect the polarizability of the electron distribution. A detailed discussion of van der Waals contributions to molecular interactions is available in Israelachvili (1992), and dispersion forces are treated quantitatively in Mahanty and Ninham (1976). *Hydrophobic* forces are the net attraction observed for hydrophobic molecules and surfaces in water. This can be significantly larger than their attractive forces in vacuum, as shown for methane molecules in Table 1. The bases of this force is an entropic phenomenon due to rearrangement of water hydrogen bonding configurations about closely approaching solvated species. The force has much longer range than covalent bonding. Israelachvili and Pashley (1982) found that the force between two macroscopic curved hydrophobic surfaces in water decayed exponentially in the range of 0-10 nm with a decay exponent of 1 nm. The free energy of species dimerization was found to linearly relate to the species diameter. Hydrophobic interactions have important roles in biological surface phenomena, molecular self-assembly and protein folding, and hence are an important aspect of nanoparticulates with hydrophobic components.

Electrical double layer, Derjaguin approximation and DLVO theory

Particle-particle interactions involving the forces above are not simple sums over each type of interaction. Moreover the electrical structure that develops at a solution-solid interface has a large effect on the net attractive or repulsive forces between particulates. This electrical structure is called the electrical double layer in its simplest depiction. The double layer results from the interaction of a charged surface with charged solution species and dipoles. The surface charge occurs due to ion adsorption or ionization of a surface chemical group. Transition metal oxide and hydroxide surfaces equilibrate with aqueous solutions by trading protons and hydroxyls from metal surface sites. At low pH values the surfaces are more protonated and tend to be positively charged, with the polarity reversing as hydroxyls increase with increasing pH. Specific dissociation constants dictate at what pH a surface switches from net positive to net negative, a pH value sometimes referred to as the point of zero charge.

Much has been written in the geochemical literature about electrical double layer

theory (e.g., Sposito 1984; Stumm 1987; Davis and Kent 1990), so we show only the main models here. These are the capacitance, diffuse, Guoy-Chapman and Stern-Grahame models (Fig. 10). The capacitance model relates the electrochemical potential in the vicinity of an interface to a parallel plate capacitor. This has a linear dependence of potential with interface position, and is only a fair approximation of an actual interface situation. A more realistic model assumes only counterions in solution, and the application of the Poisson equation in electrostatics to solve for the variation of potential with distance. This is combined with the Boltzmann distribution to yield a Poisson-Boltzmann equation which will give the potential, electric field and counterion density at any point in the double layer (Israelachvili 1992). A linearized version of this equation, applicable to low potentials (using the Debye-Hückel approximation) yields a potential profile with distance that is non-linear, and is attributable to a “diffuse” swarm of counterions balancing the surface charge. A more general calculation is the Guoy-Chapman model derived for a planar double layer without assumptions of low potentials. Although Guoy-Chapman models are closer in form to observations, they still did not agree with experiment, particularly for mercury electrodes. This led to the Stern-Grahame model which uses a compact (Stern or Helmholtz layer) of counterion charges against the surface, and a diffuse layer derived from a Guoy-Chapman type treatment farther from the surface. The potential is assumed to be linear across the Stern layer.

One of the problems in calculating the forces acting on particles in solution is that we can calculate interaction energies for molecules (Table 1) but do not have a way to readily relate these to the forces between interacting real particles. This is especially important as particle-particle and surface-surface forces can now be measured by several methods. Use of a force law with the theoretically simple parallel planar surface model will always yield infinite forces as the planes are themselves infinite. A solution is obtained by use of the Derjaguin approximation (Derjaguin 1934) wherein the force between two interacting spherical particles can be given in terms of the energy per unit area of two flat surfaces of fixed separation. This strategy is applicable to any force law, whether attractive, repulsive or periodic.

Using this approximation Derjaguin and Landau (1941) and Verwey and Overbeek (1948) described a model (DLVO) which incorporated double layer electrostatic forces with van der Waals forces, and which explained much of colloid behavior. Figure 11 shows the basic nature of the DLVO model. As particles of the same type are considered to have the same surface charge, the net double layer forces are repulsive while the van der Waals forces are always attractive. For short distances the van der Waals forces dominate due to the r^{-6} power law, but at distances of a few nm the balance of forces can create local minima and thus stability at a well-defined separation. In this model the van der Waal forces are also assumed to be independent of electrolyte concentration and pH, which is not too bad a first approximation. The general form of the DLVO model is shown in the inset. There is a primary minimum, a secondary minimum, and an energy barrier. Curve a represents highly charged surfaces in a dilute electrolyte. Large planar surfaces will feel a long range repulsive force, and would become attractive if forced together with a great expense of work. Nanoparticles would be stable and resist aggregation. Curve b represents somewhat higher concentration electrolytes and shows the creation of the secondary minimum. Planar surfaces would be at equilibrium at this secondary minimum, and nanoparticles would either remain dispersed in solution or form an association at the same minimum. A colloid formed with such a energy minimum is called *kinetically stable* as opposed to *thermodynamically stable* as would occur if the particles were forced together and reached the primary minimum point. The energy barrier is lowered if the surface charges are lower, and this situation is represented by curve c. Large surfaces will equilibrate at the secondary minimum, but nanoparticles will

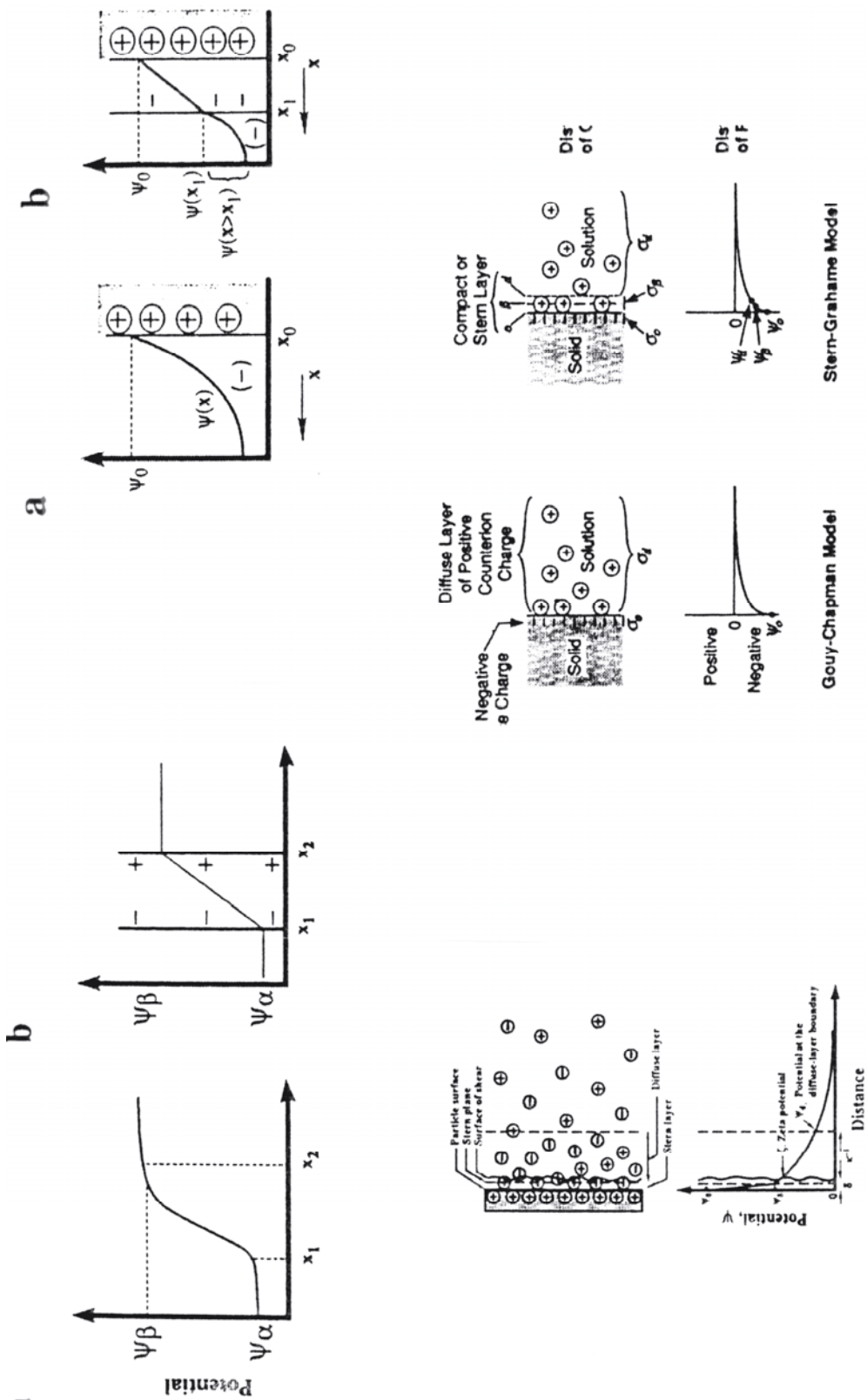


Figure 10. Electrical double layer models. Top right: (a) typical type of potential vs. composition plot for a charged surface compared to (b) constant capacitance model. Top left: Two double-layer models. (a) diffuse double layer. (b) part parallel plate capacitor and part diffuse layer. Bottom left: Stern layer model. Incorporation of adsorbed ions to surface. From Hiemenz and Rajagopalan (1997) Bottom right: Comparison of Gouy-Chapman and Stern-Grahame models of the electrical double layer. From Davis and Kent (1990).

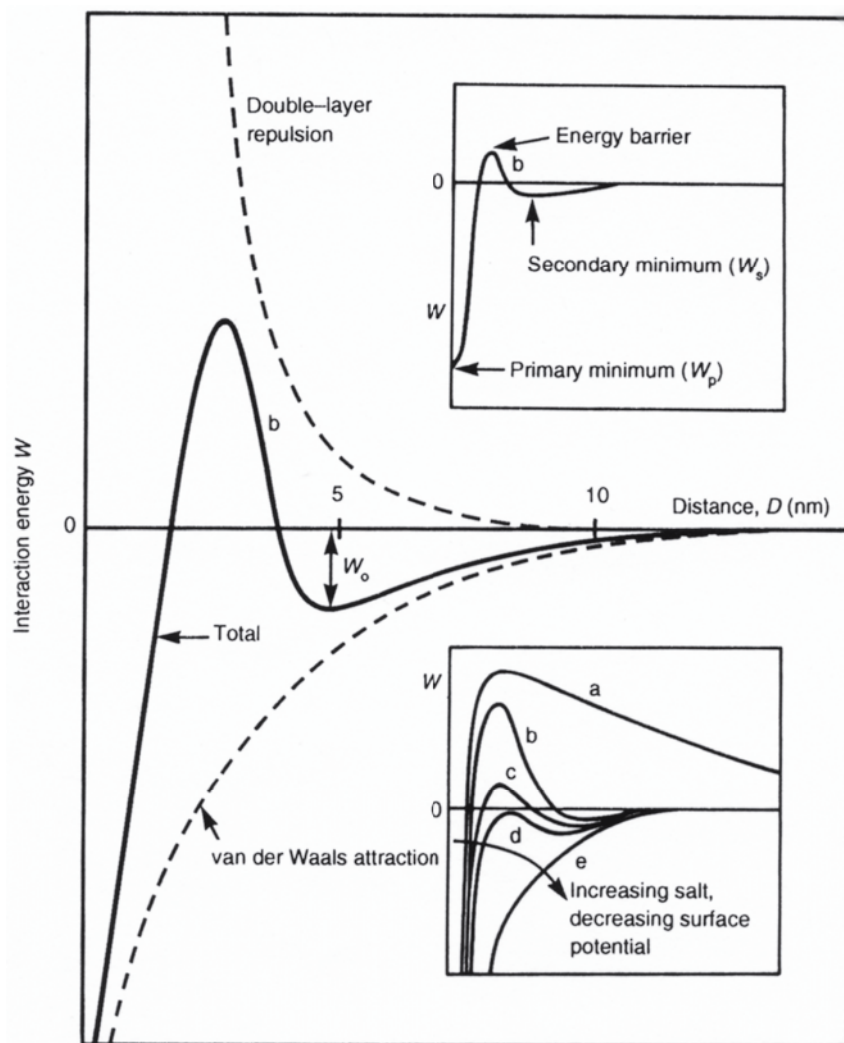


Figure 11. Interaction energy with separation distance for DLVO forces between interacting surfaces or particles. Top inset shows definitions for critical points on energy curve. Bottom inset shows the shape of the curve for different conditions. (a) Highly charged surfaces, dilute electrolyte. (b) Highly charged surfaces and more concentrated electrolyte. (c) Moderate surface charge and more concentrated electrolyte. (d) Moderate surface charge and highly concentrated electrolyte. (e) Weak or nil surface charge. After Israelachvili (1991).

slowly aggregate (called *coagulation* or *flocculation*) due to the lower energy barrier. Above some electrolyte concentration known as the *critical coagulation concentration*, the energy barrier will fall into the attractive(negative) range, and nanoparticles will rapidly aggregate (curve d). Such a situation is referred to as an *unstable colloid*. Finally with near zero surface charges the interaction is mainly just a van der Waals attraction and large planar surfaces or any size particles coalesce rapidly (curve e).

Aggregation kinetics and kernels in the Smoluchowski equation

In contrast to what is clear from the DLVO model, early classical models of aggregation are based on an assumption that interparticle interactions are negligible until the particles contact. This contact then is assumed to result in adhesion 100% of the time. However, as particles are attracted together the fluid in the intervening space must be ejected, creating a hydrodynamic response in the particles, such as rotation. Neglect of

this effect in aggregation is termed *rectilinear* modeling, whereas inclusion is termed *curvilinear* modeling. The fact that hydrodynamic effects can combine with Brownian motion to rotate particles as they approach one another, opens the possibility that specific orientations for attachment may be slightly favored due to local strong directional interaction forces. This gives added credence to the possibility of oriented aggregation which is considered in detail in the chapter by Banfield and Zhang in this volume.

The adjustments made to the kinetic aggregation theory of Smoluchowski due to curvilinear effects, as well as to problems caused by the original simplifying assumptions, have been reviewed in detail by Thomas et al. (1999). Due to the form of the Smoluchowski equation, it is possible to make such adjustments by improvements to the kernels. For example, the rotation of particles in the curvilinear model can be taken as a decrease in their probability for attachment. A larger adjustment is the addition of particle-particle interactions through the use of DLVO and related theories. The addition of the kinetic effects of these theories alters the rates of particle collision, probability of particle adhesion, action of particles of different sizes, and the probability of floc breakup. Another important assumption of the original Smoluchowski theory is that perfectly solid spherical particles were coalescing into perfectly solid spherical aggregates. This is true for types of vapor deposition processes by which the original theory was tested, but not in general. In environmental systems the situation is about as opposite as it can be, with aggregates more properly described as fractal objects (Li and Ganczarczyk 1989). Use of fractal geometry allows for quantification of the geometric scaling properties of rather diverse types of physical aggregates, and enables separation of aggregation models on the basis of kinetic factors and cluster form (Meakin 1992).

Fractal dimensions of an aggregate

If it is assumed that a solid particle aggregates to a solid mass with no interparticle space, the mass of the aggregate as a function of r is given by

$$m(r) = \rho(4/3)\pi r^3 \quad (12)$$

If there are actually empty spaces between the particles then the mass must be reduced and a relationship like

$$m(r) = \rho(4/3)\pi r^{d_f} \quad (13)$$

might be used, where $d_f < 3$, representing a reduced spatial dimension. Remarkably, this works for a large proportion of physical cases, and the quantity d_f is known as the fractal dimension. It is possible to measure the fractal dimension by a number of techniques (some of which are discussed below). Fractal analysis and scaling properties are broad subjects that cannot be treated here in detail, but the crucial idea is that aggregates can be characterized in terms of fractal properties, and that kinetic formation models can be similarly derived so that aggregate structure can be related to particular formation processes.

Aggregation topologies

If the probability of particle adhesion controls the rate of formation of an aggregate, the process is known as *reaction-limited aggregation* (RLA). If the rate of formation is controlled by the rate of diffusion of particles to the growing aggregate, then the process is called *diffusion-limited aggregation* (DLA). DLA is a very general phenomena for all kinds of pattern formation (Halsey 2000). In keeping with the original Smoluchowski assumption of primary particle aggregation only, the classical version of DLA was derived by Witten and Sander (1981) and is called a diffusion-limited monomer-cluster aggregation (DLMCA) process. There are many types of variations upon these basic





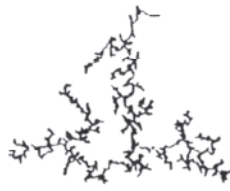
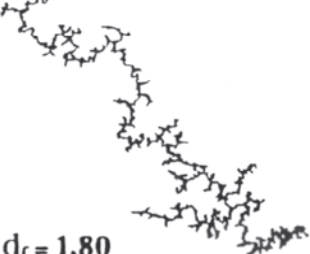
	Reaction-Limited	Ballistic	Diffusion-Limited
Monomer-Cluster	<p>Eden</p>  <p>$d_f = 3.00$</p>	<p>Vold</p>  <p>$d_f = 3.00$</p>	<p>Witten-Sander</p>  <p>$d_f = 2.50$</p>
Cluster-Cluster	<p>RLCCA</p>  <p>$d_f = 2.09$</p>	<p>Sutherland</p>  <p>$d_f = 1.95$</p>	<p>DLCCA</p>  <p>$d_f = 1.80$</p>

Figure 12. Different types of aggregation geometries. d_f refers to the fractal dimension of the aggregates. From Hiemenz and Rajagopalan (1997) with permission from Marcel-Dekker.

models, including permitting the adhesion of small aggregates to form larger ones, which leads to more expanded aggregates and lower fractal dimensions. This is an example of *diffusion-limited-cluster-cluster aggregation* or DLCCA. Other models, shown in Figure 12 include the reaction-limited cluster-cluster aggregation (RLCCA), rectilinear “ballistic” monomer-cluster (Vold and Vold 1983), rectilinear “ballistic” cluster-cluster (Sutherland 1970), and reaction-limited monomer-cluster (Eden 1961).

Another type of aggregation that differs markedly from these geometries is that imposed by so called “self-assembly” processes. For nanocrystals it has been possible recently to prepare particular habits and sizes, and stabilize these with organic or inorganic secondary coatings. The resulting entities are stable and can pack into superlattices in two or three dimensions. The nanocrystals are effectively the hard atomic-like cores that preserve lattice ordering, while the coatings perform as interparticle molecular bonds balancing the attractive forces against forcing the core nanocrystals into fractal aggregation (Yin and Wang 1997; Murray et al. 1995; Sun and Murray 1999; Caruso 2001). The strength and type of interparticle bond is mitigated by the type of organic molecules used, e.g., the length of the chains in these molecules or the types of functional groups (see Fig. 13). A somewhat different process is the reorganization of original aggregates into a different type of aggregate, rather than into a single crystal. This has been demonstrated in MnO_2 nanomaterials by Xiao et al. (1998) and Benaissa et al. (1997). In this case an initial low density random aggregate is slowly modified by the nucleation and growth of nanofibers which grow out of the aggregate surface by diffusional processes. The intersection of fibers from dispersed initial aggregates ultimately produces a mass of interlocking fibers (Fig. 14). This scenario suggests that hybrid aggregation/nucleation and growth processes may be important in both technological and environmental nanomaterial formation. Finally, rather different aggregation topologies can be produced by crystallographically oriented aggregation processes, such as the incorporation of particular defects, the introduction of polytypes,

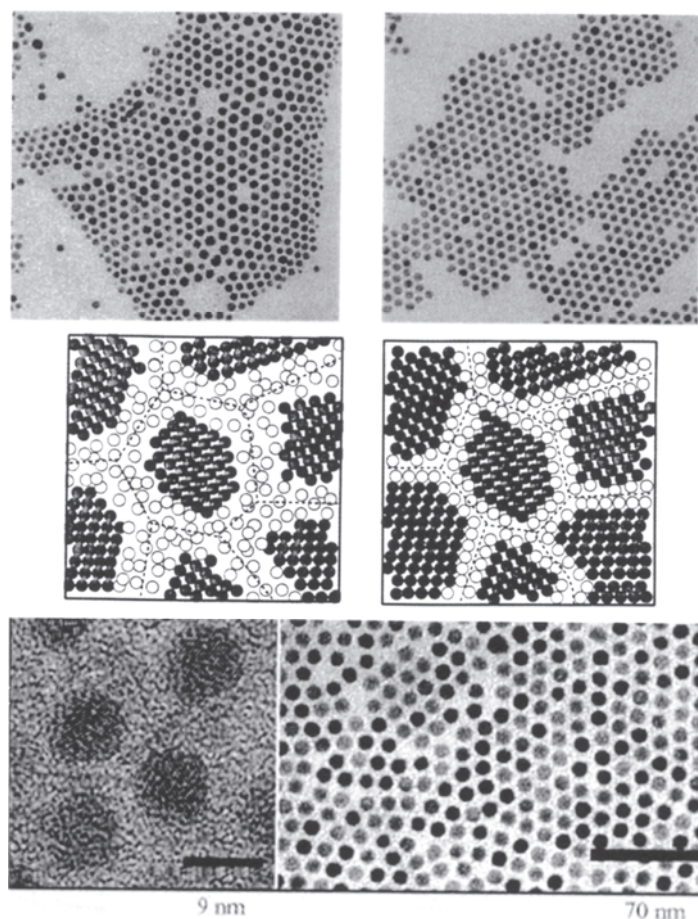


Figure 13. Aggregation/assembly of nanoparticles and nanocrystallites into superlattices and grain structures. Top right HRTEM image: assembly of capped Au nanocrystals into mosaic structures due to polydispersity. Note how sizes are sorted and produce new types of voids and curved registry. Top left HRTEM image: capped Au nanocrystals forming well-defined regular grain structures. Note incorporation of stacking faults and types of void spaces. From Martin et al. (2000), used with permission of the American Chemical Society, publishers of the *Journal of Physical Chemistry*. Middle left: Model for self-assembly of nanosemiconductor crystals having a large disordered region at the grain boundaries. Middle right: Analogous model with well-ordered grain boundary structure (from Weissmuller 1996). Bottom left: capped Pt nanocrystals. Bottom right: Self assembly of capped Pt nanocrystals.

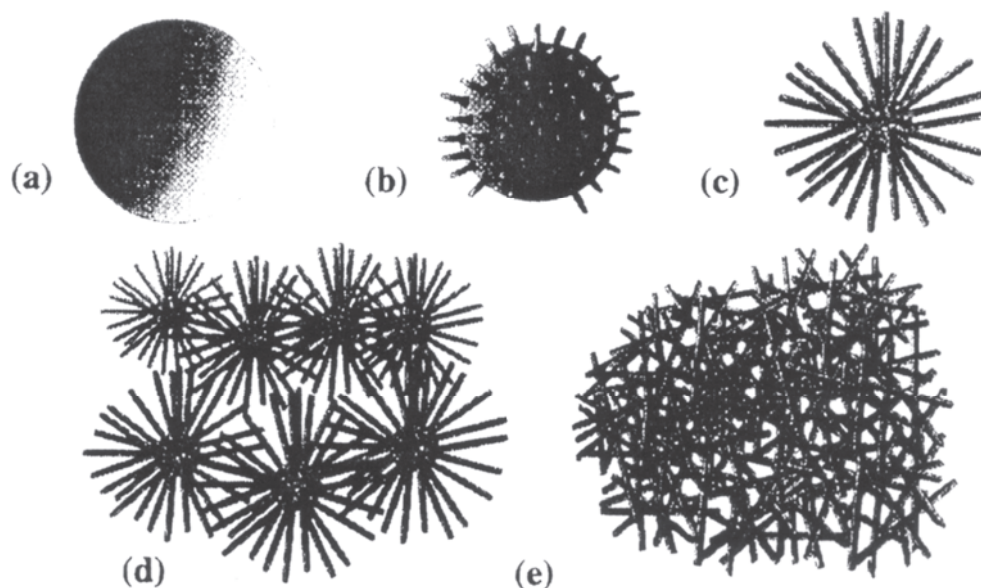


Figure 14. MnO_2 nanoparticle evolution during formation. (a) Initial aggregation produces densely packed clot of nanocrystals. (b) Nucleation of elongated nanocrystals and growth normal to surface of resorbing clot. (c) Nearly complete recrystallization of clot into spherulitic shapes. (d) Aggregation of spherulitic forms into loose clot. (e) Interweaving further growth of aggregate. After Benaissa et al. (1997).

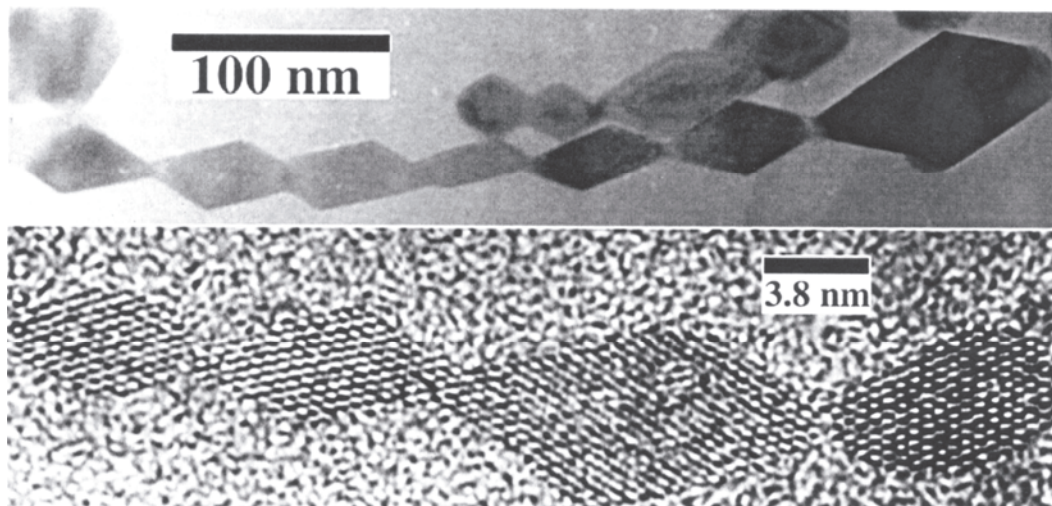


Figure 15. Aggregated nanoparticles of titania forming a single-crystal chain, an example of oriented aggregation. From Penn and Banfield (1999) with permission from Elsevier, publishers of *Geochemica et Cosmochimica Acta*.

and the nucleation of metastable phases (Penn and Banfield 1998a; 1998b). An example of a single crystal chain of nanoparticles formed by oriented aggregation is shown in Figure 15.

Simulations and state of knowledge

Simulations of growth by aggregation using various kinetic models consistent with DLVO theory have been done extensively over the past few decades, generally obtaining good agreement with observation for idealized cases. [For breaking news on many-body interactions that deviate from DLVO, see www.che.utexas.edu/~jeff/research/edl.html.] A thorough review of kinetic simulations is available (Meakin 1992), and numerous examples can be found in the NATO conference volume by Stanley and Ostrowsky (1986). From the point of view of physical theory, there remains much to be done in the area of fractal aggregation on surfaces, an area of obvious importance to geochemistry, and in the area of concentrated systems, such as in situations of low water saturation and increasing concentration. Thomas et al. (1999) make the point that many different aspects of porosity, nonsphericity, interaction forces, hydrodynamics and aggregation kinetics have been dealt with in the available literature, but generally in isolation from one another. Hence work needs to be done to integrate the available theory into a more realistic and applicable form, especially for geochemical systems. Another area which has not received much attention, is the coarsening (or *Ostwald ripening*) of aggregated nanoparticles into larger and more solid aggregates, or into single crystals. This is important for ceramic as well as geochemical processes such as diagenesis, solution encapsulation, impurity capture, and particulate transport. Krill et al. (1997) have reviewed the issues of stabilization of grain size and recrystallization in metallic nanocrystalline materials including the relevant factors of grain boundary motion and grain boundary energy.

STRUCTURE

Scales of structure

The discussions above concerning aggregation provide some background to the problems of characterizing the structure of nanoparticles and nanoparticulate aggregates.

First, there is the problem of *polydispersity* of particles and aggregates. It is one thing to attempt to deduce the structure of a set of objects that are all similar in density

and size, but quite another to sort out structure in ensembles where size, density, fractal dimension and other attributes are widely varying. Systems that are usually studied in nanotechnology, such as semiconductor and superconductor materials (see chapter by Jacobs and Alivisatos), and fine droplets or colloidal particles in solution, are much more amenable to structural analysis than environmental aggregates due to their more limited polydispersity. Second, there is the problem of intraparticulate diversity. One of the most important aspects of nanotechnology is the change in physical structure occasioned by reduced particle diameter (see discussion and examples of by Banfield and Zhang, this volume). This can take the form of unusual surface structure, or bulk structure. The degree of structural change may be dependent on particle shape and diameter, thus creating a distribution in structure variation and microstructures. Hence in the general case we need to consider the structure of particle surfaces, interiors, intergrain boundaries and aggregates, all with possible complex dependencies on size distributions. Attempts to sort all of this out, with even the complete arsenal of available structure probes, will require careful experimentation on selected and probably idealized environmental systems. On the other hand, the immense information carried in a complete description of the structural state of environmental nanoscale materials provides ample reason for pursuing this type of investigation.

Surface vs. bulk structure

Surfaces of any crystal have important differences from the interior of the crystal:

1. The long range periodic symmetry is broken, affecting bonding orbital systems, vibrational states, and thus many aspects of spectroscopic signature. Some of the coordination polyhedra of a structure must be different on a surface than in the bulk. Valence states on the surface may be altered by electron transfers associated with adjustments in bonding. This may be especially important in environmental Fe-Mn oxyhydroxides.
2. The chemistry of the surface may differ from the bulk. Except for materials prepared by high temperature anneal under high vacuum conditions, the surfaces of oxides are oxygen terminated. Hence the cations may have complete oxygen coordination, but none of the surface oxygens have complete metal coordination as in the bulk. In the rigorous sense, this means that a small oxide particle has an excess of oxygens and is thus nonstoichiometric. In other types of nanoparticles there may be a chemical gradient near the surface as one type of ion may tend to migrate to the surface. These considerations suggest types of investigations that can be used to specifically detect bulk vs. surface structural differences.
3. The differences in surface bonding can cause surface relaxation and/or rearrangement. Figure 16 shows surface models for $\alpha\text{-Al}_2\text{O}_3$ as obtained from crystal truncation rod (CTR) X-ray diffraction measurements. The differences among the vacuum-equilibrated, water-equilibrated and ideally bulk terminated structures are shown. Not only do the surface oxygens have reduced metal coordination, they and other atoms move (or "relax") from their bulk positions. This relaxation process at the surface can be understood using two different concepts for ion interactions: electrostatic and "bond valence".
4. A corollary to (2) is that environmental nanoparticles will be generally surrounded by water, either due to saturated conditions, or adsorbed water. Hence the surfaces of the particles must adjust to the bonding with water molecules, and possibly excess or surplus protons as dictated by the pH. This alone may cause a significant difference in the nature of the particle surface relative to a dry surface, e.g., a cleaved particle exposed to a dry atmosphere of pressure with sufficient oxygen partial pressure to maintain all metal valence states as in the bulk.

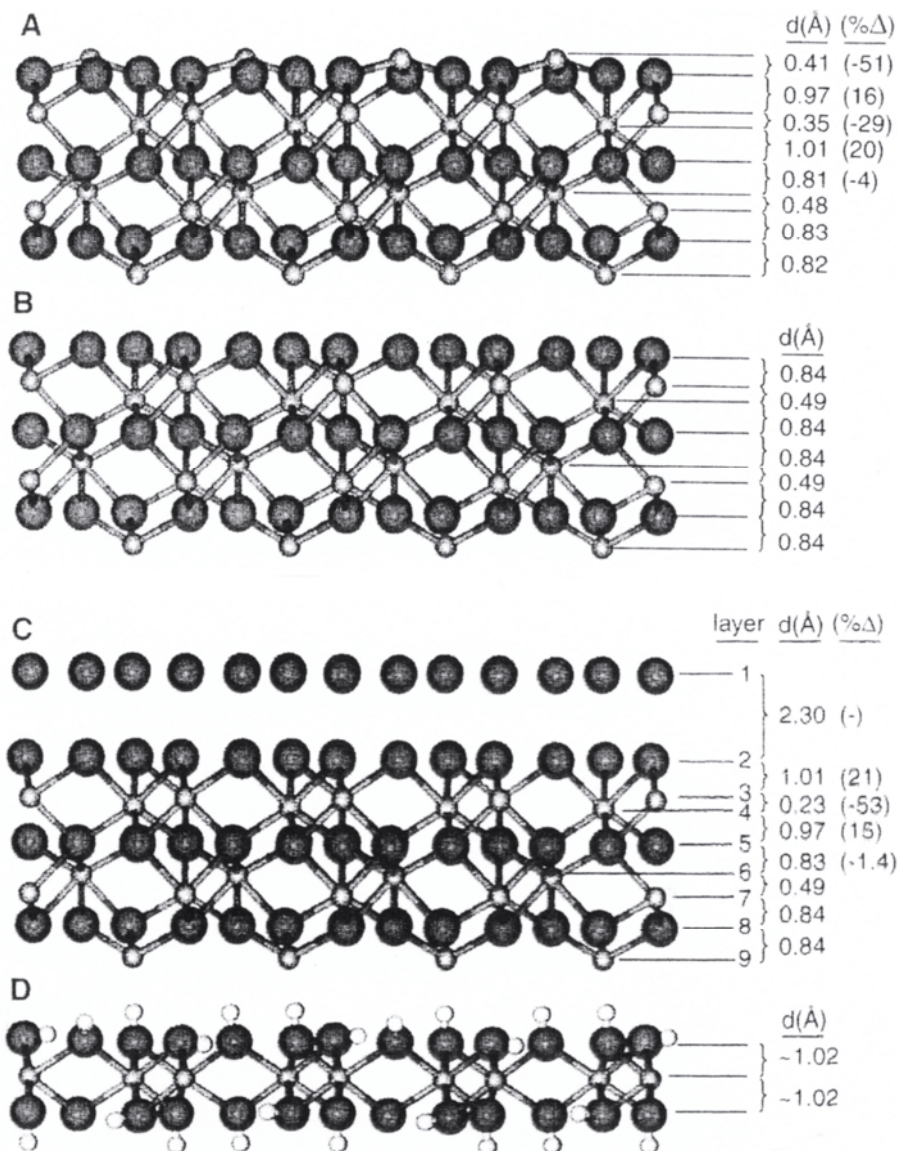


Figure 16. Surface structure the (0001) surface of sapphire (α - Al_2O_3) from Eng et al. (2000) with permission of the editor of Science. (a) Structure of vacuum-equilibrated dry surface. Al metal atoms sit on the surface. (b) Ideal bulk terminated surface with no relaxation or reconstruction. (c) Model for the wet-equilibrated surface at one atmosphere from surface scattering (crystal truncation rod) diffraction measurements. Al metal atoms have shifted, the surface is oxygen terminated, and an organized water monolayer is required to accurately describe the observations. (d) Structure of gibbsite or γ - $\text{Al}(\text{OH})_3$. The relaxed wet-equilibrated sapphire surface is intermediate between this structure and that of the bulk terminated structure (B).

Surface features

Symmetry considerations. Even in the case of perfect single crystals of large size that do not differ in atomic arrangement except for face terminations, the surface has a local symmetry that cannot include symmetry elements requiring operations in the z (surface normal) dimension. These operations include some types of glide planes, all screw axes, and center of symmetry, and the possible spatial symmetries are reduced from 230 space groups to 17 plane groups. This alone can have consequences for the type of bonding at surfaces. The symmetry is further broken by the presence of growth

features such as steps and terraces (see Figs. 10 and 11) which can be consequences of growth conditions as noted earlier. For the smallest nanocrystals, there are too few atoms to produce stable faces on the crystal, and in many materials the crystallite shape may be a consequence of electronic properties, i.e., covalency or electron delocalization effects involving the entire unit. On the other hand, if the crystallites are prepared near thermal equilibrium and are large enough (but not so large as to have habit altered by kinetic effects), it is expectable that the particle face and shapes will be predictable by the Wulff construction. This is testable provided that reliable calculations or measurements of the surface energies are obtainable.

Besides these basic aspects of surfaces, there are surface expressions of grain boundaries, and defects such as twinning planes and dislocations. Dislocations are expected to be unstable in nanocrystals (Gao and Gleiter 1987; Milligan et al. 1993; Thomas et al. 1990), though observations on this have been limited mainly to metallic and semiconductor nanomaterials. The absence of dislocations can have marked effects on mechanical properties of nanoparticulate phases. As certain types of planar “defects” are also consequences of non-stoichiometry, e.g., the so-called crystallographic shear structures called Wadsley and Magneli phases (Greenwood 1970; Wadsley 1964) common to TiO_x , MoO_x and WO_x systems, it is possible that types of nonstoichiometry could stabilize stacking faults in nanocrystals that would otherwise be energetically unfavorable.

Relaxation of surfaces. A common aspect of surfaces is a relaxation from the interatomic distances observed for the bulk material. The relaxation can be a net contraction or a net expansion depending on the type of material and surface chemistry. For oxide nanocrystals we can invoke the bond valence model to predict a surface contraction. Consider a simple NaCl-structure oxide like MgO. As we noted earlier the surface will be oxygen terminated, so that the surface oxygens do not have full coordination by Mg atoms. In the bond valence method, we sum the “valence” contributions about an anion to see if its valence needs are achieved. The valence sums are determined by the Mg formal charge and coordination, so that a six-coordinated Mg has a net valence contribution of $2/6 = 1/3$. The oxygen normally has six surrounding Mg atoms that contribute $6 \times 1/3$ valence contributions to add to 2. At the surface of MgO, the oxygen has coordination of 5 or less (depending on its exact position at the surface). Hence its valence is unsatisfied. It can make up this loss by decreasing its bond distance from one or more of the nearby Mg atoms, as it can also be shown that valence contribution is a function of bond length (Brown and Shannon 1973). Hence the overall effect of bond valence analysis suggests a surface contraction, at least in the top oxygen layer. But this situation may be altered by protonation of the surface oxygens. Single protonation may give the hypothetical oxygens too much bond valence (H contributes a full 1.00 valence contribution if not also hydrogen bonded to other atoms.) This bond valence sum would indicate an expansion of the top hydroxyl layer to lengthen the Mg-OH bonds. A mineralogically relevant example is the surface of $\alpha\text{-Al}_2\text{O}_3$ (sapphire or corundum). Eng et al. (2000) showed via surface X-ray diffraction that the (0001) surface equilibrated in air (i.e., with a few monolayers of surface water), has a structure that is intermediate between the oxygen terminated surface with no relaxation, and the gibbsite ($\gamma\text{-Al}(\text{OH})_3$) structure (Fig. 16). This means that the nearest surface Al atoms are displaced 0.14 Å down into the crystal, and the next lower Al atoms displaced 0.11 Å upwards towards the surface relative to the bulk structure. The oxygen layers above and below these Al atoms increase in separation by 0.04 Å, so that the Al-O distances increase relative to the bulk, i.e., a surface expansion.

For a different interpretation of surface relaxation, see Linford (1973) and Onodera

(1991), who consider the role of capillary forces in surface stress and relaxation. Still other mechanisms for surface relaxation involve the changes in vibrational amplitude of surface atoms, which surprisingly can be either larger or smaller than in the bulk phase depending on the vibrational modes active at the surface (Schreyer and Chatelain 1985). Anharmonic vibrations can result in net changes in mean atomic positions if vibrational amplitudes at surfaces are larger than in the bulk.

Reconstructions, distorted or altered coordination environments, incomplete coordination polyhedra and changes in surface bonding. Significant repositioning and ordering of atoms on a surface can lead to surface cells that are quite a bit larger than the projection of the unit cell onto the surface plane. Smaller analogs of the familiar 7×7 reconstruction of the silicon surface, and reconstructions seen in metal single crystals could also occur on mineralogical nanocrystal surfaces, but there has been little observational evidence to date. The small sizes of crystallite faces might disrupt equilibration of reconstructions, as these represent energy reductions that may be smaller than variations in interfacial energy for small particles. It has already been mentioned how oxygen termination of an oxide surface leads to lower coordination for the oxygens. However cation coordination can also be altered due to relaxation effects at a surface, or affected by the presence of surface defects and other features. For example, at the edges and corners of ledges or steps on an oxide surface a metal atom (say in MgO) could have two or three oxygens about it having reduced coordinations. As the symmetry constraints of the structure do not apply to such a site on the surface, the metal atom is free to reconfigure its coordination environment to lower the local energy. The coordination could distort or change in number. Changes such as this have been suggested for the ferrihydrite surface (Zhao et al. 1994), for TiO_2 surfaces, and are consistent with bond valence concepts. For the TiO_2 surfaces, Chen et al. (1999) suggested that the surfaces of 1.9 nm particles have a significant number of highly distorted and probably 5-coordinated Ti sites. XANES analysis indicated that the geometry of these sites was a square pyramid. Binding of other molecules on the surface of the particles restored the coordination geometry to 6-coordination. Current quantum mechanical calculations appear inadequate to predict whether such coordination changes would occur. Hence for both reconstructions and coordination changes we may be forced to rely on characterization of experimental materials for the present.

Bulk nanoparticle features

Lattice contraction/expansion. Just as the surface can experience a relaxation, the bulk of a nanocrystal may expand or contract in lattice dimensions. One of the first clear observations of this was in Cu metal by Montano et al. (1986), who showed that the Cu-Cu distance decreased as nanocrystallites were reduced in size. The Cu-Cu distance appeared to form a continuous trend toward that of Cu-Cu gaseous dimers. Lattice contraction is also seen in nanosized silicon particles having thin surface coverages of amorphous silicon dioxide (Hofmeister et al. 1999). Due to the oxide layer this effect may arise more from compressive stresses than a change in silicon bonding. Lattice contraction is observed in Sn and Bi particles (Nanda et al. 2001), and explained by treating the nanoparticles as if they are droplets with a high effective external pressure, i.e., strain induced by the large surface area. In nanosized Pt particles it has been suggested that the lattice contraction is due to an increase in cohesive energy for particular geometric shapes (Khanna et al. 1983). Aggregation, occupation of zeolite cages and surface stabilizing films all reduce the contraction effect in Pd, Pt and Au nanocrystals (Fritsche and Buttner 1999). In the case of oxide nanoparticle systems both expansions and contractions have been observed. Tsunekawa et al. (2000a) studied nanocrystalline BaTiO_3 particles in the size range from 250 to 15 nm. With size reduction

to the smallest sizes, a 2.5% expansion in the lattice parameter is observed. At 80 nm there is also a change in the overall space group symmetry, from tetragonal (ferroelectric) to cubic. Tsunekawa et al. (2000b) examined the lattice expansion in both BaTiO₃ and CeO₂ by photoelectron spectroscopy (XPS) and simulation methods. They found in the case of CeO₂ that the expansion of the lattice was caused by reduction of some of the Ce⁴⁺ ions to Ce³⁺, and in BaTiO₃ by the increase of ionicity of the Ti ions. In contrast, Cheng et al. (1993) found a net lattice contraction in nanoparticle TiO₂. These studies suggest a major difference between metal and oxide nanoparticles, which may be extremely important for catalysis processes.

Grain boundaries, stacking faults and grain boundary encapsulation. A large body of literature has dealt with the nature of grain boundaries in metals and other materials (see e.g., Bollman 1970). Stacking faults are similarly well understood crystallographically. The question here is whether these structural aspects will be different in nanoparticles, i.e., will they occur in different geometries or densities, and will they have a large effect on nanoparticle properties? As noted earlier, dislocations should be disfavored in small nanocrystallites. This is not only due to rapid diffusion rates, but also repulsive forces between dislocations that restrict their density (Alivisatos 1997). However, dislocations, stacking faults and grain boundary structures will be generated by particle aggregation. Penn and Banfield (1998) showed that dislocations could be created by small misorientations at the interface between assembled nanoparticles of TiO₂ (anatase). Crystallites of 5-6 nm in diameter were reacted under hydrothermal conditions to produce coarsening. HRTEM photos showed clear evidence for dislocation formation at primary particle attachment zones (Fig. 17). Particularly if surfaces of nanoparticles are chemically altered, e.g., passivated by a thin coating of water or surfactant (i.e., “capped”), or altered in composition or stoichiometry, a large density of defects can be preserved at grain boundaries during aggregation. These defects may dominate the physical properties of the aggregate, and kinetic factors will determine their stability. (See also chapter by Banfield and Zhang for more details of grain boundary and nanoparticle defects.) Grain boundary density and structure are also important factors in aggregate recrystallization. In this case the energy added by these kinds of defects can serve as a driving force for diffusion and recrystallization. On the other hand, particular types of grain boundaries may be stabilized with impurities, and act to frustrate recrystallization processes. An example of the simulation of grain boundaries is that of MgO nanocrystallite films (Sayle and Watson 2000). Although thin films can retain enormous strain energy making them in this sense poor analogs of monodispersed nanoparticles, they are technologically widespread and widely studied. Figure 18 shows the results of Sayle and Watson’s simulation of 2 to 3 layers of a nanocrystalline MgO film. Particularly notable are the fairly well-defined type of voids at the grain boundaries, many of which are the cores of dislocations (label A). Other features are the mixed screw-edge dislocations (label B), and regions of hexagonal MgO (label C). The calculated model shows how the dislocation cores could be stabilized by doping with impurities, and also how some of the lattice mismatch between grain boundaries can be made up with an expanded type of local lattice, in this case pseudo-hexagonal.

Impurities and point defects. Point defects are stable equilibrium species and both impurities and vacancies will be present in any nanoparticles. Due to the expansion/contraction effects we have discussed above, impurities or vacancies may migrate into the bulk or to the surface depending on size and relative charge. Grain boundary “decoration” by impurities are common in metallic alloys, but little studied in nanoparticulates. In mineral systems, aggregation of nanometer particles could provide grain boundary sites for species not readily sorbed onto typical grain surfaces. Hence aggregation of grains could provide a new mechanism for remediation of toxic agents,

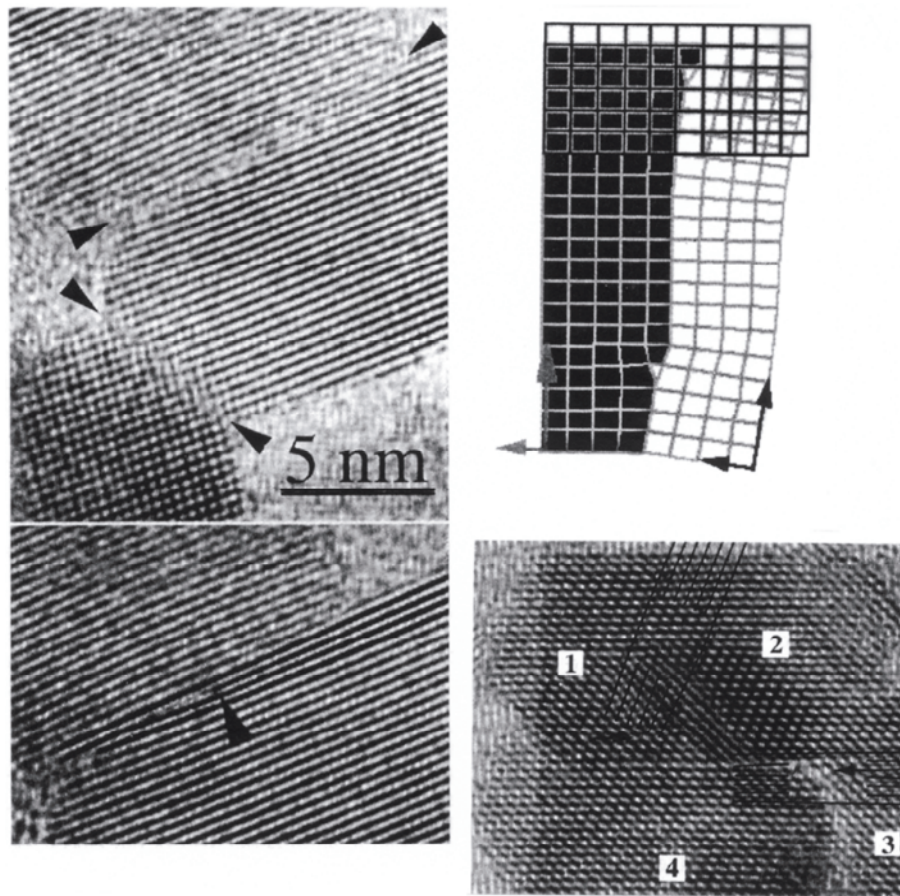
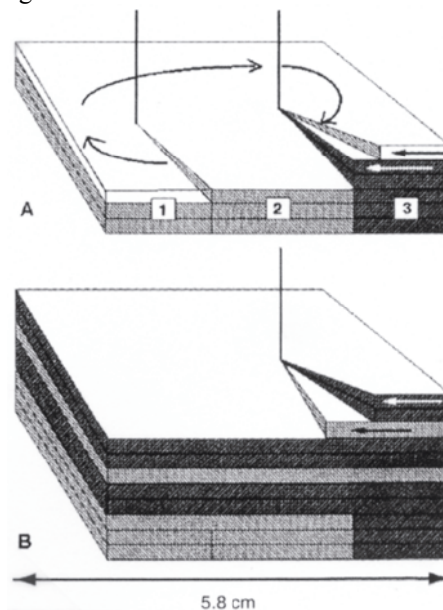


Figure 17. Origin mechanism for dislocations in TiO_2 . Left: Three attached nanoparticles (top) showing interface regions. Upper interface is reproduced (bottom) to clarify edge dislocation. Center, top: Diagram illustrating misorientation of idealized grains and the formation of dislocations. Lower grains join initially with surface steps causing a rotation. Third crystal is attached atop the other two oriented with the left crystallite, but rotated with respect to the right crystallite. Both edge and screw dislocations are thus formed. Center, bottom: HRTEM image of a crystal formed by attachment of four primary particles. Arrowheads and lines indicate edge dislocations.

Right (A): Block diagrams showing how growth at two adjacent screw dislocations can occur and give rise to polytypism. Three separate crystals have joined with slight orientational mismatch to create the dislocations. (B) The growth occurs at each leading step and allows intimate stratification of the crystals. From Penn and Banfield (1998a).



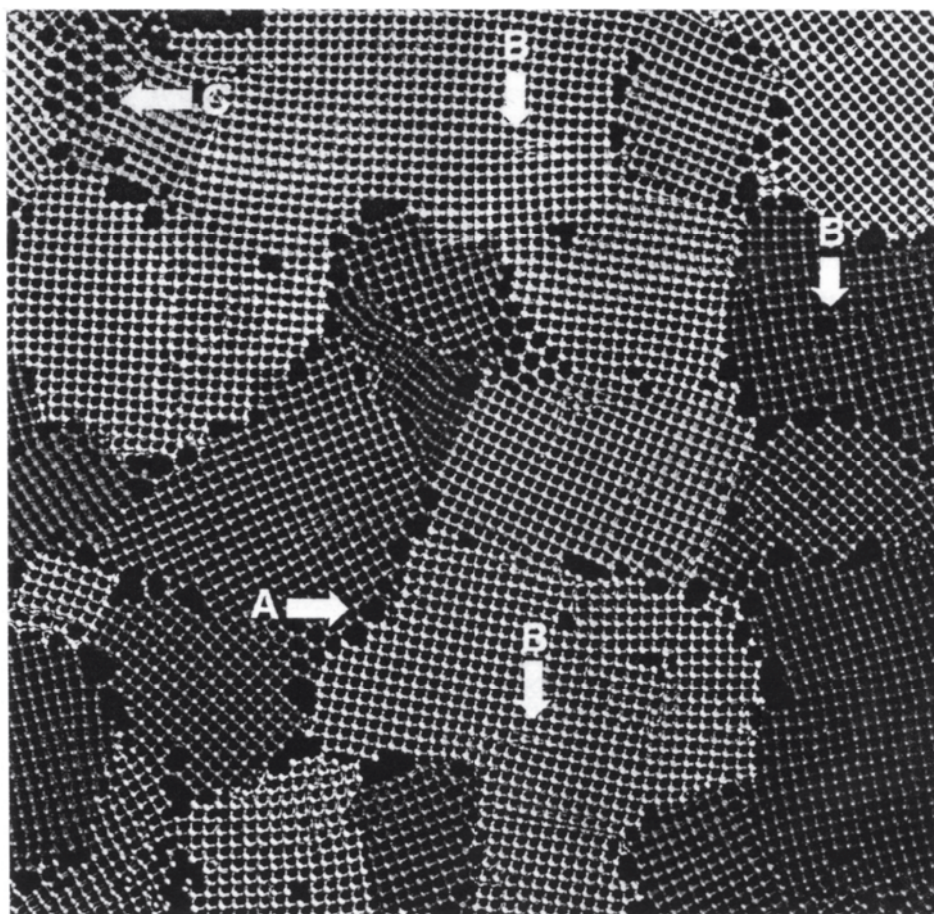


Figure 18. Simulated MgO grain and grain-boundary structure. Note the regular voids at A, defects at B and hexagonal structure at C. From Sayle and Watson (2000), used with permission of the Royal Society of Chemistry, publishers of the *Journal of Materials Chemistry*.

and also explain how seemingly incompatible impurities are incorporated during growth (Banfield et al. 2000).

STRUCTURE AND SHAPE/SIZE DETERMINATION

Atomic structure—TEM, X-ray scattering and diffraction

The details of nanoparticle crystal structure are mainly determined by scattering and imaging techniques, sometimes assisted by spectroscopy that can decisively assign some aspect of the structure. The chapter by Banfield and Zhang gives examples of TEM imaging and image interpretation, hence we will focus here on the scattering techniques.

The most widely used and versatile technique remains X-ray diffraction and scattering. Traditional diffraction involves measurement of the Bragg peaks in either powder or single crystal patterns, usually by comparison with kinematical simulations of the same patterns. This is a mature field and structural analysis is straightforward if a good diffraction pattern can be obtained. General reviews of powder diffraction theory and application can be found in Klug and Alexander (1974) and Azaroff (1968), as well as the RIM volume on powder diffraction (Bish and Post 1989), while single crystal diffraction is treated well by Warren (1969) and Schwartz and Cohen (1987). A good

general discussion of nanoparticle X-ray characterization is given by Zanchet et al. (2000).

Bragg peak broadening

The Bragg equation for the scattering from a series of parallel planes of spacing d , is given by

$$n\lambda = 2d \sin \theta \quad (14)$$

where λ is the scattered radiation wavelength, and θ is the scattering angle, equivalent to half of the angular change in direction of the incident and scattered beams, 2θ . This relation simply indicates that the scattered beam has to match in phase the beams scattered from each plane of atoms. Hence the path difference from plane to plane must be a multiple of wavelengths. The integer n indicates the number of wavelengths that add to one path difference.

Small particles present difficulties for Bragg analysis. Particles in the sub-micron range will cause Bragg peaks to be broadened, with the peak widths increasing with decreasing particle size until the Bragg pattern grades into a diffuse non-Bragg or Debye scattering profile (see below). This broadening can be used to determine particle size, provided that the effects of strain on peak broadening can be taken into account. Particle shape also affects the degree of broadening of specific hkl reflections, and results in size uncertainties of 20% or more unless the crystallite shape is independently known. The broadening of Bragg peaks is created by decreasing coherence of scattering as the crystallite size decreases. Because X-rays can penetrate a fraction of a micron even into dense materials, scattering can readily occur from atomic planes from depths such as this within a crystal. For very intense scattering some of the scattered X-rays will be reflected backward toward the depths of the crystal and cancel some of the forward scattering. This is the phenomenon of dynamical diffraction, which is not needed for the evaluation of small particle diffraction as such cancellation effects are small for small crystals. The usual treatment is with the kinematical (or two-beam) theory where only incident and forward scattered X-ray beams are considered. From Figure 19 we can see that a large crystal with many atomic planes contributing to a Bragg reflection can only have finite Bragg intensity over a small angular range. All other directions of scattering are out of phase with one another and completely cancel. As the crystal gets smaller there are fewer and fewer contributing planes, and hence the phase cancellation is progressively relaxed. In the limit of a single scattering pair of atoms the scattering is not cancelled in any direction, but is only modified into a diffuse scattering pattern. Note that this model only applies within individual crystallites. The scattering from separate crystallites is effectively completely independent. A micron-sized particle composed of aggregated nanometer sized crystallites will have broadening associated with the latter size. The basic concept of broadening of X-ray reflections due to particle size was indicated by Scherrer (1918), who derived a semi-empirical formula to determine particle size. Later work gave more quantitative analysis of peak broadening and shape (Wilson 1963; Warren and Averbach 1950).

Bragg analysis and Rietveld method

Crystallites above about 50 nm (and smaller for electron diffraction) are large enough to yield broadened but characteristic diffraction patterns. By characteristic it is meant that the symmetry and geometric arrangement of the structure will be clearly reflected in the diffraction pattern. The normal way in which this is represented is via the crystallographic structure factor:

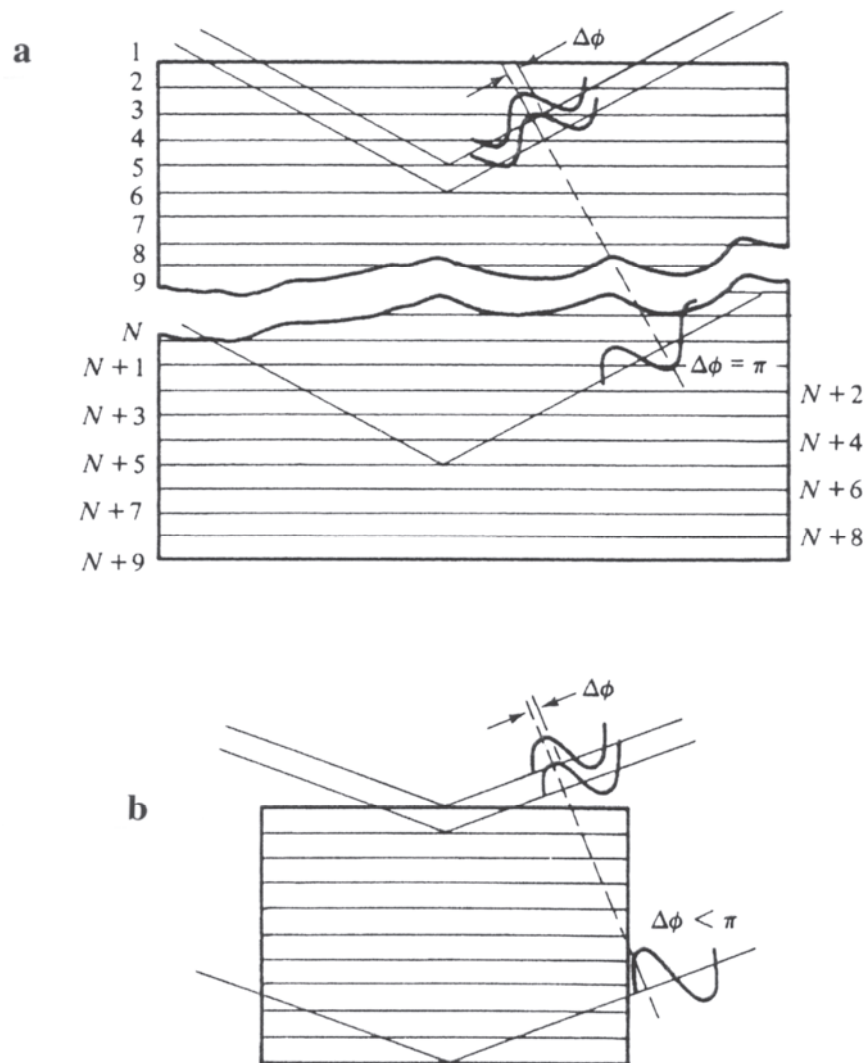


Figure 19. Origin of diffraction peak broadening in the kinematical approximation. (a) Large crystal with orientation just off the Bragg angle. For each different plane there is a slight phase shift in the scattered radiation. For some plane well below the top of the crystal surface there is a plane scattering out of phase with it. Hence for large crystals the reflection peak is quite sharp. (b) For small crystals scattering from the top and bottom-most planes do not create such a large phase shift when the crystal is set off the Bragg angle. Hence the range of angles where the scattered radiation is cancelled is reduced and the reflection broadens. From Schultz (1982) with permission of Prentice-Hall.

$$F_{hkl} = \sum f_n e^{2\pi i (hx_n + ky_n + lz_n)} \quad (15)$$

In this equation f_n is the *atomic scattering factor* or *atomic form factor*, h, k, l are the Miller indices of the reflecting plane, and x_n, y_n, z_n are the coordinates of the scattering atom in decimal fractions of unit cell parameters, a, b, c , respectively. For simple structures the structure factor indicates what types of Bragg planes in a given kind of structure can produce a diffraction peak, i.e., have non-cancelled, coherent scattering, and also indicates the relative intensity of the ‘allowed’ peaks (Warren 1969). A few structure factors for simple crystal structures are shown below.

Face-centered cubic (<i>F</i>)lattice	hkl mixed:	$F_{hkl} = 0$
	hkl unmixed:	$F_{hkl} = 4 \sum f_n e^{2\pi i (hx_n + ky_n + lz_n)}$
	MgO hkl all even:	$F_{hkl} = 4 (f_{Mg} + f_O)$
	MgO hkl all odd:	$F_{hkl} = 4 (f_{Mg} - f_O)$
	MgO hkl mixed:	$F_{hkl} = 0$
Body-centered cubic (<i>I</i>)lattice	$h+k+l = \text{even}$:	$F_{hkl} = 2 \sum f_n e^{2\pi i (hx_n + ky_n + lz_n)}$
	$h+k+l = \text{odd}$:	$F_{hkl} = 0$
Hexagonal lattice:	$h+2k = 3n, l \text{ even}$:	$F_{hkl}^2 = 4 f^2$
	$h+2k = 3n+1, l \text{ odd}$:	$F_{hkl}^2 = 3 f^2$
	$h+2k = 3n+1, l \text{ even}$:	$F_{hkl}^2 = f^2$
	$h+2k = 3n, l \text{ odd}$:	$F_{hkl}^2 = 0$

For structures with complicated unit cells and many symmetry elements the structure factor can be quite complex. However from these relationships it can be seen that there will be characteristic diffraction patterns for FCC, BCC or other atomic packings, and the intensities will have certain relative values (scaled by the scattering power of the individual atoms). With this information, the identity of simple structures can be deduced from the diffraction patterns, usually by comparison with many model calculated patterns. If the patterns are good enough, the presence of more complex structural aspects can be identified, e.g., the space group of the structure which defines the three dimensional set of symmetry elements of the structure can be determined subject to certain limitations, the presence of stacking faults which produce non-Bragg scattered intensity can be detected, and the effects of twinning characterized. In such case the structure can be refined via a variety of techniques to yield cell dimensions and cell angles. Full single crystal analysis of a nanoparticle has not been done, with the current minimum size limit using a synchrotron X-ray source being about 0.5 μm . This type of analysis requires one to be able to mount the single nanocrystal, orient it along known crystallographic directions, and collect diffraction data from a large set of unique diffraction planes. This body of information contains three dimensional structure information, and is needed to refine the positions and thermal vibrations of each atom in a unit cell of the structure. In the future this type of analysis may be possible for 100-nm crystallites extracted from materials, and possibly to similarly sized crystallites at the surface of aggregates. Present focussed X-ray beams at synchrotron sources are as small as a micron in diameter, and sizes to about 100 nm are possible. Single crystal structure analysis is described in detail by Azaroff (1968) and Glusker and Trueblood (1985).

An alternative to traditional single crystal diffraction analysis is the method described by Rietveld (1969), which has been widely developed for use on polycrystalline samples. This is an extremely important structural technique for poorly crystallized minerals (Post and Bish 1989). Rietveld analysis consists essentially in the calculation and least squares fitting of a complete powder diffraction pattern. This includes not only the structure factors which are proportional to the peak areas, but disorder, site occupation, strain, texturing and background intensity. Overlapping peaks due to various similarly spaced atomic planes are easily handled, as no extraction of areas or structure factors is done. Because of its full use of a powder pattern the Rietveld technique can be used to refine atomic positions in relatively complex structures, where use of structure factors alone would not be sufficient. Because the powder data input is essentially from a (ideally) random material and is thus averaged over all directions, the scattering data is one dimensional. Rietveld analysis has the advantage of being applicable to aggregates of nanoparticles as well as powders, but has not yet been applied

widely due to the general poor quality of diffraction data from small quantities of aggregates with crystallites below 50-100 nm. Rietveld analysis is regularly used with neutron diffraction as large samples are necessary and generally these must be powders or aggregates of single crystals.

Debye equation and scattering from small crystallites

For small crystallites (less than a few hundred atoms or so) we can calculate the diffraction as the sum over the scattering contributions (and interferences) of each atom-pair, i.e., we can neglect the scattering plane treatment as with Bragg diffraction. This is done with the Debye equation:

$$I(S) = D \sum_m \sum_n f_m f_n \frac{\sin Sr_{mn}}{Sr_{mn}} \quad (16)$$

This is a kinematical relation which is summed over each pair, mn , of atoms. Note that the sums would get enormous with any sort of macrosized crystal, so the calculation is impractical except for small clusters and molecules. The main feature is that the scattering for any one atom pair is a Fourier series of the form $(\sin Sr)/Sr$, a dependence which is common to all types of scattering where there is interference between the scattering from a given pair of elements. Other parameters are S , the scattering wavevector, f , the atomic scattering factor, D , the Debye-Waller factor which allows for damping of the Fourier oscillations as scattering angle increases, and N is the number of atoms in the cluster. D has a form like

$$D = e^{-\frac{(\Delta x)^2 \sin^2 \theta}{\lambda^2}} \quad (17)$$

where Δx is the rms atomic displacement from the equilibrium position. This ‘blurring’ of the atomic position reduces the intensity of scattering in a given direction, and preferentially at higher scattering angles. The Debye-Waller term is a way of introducing random structural or thermal disorder effects into the calculation. Because it is completely general, the Debye scattering equation is an excellent way to incorporate stacking faults, twinning, and other types of structural defects into a nanocrystal scattering pattern. For small metal nanocrystals having particular types of atomic packing and habits the results of the Debye equation calculation are shown in Figure 20. The effects of crystallite size also show in these calculated patterns.

The Fourier nature of the sums in the Debye expression allow the scattering function to be recast via a one-dimensional Fourier transform into a spherically symmetric picture of the interatomic distances r_{mn} . The resulting function is called a radial distribution function (RDF) and in the usual form is a series of peaks on a parabolic background which itself represents the mean atomic density of the sample. Other forms of the RDF subtract this average background to produce oscillations about zero. Different interatomic distances produce different sinusoidal frequencies in the Debye relation, and thus give rise to the discrete peaks (Fig. 21) in the RDF. The size of the region measured in scattering space (also called reciprocal or momentum space) dictates the amount of information in the scattering pattern. Smaller regions will show less of the sinusoidal variations in scattering, and hence will yield poorer estimates of the sinusoidal frequency and interatomic distances. In other words, smaller regions of scattering space will result in broader peaks in the Fourier Transform of the scattering pattern.

The size of scattering space is defined with a quantity like S :

$$S = 4\pi (\sin\theta)/\lambda \quad (18)$$

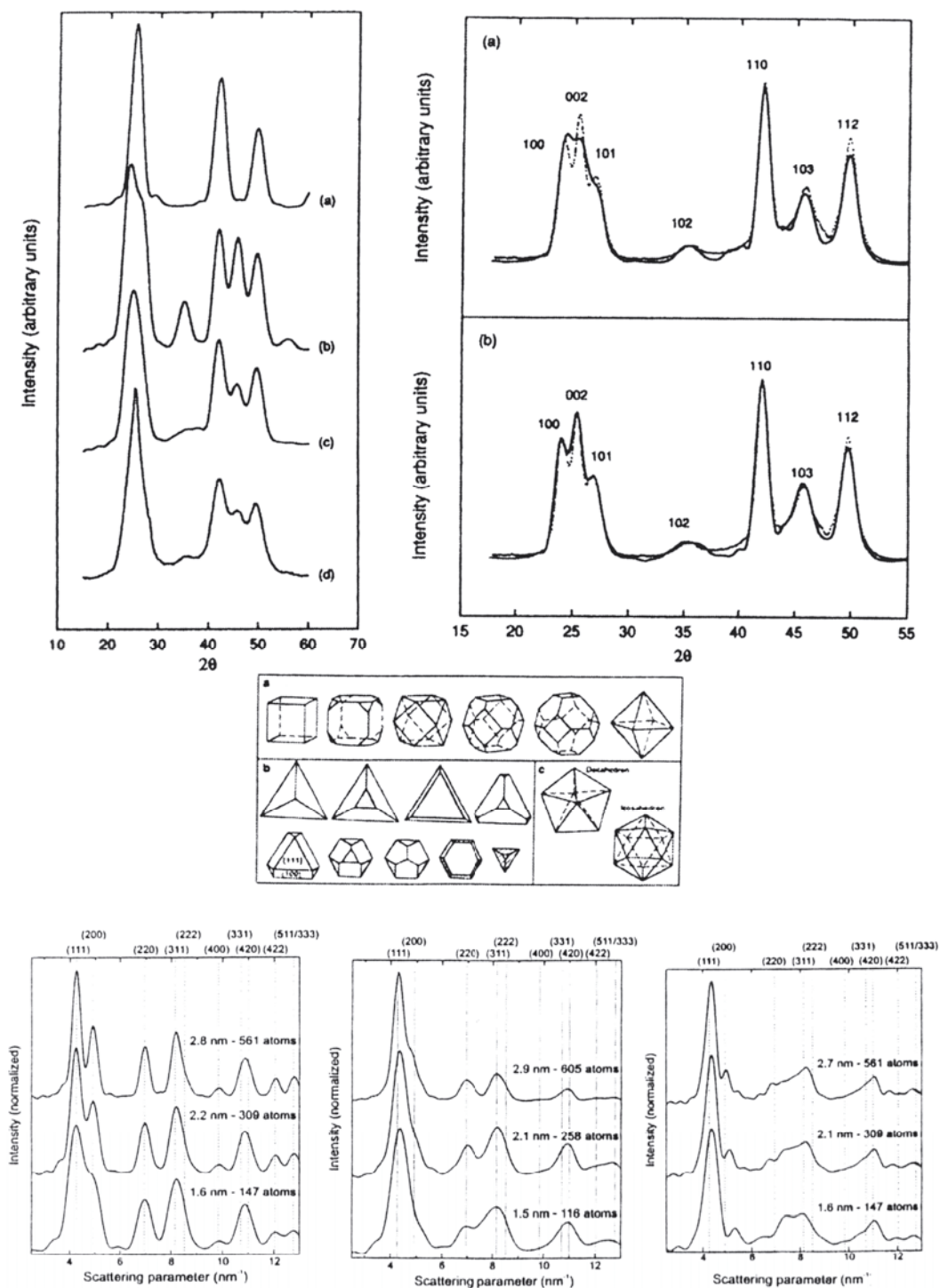


Figure 20. Calculated X-ray scattering patterns for various types and sizes of Pt nanocrystallites. Top left: 3.5 nm (a) sphalerite (b) wurtzite (c) wurtzite with one stacking fault (d) experimental powder spectrum with ca. 3.5 nm avg. crystallites. Top right: Experimental powder diffraction pattern of ca. 8.0 nm crystallites (dotted line) compared to: (a) spherical and (b) prolate particles (solid line) Center: (a) progression of habits of cuboctahedral shapes of nanocrystals. (b) change in shape as $\{111\}$ faces increase and $\{100\}$ decrease. (c) decahedron and icosahedron multiply twinned forms. Bottom left to right: three successive sizes of cuboctahedral nanocrystallites; three successive sizes of decahedral nanocrystallites; three successive sizes of icosahedral nanocrystallites. From Zanchet et al. (2000), used with permission of Wiley-VCH.

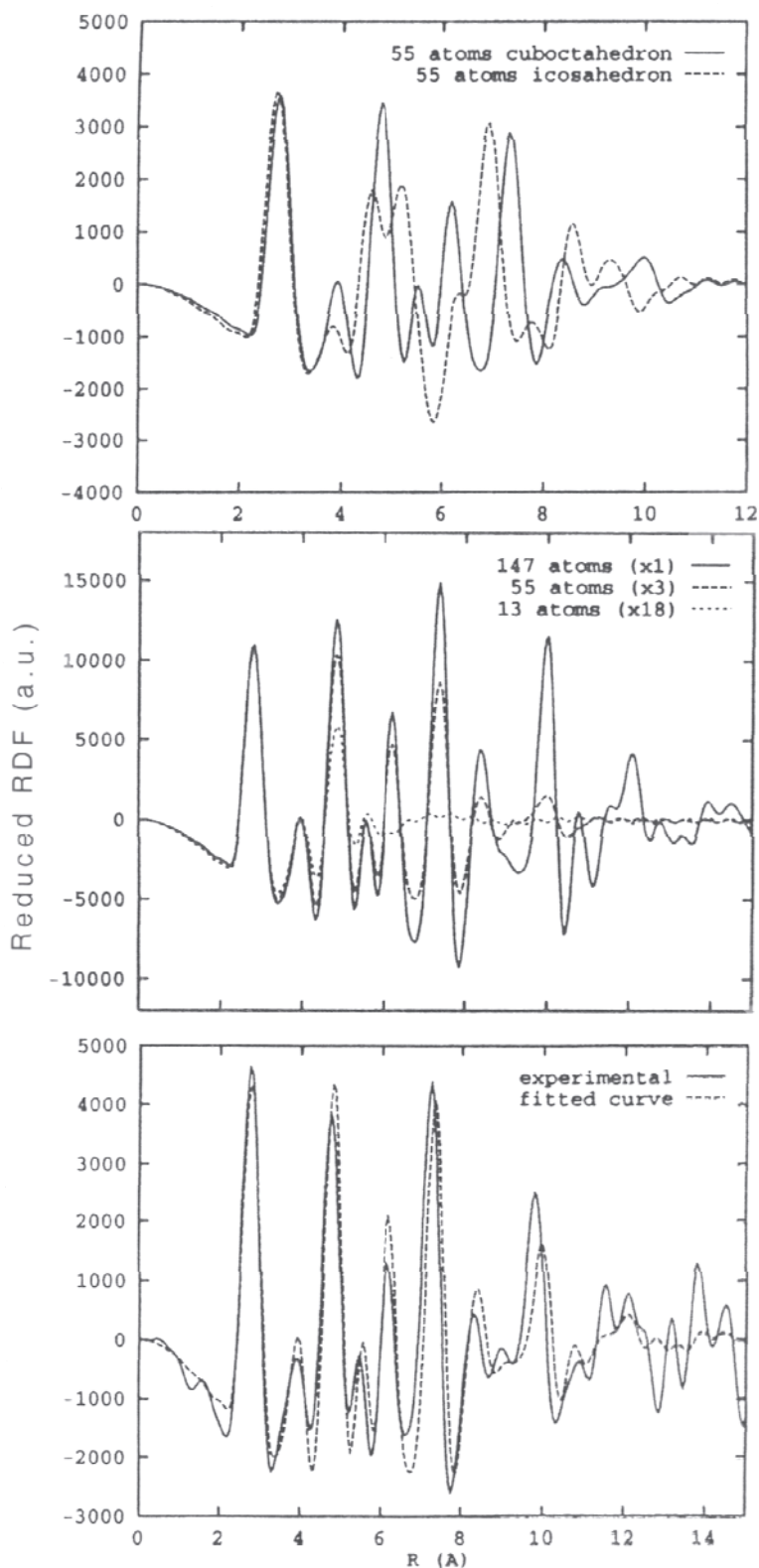


Figure 21. Radial distribution functions calculated using a Fourier transform of scattering patterns produced with a Debye equation. Top: Cuboctahedron (cluster with both octahedral $\{111\}$ and cube $\{100\}$ faces) and icosahedron (multiply twinned hcp structure) clusters of the same size. Center: Cuboctahedra of different sizes. Bottom: Experimental and simulated cluster RDF of a Pt colloid. The fit is a 90:10 mixture of 55 and 147 cuboctahedral clusters, respectively. After Casanove et al. (1997).

where θ is the scattering angle and λ is the X-ray wavelength. S has units of reciprocal length, usually \AA^{-1} . From Equation (18) the largest amount of scattering space is explored with the largest scattering angles and smallest wavelengths. A powder diffractometer usually uses $\text{CuK}\alpha$ X-radiation ($\lambda = 1.54 \text{\AA}$) and may have a scanning angle (2θ) of 120° . This yields a maximum S value of about 7\AA^{-1} . Using the full 0-7 range of S would yield peaks in the Fourier transform of about 0.45\AA in width, so that it would be difficult to sort out different atom-atom pairwise distances. For standard wide-angle X-ray scattering (WAXS) analysis, $\text{MoK}\alpha$ or $\text{AgK}\alpha$ radiation is used, with scattering angles up to 170° . This yields S values up to about 20\AA^{-1} and resolution in interatomic distances of about 0.16\AA .

In performing the Fourier transform the scattering data must first be corrected for absorption effects, air scattering components, the presence of inelastic scattering components, and effects due to the polarization of the incident X-ray source and any additional diffractive optics in the scattering apparatus (Klug and Alexander 1974). The data are then converted into S -space via Equation (18) and fit with a scattering profile indicative of the average scattering atom in the sample. This function is just the weighted atomic scattering for the sample composition, which is assumed to have the same profile for any type of atom in S space. The fitting is done only by setting a scaling factor for the atomic scattering curve. Once fit, the data will be seen to oscillate about the atomic scattering curve, i.e., the atomic scattering curve represents the total scattering without any interference effects as would be caused by some ordering of the atoms in the sample. The fitted atomic scattering is then subtracted and multiplied by S to give the function $S I(S)$, which is analogous to the output of (16). The Fourier transform is usually done with the expressions:

$$D(r) = 4\pi r^2 \rho_0 + \frac{2r}{\pi} \int_0^\infty S I(S) \sin Sr \, dr \quad (20)$$

$$G(r) = D(r) - 4\pi r^2 \rho_0$$

Here the first term in the $D(r)$ function is the average radial density function of the material which has the form of a parabola with ρ_0 equal to the average density in electron^2 units, and the second term oscillates about the parabola indicating distances of high and low atomic (electronic) density. The $G(r)$ function subtracts off the parabola so that the oscillation is about zero. Several representative RDFs of minerals are shown in Figure 22. There are several other types of radial distribution functions used in the literature, as well as the analog in EXAFS analysis below. For a complete review of the various types of analysis see Klug and Alexander (1974) and Warren (1969).

Examples. Nanoparticulates consisting of arsenate sorbed onto ferrihydrite were examined by Waychunas et al. (1996) using WAXS and EXAFS measurements. The crystallite size in the particles was reduced due to coprecipitation with high concentrations of arsenate, which sorbed on particle surfaces and effectively poisoned crystal growth. The $S I(S)$ functions and RDF's are shown in Figure 23, for particles of different mean size and arsenate concentration. It is very clear from the $S I(S)$ functions that as the crystallite size decreases so do the higher frequencies and thus the larger distance peaks in the RDFs. The smallest crystallites ($\text{As/Fe} = 0.7$) averaged about 0.8 nm in diameter.

Another approach to the analysis of a WAXS pattern is called Debye function analysis (DFA) and has been applied by several groups (Reinhard et al. 1997, 1998; Gnutzmann and Vogel 1990). The main difficulty in any diffraction experiment is that a unique structural model cannot usually be extracted from the data. This is obvious with powder diffraction data where for a complex structure there are far more structural

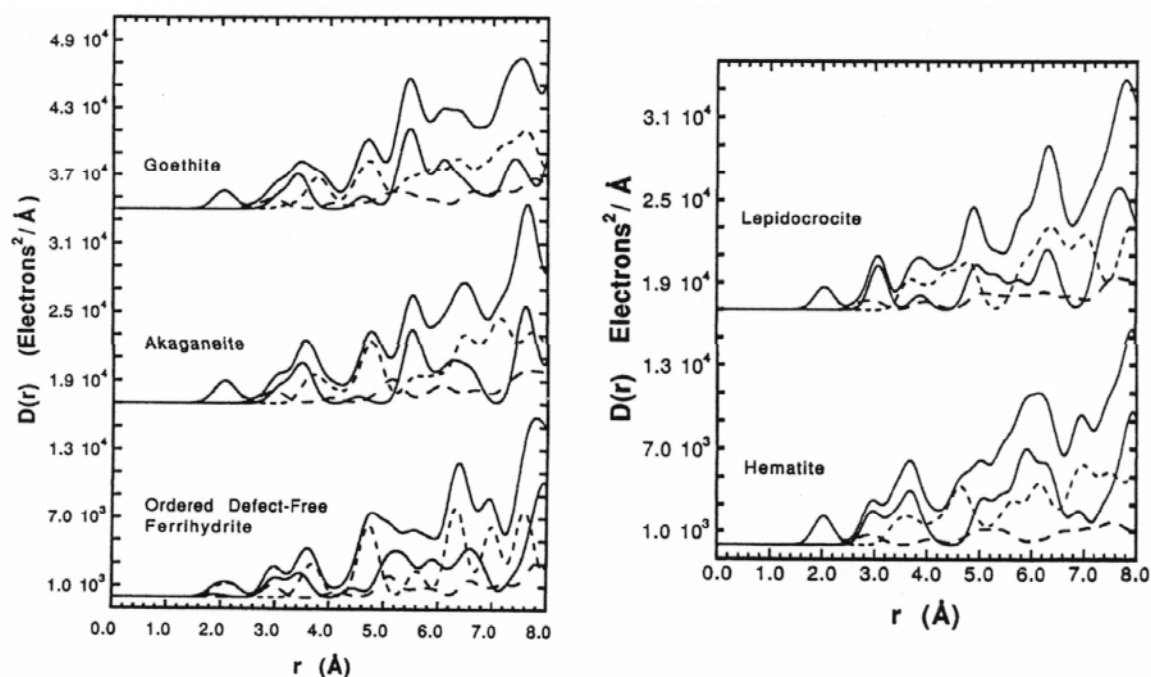


Figure 22. Calculated RDF functions for 2.0-nm diameter nanocrystallites of iron minerals. The overall RDF is a sum over all pair correlations including Fe-Fe, O-O, Fe-O, Fe-H, O-H and H-H, but the proton correlations are neglected here for clarity (they are very small compared to other contributions). Contributions shown are Fe-Fe (solid line), Fe-O (short dash line), and O-O (long dash line). From Waychunas et al. (1996).

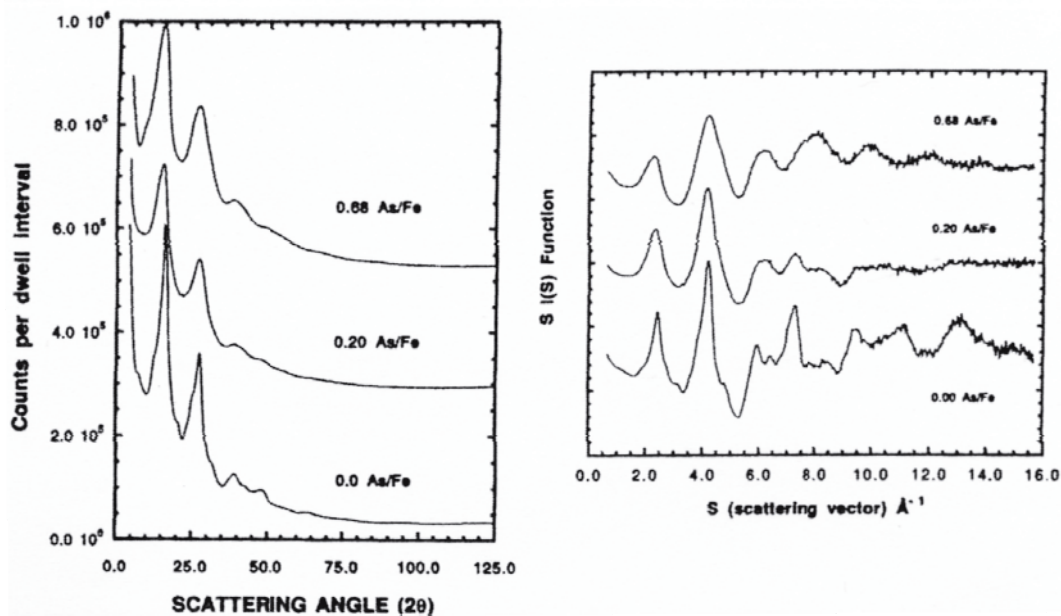


Figure 23. Example of WAXS scattering analysis for ferrihydrite particles with sorbed arsenate. Left: Raw scattering data for ferrihydrite prepared with coprecipitated arsenate in different proportions. Right: SI(S) function extracted from the scattering data. From Waychunas et al. (1996).

parameters than can be measured even with Rietveld analysis. This is also the case for applications of the Debye equation as smaller nanocrystals will have broadened patterns with overlapping features, yielding progressively greater structural ambiguity. With DFA pre-calculated patterns as a function of crystallite size and structure are added to produce the best fit with observations (Fig. 24). The method has been useful in identifying the

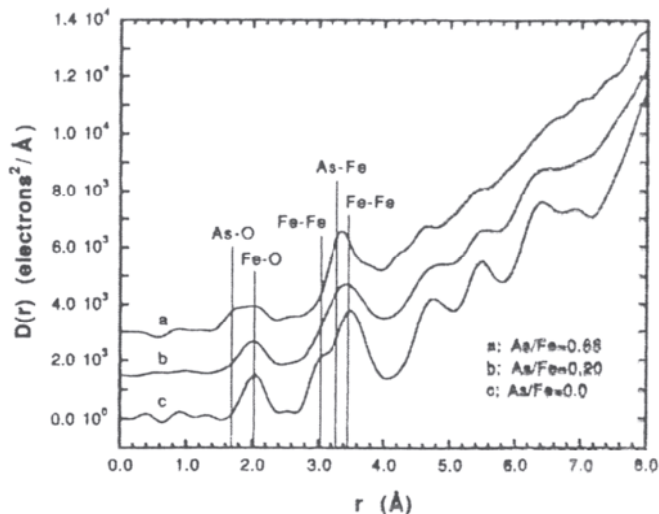
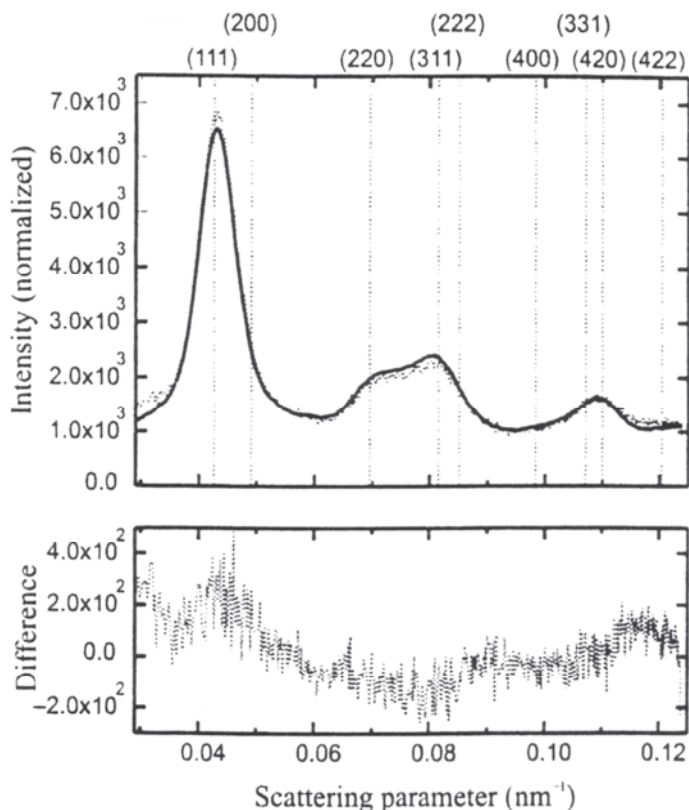


Figure 23, continued. Example of WAXS scattering analysis for ferrihydrite particles with sorbed arsenate. RDFs calculated from the SI(S) functions. The loss of higher frequency oscillations in the SI(S) function indicates loss of longer-range correlations in the RDF. The highest arsenate ferrihydrite particles are about 1 nm in diameter. From Waychunas et al. (1996).

Figure 24. Debye function analysis done on a colloid of 2-nm gold particles. Solid line is the fit using icosahedral and dodecahedral nanoparticles. Dotted vertical lines indicate FCC structure peak positions. Essentially no FCC or cuboctahedral particles are present. The bottom plot shows the difference between calculation and observation. From Zanchet et al. (2000), used with permission of Wiley-VCH.



presence of multiply twinned particles (MTPs) in nanoparticle diffraction patterns (Zanchet et al. 2000).

Short range order: X-ray absorption spectroscopy (XANES and EXAFS)

X-ray absorption spectroscopy is a powerful tool for nanoparticle analysis due to its selectivity and independence of sample physical state. It is limited in range to the region within about 0.5-0.7 nm of a particular (chosen) absorber atom in the structure, but can be applied to amorphous or even liquid samples. The basic theory behind the origins and analysis of the extended X-ray absorption fine structure (EXAFS) has been well described by Sayers et al. (1970, 1971) and Lee et al. (1981), with mineralogical applications detailed by Brown et al. (1988). The crucial aspect of the EXAFS spectrum is that it is formed by an electron backscattering process in the vicinity of the absorber

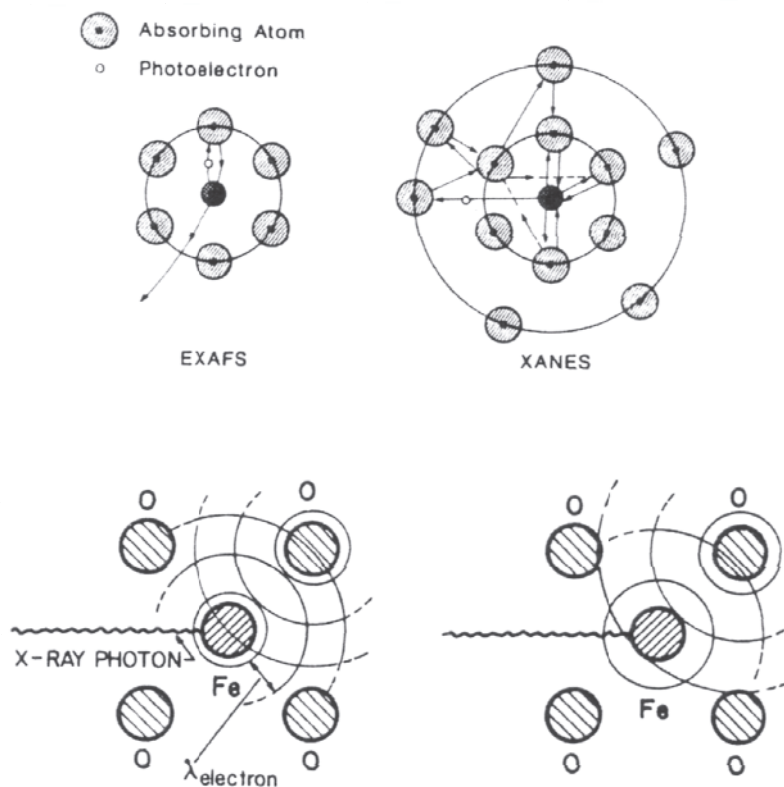


Figure 25. Cartoons showing the fundamental processes giving rise to the EXAFS and XANES spectra. Top left: EXAFS process. The ejected inner shell electron scatters off of a single backscatterer before returning to interfere with the outgoing electric wave at the absorber. Top right: XANES process. At electron kinetic energies close to the edge, the photoelectron has a large mean free path. Hence scattering off of several neighbors and over a large range of pathways is likely. This effect damps out quickly with increasing energy away from the absorption edge. After Calas et al.(1987). Bottom: interference process in EXAFS. The photoelectron leaves the absorber atom as a wave train that interferes with its own reflection off of neighbor atoms. Left: destructive interference. Right: constructive interference. From Brown et al. (1988).

atom. At the absorption edge the energy threshold for ionization of an atomic electron is reached. At energies above the edge the ejected electron leaves the absorber atom as a photoelectric wave with kinetic energy equivalent to the difference in edge and incident X-ray energies. In the EXAFS range of about 30 eV or more above the edge, the photoelectric wave scatters (mainly) only once from neighboring atoms with the backscattering wave interfering with the outgoing wave at the absorber. This interference modulates the absorption spectrum with a sinusoidal oscillation whose frequency depends on the absorber-neighbor distance. Hence embedded in the EXAFS spectrum is the scattering pattern associated with the local structure near that absorber (Fig. 25). The EXAFS spectrum is analyzed in a manner analogous to the X-ray diffuse scattering as per the Debye equation. The spectrum is extracted and suitably normalized to the sample composition, then converted to a scattering function by converting from energy to momentum space. The wavevector in this case is not S , but k : $k = [0.262 (E - E_0)]^{1/2}$, where E is the incident X-ray energy, and E_0 is the energy at the edge corresponding to zero photoelectron kinetic energy. Typically the quantity $k^n I(k)$ is Fourier transformed, with $n = 2$ or 3 depending on the weighting desired. Figure 26 shows a typical sequence of analysis from raw absorption edge spectra to Fourier transform. It is important to note

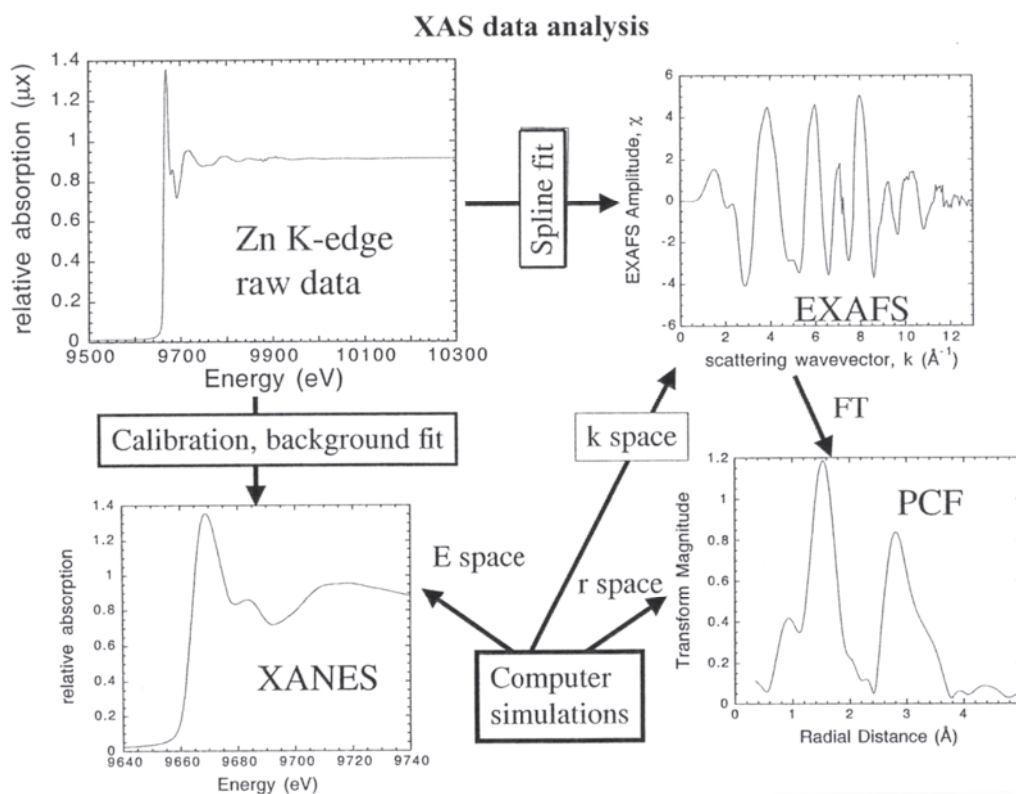


Figure 26. EXAFS and XANES analysis scheme. Top left: Raw data with background removed. Top right: Fit of EXAFS region with cubic spline and subtraction yields EXAFS oscillations; shown is the EXAFS weighted by k^3 . Bottom left: XANES spectral region expanded. Bottom right: PCF or pair correlation function (also called Radial Structure Function to distinguish it from the X-ray analog RDF); shown is the Fourier transform of the spectrum at the top left.

with EXAFS analysis that the Fourier transformed function is not a typical RDF, though it is similar. The difference comes from the phasing of the scattering process creating the EXAFS features. This is an electron backscattering process that is affected by local atomic fields, and hence the frequencies of backscattering from a given absorber-neighbor atom pair are shifted from values directly proportional to the distances. This means that the peaks in the Fourier transform do not occur at the actual absorber-neighbor distances. In practice, these distances are accurately obtained by fitting the raw EXAFS data with model functions that closely estimate the phase changes during scattering. For clarity we call the EXAFS-derived ‘RDF’ a radial structure function or RSF. There is no analogous phase shift effect with X-ray scattering.

Examples. One use of EXAFS analysis takes advantage of the total reflection of X-rays off of a sample surface at small incidence angles to examine only the surface of the sample. This method is particularly useful for examination of the structure of nanoprecipitates at the surface. Such a study is one by Waychunas et al. (1999) where nanoparticles of iron oxide were studied on quartz single crystal surfaces. In this study the iron oxide particles were found to be highly textured, with a particular crystallographic direction always normal to the quartz surface. As EXAFS spectra are collected with X-ray synchrotron radiation, which is highly plane polarized, it was therefore possible to collect K-edge EXAFS spectra with X-ray electric vector both in the plane of the particles and normal to this plane (Abruna 1991). This yielded two different but complementary EXAFS spectra that could be analyzed to yield additional structural information. This process is shown in Figure 27, where the RSFs for different types of

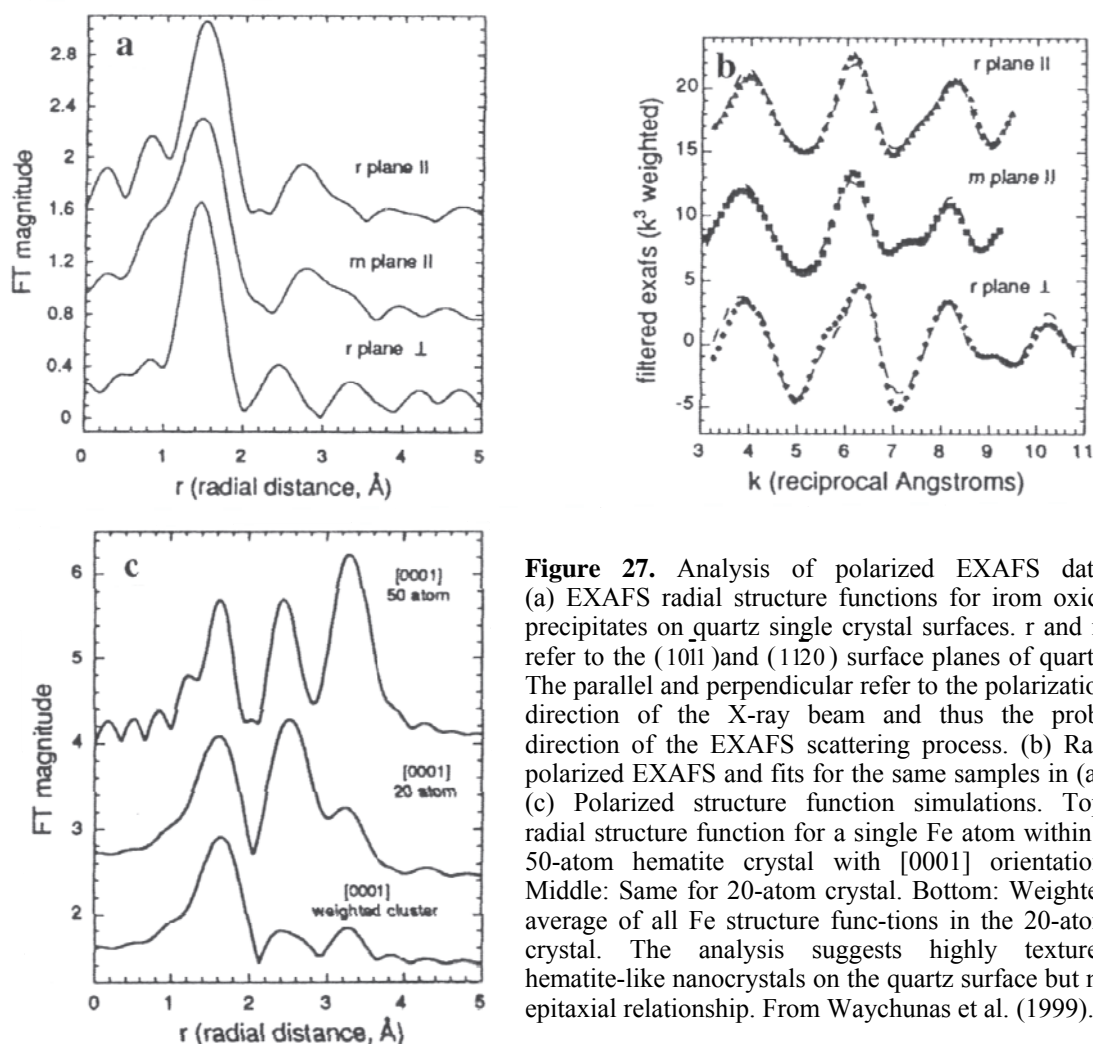


Figure 27. Analysis of polarized EXAFS data. (a) EXAFS radial structure functions for iron oxide precipitates on quartz single crystal surfaces. r and m refer to the (1011) and (1120) surface planes of quartz. The parallel and perpendicular refer to the polarization direction of the X-ray beam and thus the probe direction of the EXAFS scattering process. (b) Raw polarized EXAFS and fits for the same samples in (a). (c) Polarized structure function simulations. Top: radial structure function for a single Fe atom within a 50-atom hematite crystal with [0001] orientation. Middle: Same for 20-atom crystal. Bottom: Weighted average of all Fe structure functions in the 20-atom crystal. The analysis suggests highly textured hematite-like nanocrystals on the quartz surface but no epitaxial relationship. From Waychunas et al. (1999).

particles are shown. Through careful analysis it could be shown that the precipitate particles had structures similar to α -Fe₂O₃, with their crystallographic [0001] directions normal to the quartz surfaces. Additionally, the amplitudes of the peaks in the RSF could be used to deduce the particle size and shape. This is possible as a bulk crystal of α -Fe₂O₃ has 13 Fe next-nearest-neighbor atoms about a given Fe atom, with different Fe-Fe distances as a function of direction. These correlations give rise to well defined peaks in the RSF. However in small particles, the surfaces will have much smaller numbers of Fe-Fe neighbors, and hence the RSF peak amplitudes will be affected. This type of analysis to deduce particle or crystallite size works well in the 0.5- to 3-nm size range, and in this case showed the precipitates to be about 1 nm in size.

Another example of nanoparticle size analysis via EXAFS is the work of Frenkel (1999) on Pt and Pt-Ru particles supported on carbon. This study utilizes the longer absorber-neighbor distances within nanocrystals, showing that determinations of the relative numbers of these farther neighbors are more sensitive to crystallite size than closer neighbors. In the best case all neighbor coordinations can be used to obtain a good estimate of crystallite size and shape even without the added information provided by polarized studies (Fig. 28).

A large number of EXAFS studies have been done on semiconductor materials. For example, Rockenberger et al. (1997) examined nanocrystals of CdS in the range 1.3 to 12 nm in diameter with different types of surface stabilizing agents. Thiol-capped

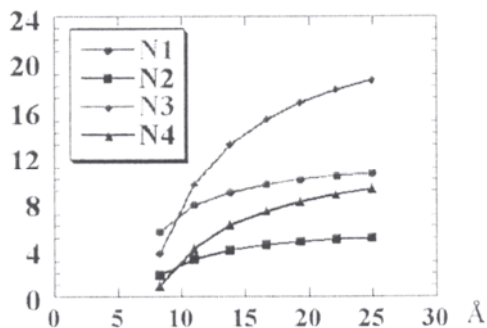
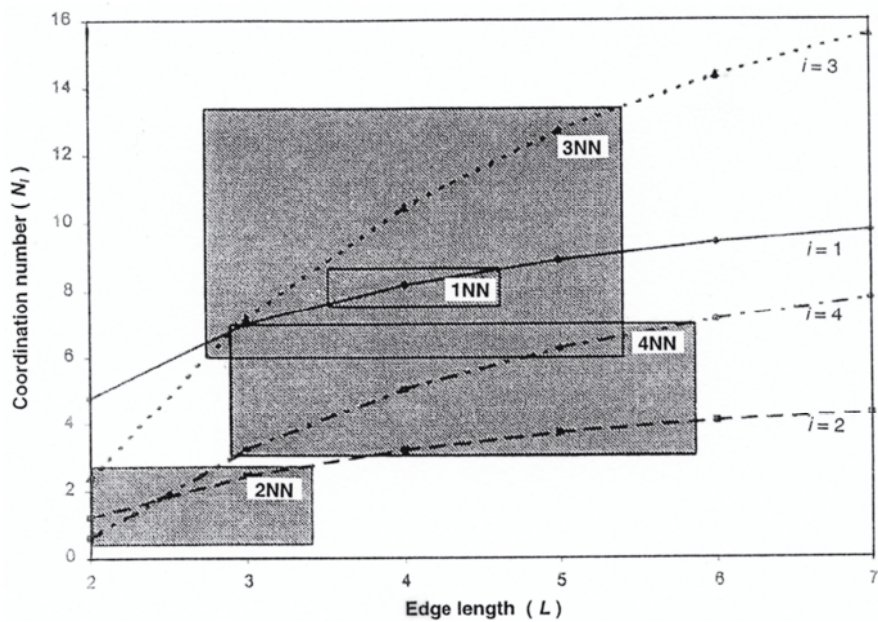
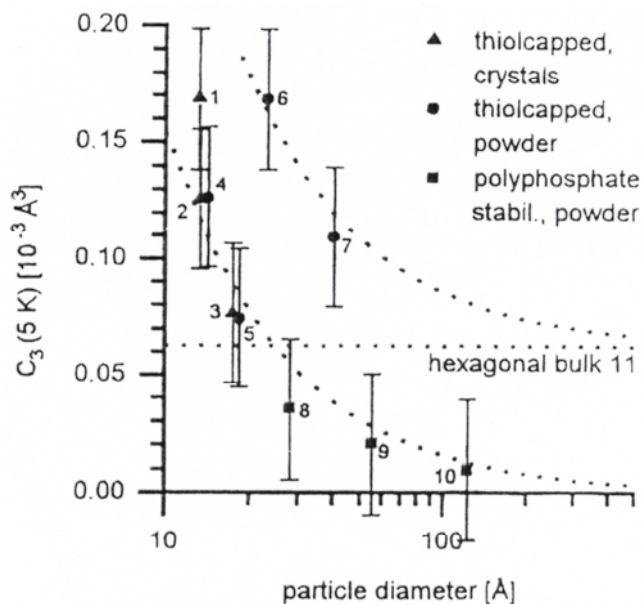


Figure 28. Top: EXAFS analysis strategy used by Frenkel (1999) to determine nanocrystal size in metal particles. The number of observed neighbors is dependent on the crystallite size. The more distant neighbors provide the most sensitive measure of coordination number and thus crystallite size. Bottom plot is the analogous function for semiconductor tetrahedrally coordinated structures. After Frenkel (1999).

nanoparticles had an expanded mean Cd-S distance, while polyphosphate-capped nanoparticles were slightly contracted. As the expected effect is one of contraction, Rockenberger et al. (1997) attributed the differing behavior to steric hindrances among the thiol groups, whereas the polyphosphate groups had no such steric interaction. The EXAFS analysis showed further that static disorder (see next section) increased in the nanoparticles, with a maximum for particles with 3-nm diameters. It was suggested that this size corresponded to the largest thermodynamically-grown nanocrystals, which enlarged further only via Ostwald ripening or aggregation. Fitting of the EXAFS-derived pair distribution function for the Cd-S bonds using a cumulate expansion allowed measurement of the anharmonicity of these distributions. A plot of the third cumulate term vs. decreasing particle diameter showed two distinct trends, one attributed to cubic (sphalerite) structure where the cumulate value increased from zero at large particle size, and a second where the cumulate value increased from a finite value. This latter trend was attributed to hexagonal (wurtzite) structure (Fig. 29). As Cd-X pair correlations are nearly identical between these two structures, the anharmonicity variation with particle diameter is possibly the only clear method for distinguishing these structures in small nanocrystals.

Carter et al. (1997) used EXAFS and other measurements to study the surface structure of CdSe nanocrystals. They found that the Se-Cd coordination number varied with particle size and that Se was only coordinated by Cd. This indicated that surface Se atoms do not have all bonds satisfied, and might lead to special optical properties of these nanocrystals.

Figure 29. Trends of third cumulate as a function of nanocrystallite diameter for sphalerite and wurtzite structures. The bulk wurtzite-structure material has finite C_3 value which increases with decreasing size, while the sphalerite structure has a zero C_3 value for bulk. These differences allow discrimination of these two structure types in nanoparticles. From Rockenberger et al. (1997), used with permission of the editor of the *Journal of Physical Chemistry*.



Rockenberger et al. (1998) examined 1.8-nm nanocrystals of CdTe capped with mercaptoethanol molecules, and thus having surface CdS bonds. They found that the surface CdS local structure was distorted relative to the bulk CdTe, and attributed this to strain because of the differences in CdTe and CdS bonding. The coordination numbers derived from the EXAFS analysis were consistent with models of individual nanocrystals with discrete stoichiometries, e.g., $\text{Cd}_{54}\text{Te}_{32}(\text{S-ethanol})_{52}^{8-}$.

Disorder problems in EXAFS analysis

The advantage of EXAFS is that it can often be employed where other structure probes cannot. The standard EXAFS equation has a term for the loss of amplitude with increasing scattering vector. It has the form

$$DW = e^{-2k^2\sigma_i^2} \quad (21)$$

This term essentially uses a Gaussian distribution function, i.e., it holds exactly for a “harmonic” distribution or a “harmonic” set of bond vibrations. For static cases this means that the distribution of N-x bond distances needs to approximate a Gaussian function. For vibrational disorder this means that the vibrations must not be so large that the harmonic part of the potential function (the trough in the potential energy vs. bond length plot) is breached. Such larger vibrations lead to “anharmonic” vibrations where there is a net change in atom mean positions. Figure 30 shows a worst case scenario for extreme anharmonicity. In the example a sharp Gaussian distribution at a shorter interatomic distance is shown to dominate a similar function with an additional Gaussian broad “tail.” The entire coordination data contained in the tail would be lost with typical EXAFS analysis. For most cases that are not so severe, the EXAFS can be fit using a cumulate moment expansion to model the distribution function, without any tacit assumption of harmonicity (Gaussian) distributions. With the cumulate expansion, the EXAFS DW term has the form:

$$DW(\text{cumulate}) = e^{-2k^2\sigma_i^2 + \frac{2}{3}\sigma_i^4 k^4 \dots} \quad (22)$$

where we now have an exponential in even-order terms of the cumulate expansion. This alone indicates a different kind of amplitude decay with increasing k. However the phase is also affected so that one has:

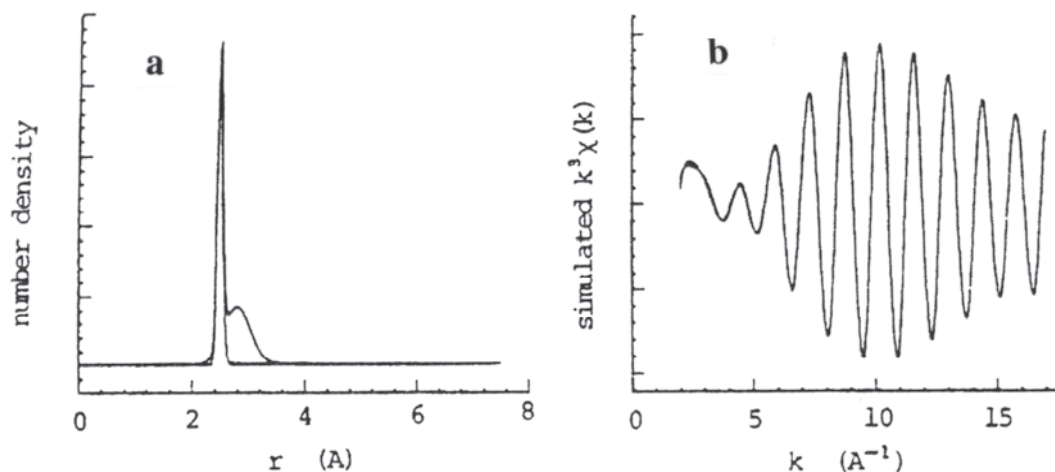


Figure 30. Effect of extreme static disorder in EXAFS analysis. Left: Gaussian distributions of equal area but with much different widths. Both the sum of the two functions and the single narrow distribution function are shown. Right: Simulated EXAFS functions for the functions at left. It is seen that there is no detectable difference in the EXAFS except at low k -values. This difference would overlap with XANES and be extremely difficult to analyze. Hence physical distributions with a broad “tail” will have reduced coordination numbers via standard EXAFS analysis, as well as an artificially produced distance “contraction”. For cases not as severe as this, cumulate analysis can quantify the degree of static disorder and allow more correct results. After Kortright et al. (1983).

$$\chi \propto \sum_i F_i(k) \sin \left[2kr_i - \frac{4\sigma_i^2 k}{r_i} \left(1 + \frac{r_i}{\lambda} \right) - \frac{4}{3} \sigma_i^3 k^3 \dots \right] \quad (23)$$

All this means is that a non-Gaussian distribution function will cause a different damping rate of the EXAFS amplitudes, and a shift in the apparent r values of neighbor distances. The third cumulate is the most reliably calculated and gives a good estimate of anharmonicity for cases without extreme anharmonicity (Tranquada and Ingalls 1983). In favorable cases the EXAFS cumulate moment analysis can predict anharmonicity-based distance effects in first and second neighbor about an absorber atom. The method is difficult to apply to complex many-atom systems. Hence EXAFS analysis of very disordered nanoparticles or mineralogical solids must be done with caution.

Empirical and *ab initio* XANES analysis

The structure very close to the X-ray absorption edges is called the X-ray absorption near edge structure or XANES. This region contains both electronic transitions within the absorber atom (called bound state transitions and just below the E_0 energy), and multiple scattering features. The latter are due to the very long mean free paths of electrons (e.g., hundreds of Å) that are ejected from the atom just above the edge energy, i.e., with little kinetic energy. These electrons can scatter around the local area of the absorber atom producing absorption features on the edge each linked to a particular MS path. As with other types of scattering already discussed, MS also produces a sinusoidal modulation, but this is damped out quickly due to the strong dependence of MS amplitude on k . Thus most significant MS features are observed on the absorption edge proper. Such features may partially cancel one another so that the XANES is not easy to interpret in terms of structure except via *ab initio* XANES model calculations. However, the sensitivity of the MS and electronic absorption features to absorber valence, coordination number and neighbor distances can be used to empirically determine these quantities if closely similar model compound spectra are available for comparison. The great advantage of XANES analysis is that the XANES carry a large amount of structural information over a small

energy range, and are often of much larger amplitude than the EXAFS. Hence for small quantities of samples, XANES information is much more easily measured.

An example of an empirical study is that of Chen et al. (1999) where some of the structural details of TiO₂ nanoparticle surfaces can be deduced from progressive changes in the XANES. Past work has shown that the position (energy) and intensity of the electronic absorption features on the low energy side of the Ti K-edge can be interpreted in terms of valence, coordination number and Ti site distortion (Farges 1997; Waychunas 1987). Chen et al. (1999) showed that smaller TiO₂ particles had intensification of these features, consistent with increased Ti-site distortion on the surface of the particles. EXAFS analysis was also done and indicated a higher concentration of 5-coordinated sites on the TiO₂ particle surfaces, which was consistent with the XANES interpretation (Fig. 31).

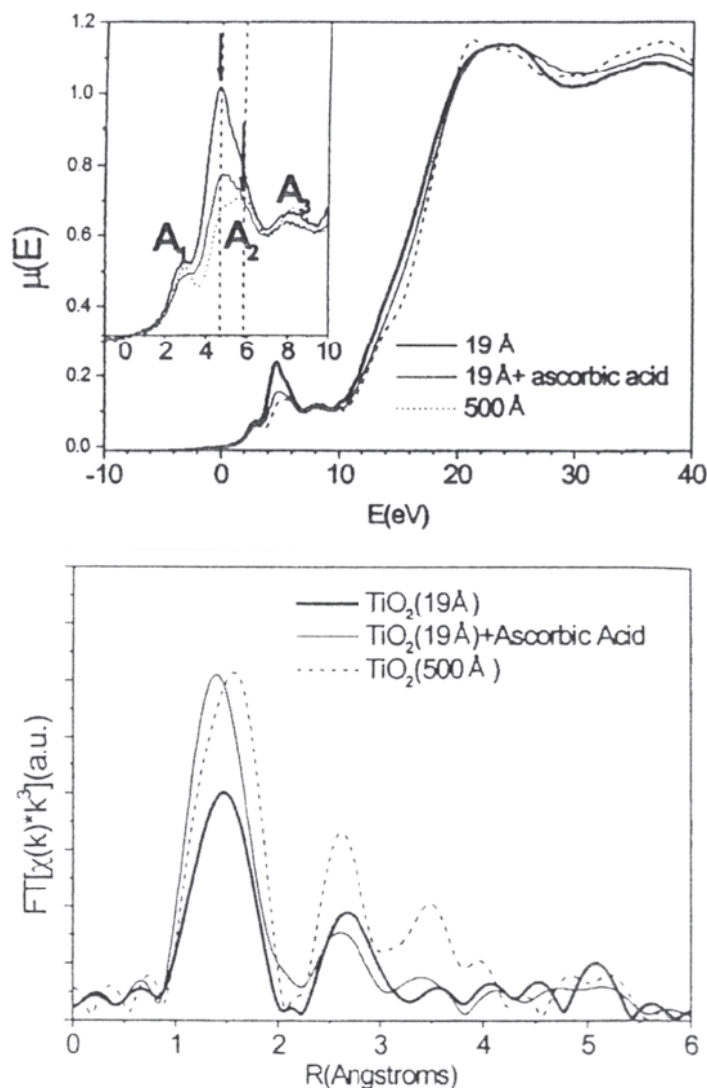


Figure 31. XANES and EXAFS analysis of the surface structure in 1.9-nm nanoparticles of TiO₂. Top: XANES analysis focussing on the “pre-edge” region. Intensification of the features in this region are consistent with distorted or reduced Ti coordination. Bottom: EXAFS analysis shows reduced peak area and coordination in the same samples with XANES intensification. Both analyses point to 5-coordinated Ti on particle surfaces. Capping the particles with ascorbic acid removes the distorted sites. After Chen et al. (1999).

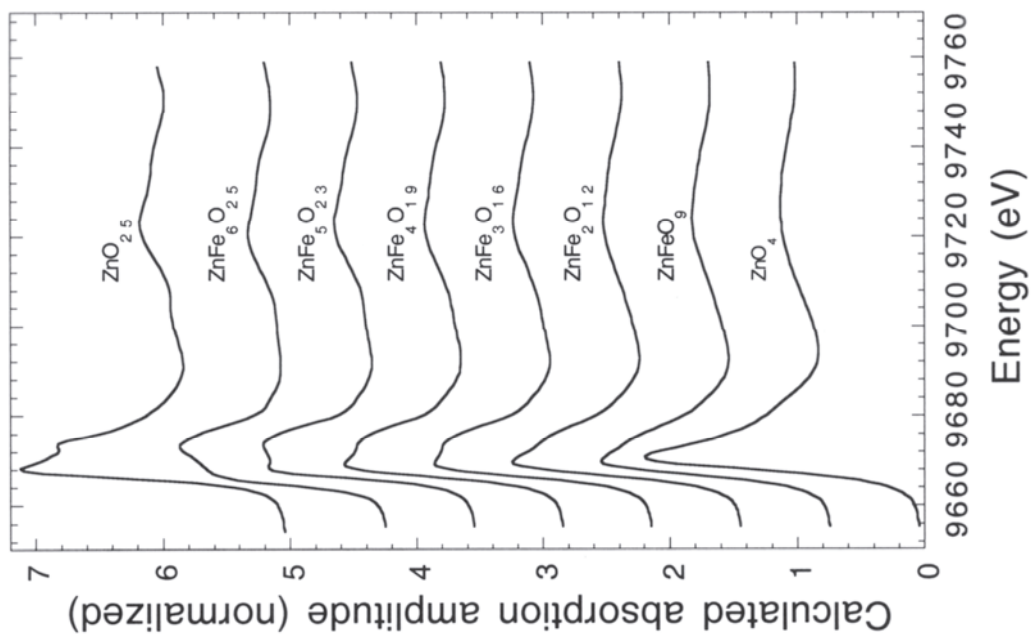


Figure 32. Zn MS calculations and XANES. Left: Small cluster of Fe oxyhydroxide polymers with sorbed tetrahedral Zn^{2+} complex. Two of the multiple scattering paths are shown that vary in number as a function of cluster size. Similar dependencies of other MS paths create non-linear changes in XANES features as a function of cluster size. Right: Calculated XANES for various clusters as depicted at left. All MS paths used in a self-consistent calculation (Feff 8). From Waychunas et al. (2001)

An example of the use of *ab initio* XANES calculations to determine nanoparticle structure is the Zn/ferrihydrite sorption system examined by Waychunas et al. (2001). In the case of sorption complexes the XANES spectrum of the sorbed species will contain information about the local structure of the substrate, and thus the structural nature of the full sorption complex. In the Zn/ferrihydrite system it was observed via EXAFS that the number of Fe³⁺ next nearest neighbors about the sorbed Zn ion decreased as the Zn sorption density increased. Direct calculation of the XANES structure identified MS paths that changed in number as a function of cluster size (and thus number of neighbor Fe atoms), and gave rise to XANES features that changed in intensity (Fig. 32). These changes agreed well with the structural interpretation of the EXAFS and the crystal chemistry of Zn-Fe³⁺ hydroxides.

Size and shape determination—X-ray and neutron small-angle scattering (SAXS and SANS)

The scattering relationships discussed earlier indicated a reciprocal relationship between scattering angle and r , the separation of scattering elements. This can be seen by combining the Bragg relation (Eqn. 14) with Equation (18). Substituting $2d \sin\theta$ for λ in Equation (16) and cancelling the $\sin\theta$ yields $2\pi/d = S$. Thus the larger the spacing the smaller the value of S , and the smaller the scattering angle for any given λ . If scattering angles down in the millidegree range can be measured, length scales in the micron range can be detected. At scales such as this, atomic scattering centers are not individually sensed, structure factors are not sensitive to order, and only form factors are important. Thus only large scale electron density differences are detected. Hence the size and shape of colloids, nanoparticle aggregates and large molecular units can be determined, though there is little sensitivity to crystallinity.

The two important factors that mitigate the intensity of scattering are the structure factor $F^2(S)$ and the form factor sometimes indicated as $P(S)$. The structure factor describes the external relationships of scattering elements, such as atoms, and hence the phasing and interferences of the net scattering. The form factor describes the internal distribution of electron density within a scattering element, and thus mitigates the intramolecular or intraparticle scattering. In our discussion earlier the only form factor mentioned was the atomic scattering factor, f . To a reasonable approximation all atoms have identical f values as a function of scattering angle, and scaling as the atomic number (number of electrons). However for small angle scattering the structure factor has little importance and we concentrate on detailed evaluation of the form factor.

In the small angle regime there are subsets of specific scattering phenomena that can be identified and analyzed. These are the center-of-mass region, the Guinier region, the Fractal region, and the Porod region (Fig. 33). In the center-of-mass region, at the smallest measurable scattering angles, the size of S is such that very long lengths are being probed by the scattering. These are much larger than the size of the particles or aggregates, and thus only an averaged electron density of a particle can be sensed. There is no interparticle interference phenomena here. Analysis of this region gives a rough average idea of particle size. In the Guinier region at somewhat larger S , there is some degree of intraparticle interference which enables analysis of the particle shape. Specifically what can be extracted is the radius of gyration, R_g , which is the electron density analog of the second moment of inertia. Guinier's (1963) approximate expression for the scattering in this region is:

$$I(S) = N_p n_e^2 \exp(-S^2 R_g^2/3) \quad (24)$$

where N_p is the number of scattering units, and n_e is the number of electrons per unit. A plot of $\log I$ versus S^2 can be used to identify R_g , and give information on the mean

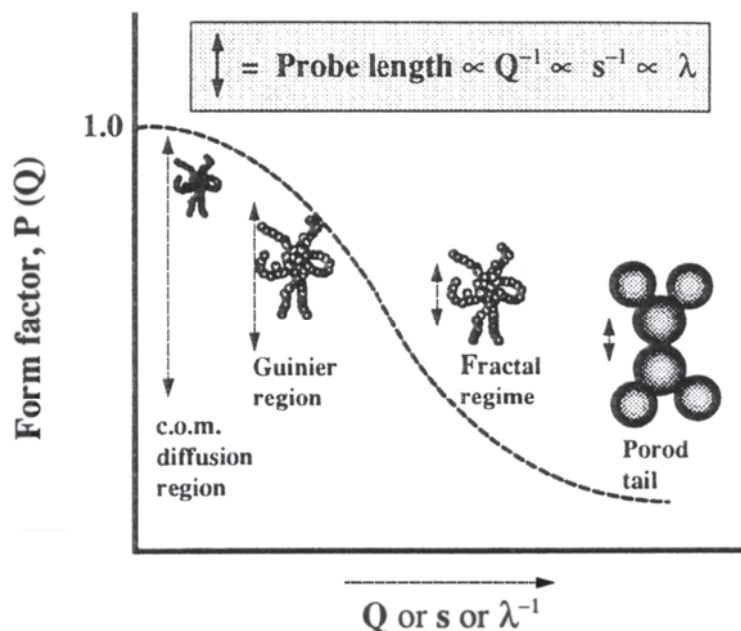


Figure 33. Regions within the small angle scattering regime that are sensitive to differing types of structures and organization. C.O.M. refers to “center of mass” region. From Hiemenz and Rajagopalan (1997), used by permission of Marcel-Dekker.

shapes of the nanoparticles. For example, if R_s is the radius of a spherical particle, the appropriate R_g is equal to $3R_s/5$. In the case of a thin rod of length R_l , R_g is equal to $R_l^2/12$. The Guinier approximation was derived for spherical particles that are highly dispersed, and is less accurate for needle-like particles and dense solutions. At values of S above the Guinier region, the fractal nature of a particle becomes important in creating interference effects. Here the probe length is consistent with aggregate size, but is much larger than the primary particles in the aggregate. Figure 34 shows a conceptual diagram of the fractal region. It can be shown that the plot of a $\log I(S)$ versus $\log S$ function is linear in this region if there is self-similarity independent of size. The slope in such a plot yields the exponent of S , which is equivalent to the fractal dimension of the aggregate. The region of largest S or Porod region has the largest falloff in SAXS intensity with S . This tail region can be used to extract the surface area of nanoparticulates using Porod’s Law:

$$I(S) = I_e 2\pi \rho^2 A/S^4 \quad (25)$$

where A is the average particle surface area, r is the electron density difference between particle and matrix, and I_e is a constant. From the combined analysis of these regions, along with analysis of scattering from still longer wavelengths such as light, a considerable amount of information can be obtained about particle size, shape, area and size distribution.

Determination of particle size distributions

Particle size distributions are important information for evaluating the synthesis, growth and kinetics of formation of nanoparticles and nanoparticle aggregates. The main contrasting techniques are imaging via TEM, and SAXS analysis. TEM analysis is independent of the type of aggregation, shape and size of nanoparticles, whereas SAXS interpretation requires assumptions about the nature of the sample. On the other hand, SAXS can be done on *in situ* systems, and often in real time during particle formation.

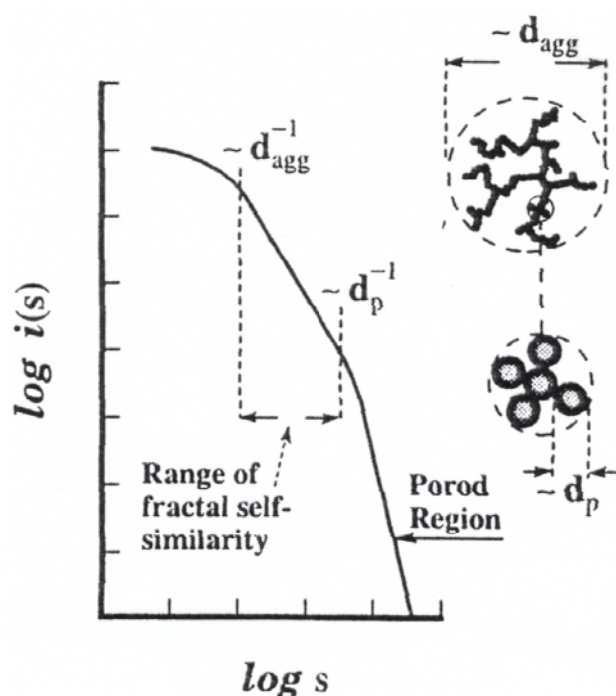


Figure 34. Cartoon showing the SAXS region where self-similarity within aggregates can be detected. Fitting of this region can reveal the fractal dimension of the aggregate, and if combined with analysis of other regions, yield information on the complete distribution function. From Hiemenz and Rajagopalan (1997), used by permission of Marcel-Dekker.

Further, there is no limitation imposed by having to dry and mount the sample, which may occasion aggregation or other physical change. A comparison of these techniques has been made by Rieker et al. (1999) on the same set of idealized hard silica sphere samples. For near-spherical particles that are dispersed and relatively dilute, it is possible to define a unique particle size distribution by fitting the Porod and Guinier regions of the SAXS pattern. Fits to experimental SAXS spectra are shown in Figure 35 compared to histogram distributions determined from TEM images. The SAXS-derived distributions were assumed to be Gaussian. The agreement is quite good, with most of the mismatch in mean particle size due to difficulty in accurately calibrating the TEM size distribution. Other comparisons of SAXS and TEM has been done on a wider set of nanoparticles including CaCO_3 , Fe_2O_3 , TiN and SiO_2 by Xiang et al. (2000) giving good agreement for highly dispersed particles, and by Turkovic et al. (1997) on nanophase TiO_2 , also giving good agreement.

Rate of growth/aggregation experiments with SAXS

Stopped or continuous flow reaction methods can be utilized with synchrotron-based SAXS measurements to determine reaction kinetics, including protein folding, nanoparticle growth, breakdown, and aggregation. Using a synchrotron X-ray source, the SAXS spectrum can be collected with a one or two dimensional detector with good quality in periods as short as 0.001 s.

A system such as this has been developed at the SRS at Daresbury, UK, that also allows simultaneous wide angle X-ray scattering and FTIR spectroscopy on the same sample. An example of this type of experiment has been described by Eastoe et al. (1998) where the breakdown kinetics of synthetic micelles was measured. Another study is that of Connolly et al. (1998) where the kinetics of superlattice formation from capped (by dodecanethiol) Ag nanocrystals was studied. The superlattice 111 reflection was monitored to determine growth rate and (111) plane spacing at 1 s intervals. A continuous reduction in (111) superlattice spacing with time suggested gradual solvent evaporation from the growing structure. Real time SAXS experiments of similar type are now also possible at SSRL, ESRF and other synchrotron sources. This type of technique is

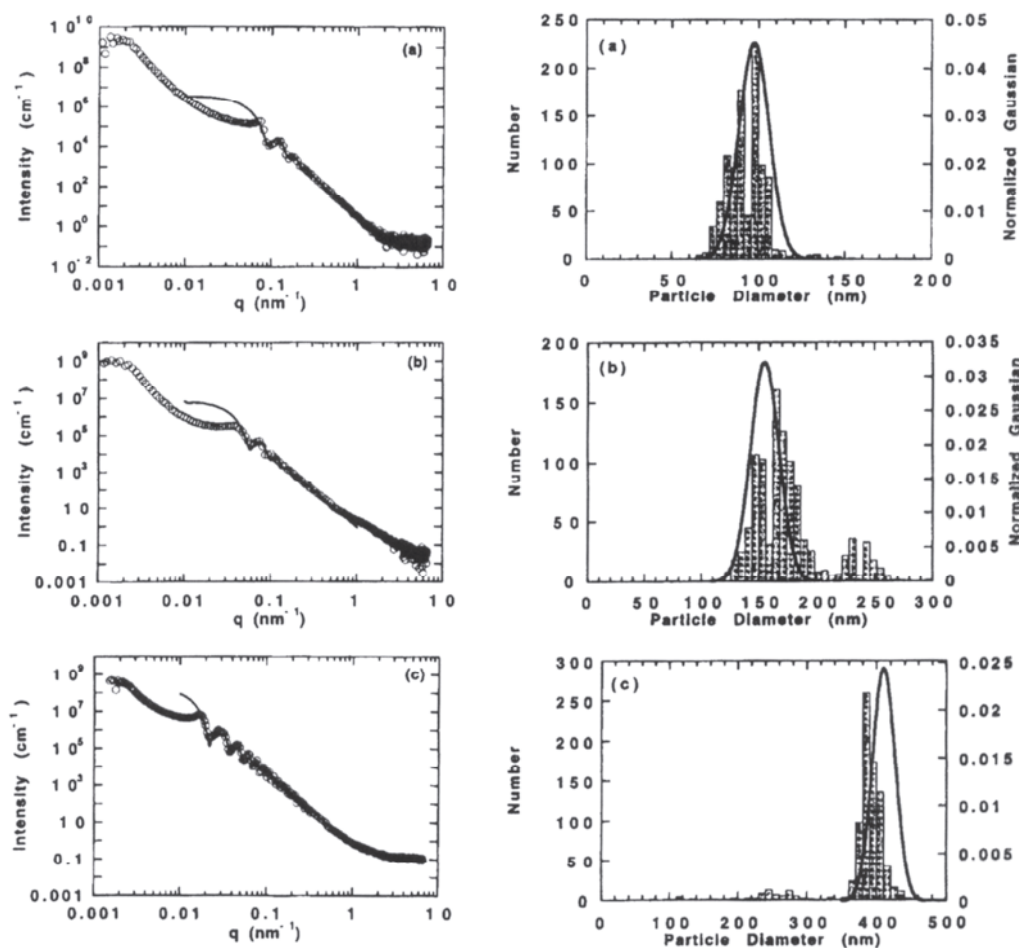


Figure 35. Comparison of distribution functions extracted from SAXS data versus from TEM observations. There are some systematic errors in the TEM analysis. However some larger scale particles appear to be lost in the SAXS analysis. As TEM particle counting favors larger particles this could also be a systematic effect. After Rieker et al. (1999).

especially valuable in studying nanomineral aggregation kinetics in aqueous solutions, or assembly of precipitated nanoparticles in biological systems due to the high electron density differences, and the intractability of other characterization approaches.

Small-angle neutron scattering (SANS)

SANS analysis is essentially the same as SAXS except that the length scales probed are somewhat different, and the intensity of scattering from atoms does not scale as the atomic number as with X-rays, but rather as a nuclear property that is effectively independent of atomic number. Additionally, the scattering factors, which are called neutron scattering lengths, can have negative values. This means that for some specific sample compositions it is possible to have net neutron scattering cross sections that are zero, a situation referred to as a “contrast match”. A seemingly unusual aspect of neutron scattering is that protons scatter as effectively as most other atoms, but with a much different (and negative) scattering length than deuterium. Hence polymer/solvent and biological systems can be adjusted with isotopic substitutions to remove scattering due to the surrounding solution, or the effects of substrates can be removed in the study of thin films. For mineralogical nanomaterials SANS can be used to selectively examine the proton distribution within and on the surface of particles, or as a complementary tool to SAXS analysis. A tutorial on SANS is presently available on the internet at www.isis.rl.ac.uk/largescale/log/documents/sans.htm.

SANS is useful in examining pore structures in nanoporous materials, or water in fractal networks (Li et al. 1994). Examples of aggregation-state analyses include studies of silica and titania nanoparticles (Hyeon-Lee et al. 1998), cationic surfactants (Brasher and Kaler 1996) and $\text{TiO}_2\text{-SiO}_2$ and $\text{ZrO}_2\text{-SiO}_2$ sol-gel materials (Miranda Salvado et al. 1996). Particle size distributions obtained via SANS, SAXS and TEM on nanophase $\text{TiO}_2\text{-VO}_2$ catalyst particles are compared by Albertini et al. (1993).

Light scattering techniques

Scattering of longer wavelength photons in the IR, visible and UV offers a number of advantages over X-ray and neutron scattering. First, the wavelengths are substantially longer so that very long length scales can be probed at technically feasible scattering angles. The range of possible scattering vector, S , overlaps and extends that available with SAXS by two orders of magnitude. Second, these wavelength light sources can be made exceedingly bright, monochromatic and coherent using lasers. Both of these conditions enable static light scattering (SLS), and photon correlation spectroscopy (PCS). A third desirable attribute is that the scattering can readily be done in solutions, i.e., *in situ*, which can be more problematic for SANS and SAXS. [PCS is also known as dynamic light scattering or DLS.] SLS is applicable to the study of nanoparticles in the 10-1000 nm regime, while SAXS mainly is used for the 1-50 nm range. The scattering equations are essentially the same for each technique, except that scattering contrast comes from the electron density differences in SAXS, while it comes from refractive index differences in SLS (Chu and Lu 2000). A comparison of the range for S and scattering lengths of different techniques is shown in Table 2.

Table 2.

<i>Method</i>	<i>Wavelength (nm)</i>	<i>S range (nm⁻¹)</i>	<i>Length scale (nm)</i>
SLS/PCS	360–1000	0.001–0.2	1000–5
FPI	400–600	Not applicable	10–1
SAXS	0.05–0.3	0.02–1.0	50–1
WAXS	0.15–0.15	0.6–7.0	1.6–0.14
SANS	0.4	0.007–0.9	150–1
WANS	0.4	10–50	0.1–0.02

PCS (DLS) measures the fluctuations in the intensity of light scattering with time. The decay rate of the time autocorrelation function of these intensity fluctuations is used to directly measure particle translational diffusion coefficients. This can then be related to the particle's hydrodynamic radius. If particles are approximately spherical, then the hydrodynamic radius is equivalent to the geometric radius. Because of its sensitivity and ease of use, PCS is widely used to determine the sizes of small particles (Pecora 2000). As with all scattering methods, distributions of particle size and shape places limits on what can be extracted from PCS data. Currently the analysis method most common is based on an assumption that the time correlation function is essentially a sum of exponential decay times, where each decay rate relates to a different particle diffusion coefficient. The logarithm of such a function can be expanded as a power series in time, with coefficients equal to K_n , known as cumulants. As with our earlier discussion of disorder in EXAFS analysis, K_1 is equal to the average value of the exponent, the reciprocal relaxation time in this case. K_2 is a measure of the dispersion of the reciprocal relaxation time about the average, and so forth. If K_2 and higher cumulants are 0, then there is a single exponential term in the correlation function and a single diffusion rate. Examples of distributions in nanoparticle samples obtained via PCS are given in Kaszuba

(1999). PCS techniques are currently being expanded into the X-ray range (XPCS), e.g., Thurn-Albrecht et al. (1999).

An alternative to PCS is Fabry-Perot interferometry (FPI) which is applicable to particles with considerable geometric anisotropy. FPI uses the frequency broadening of the laser light to determine the rotational diffusion coefficient, and this is related to the particle dimensions. The FPI system is essentially a very high resolution monochromator system that disperses the scattered light into component frequencies. A typical frequency range is 1 MHz to 10 GHz. The incident beam must be efficiently linearly polarized in the plane perpendicular to the scattering plane, and the scattered radiation taken off at right angles to the incident beam to block all light that has not been scattered and depolarized. Hence particle rotation must result in depolarization to be detected, and this is the case only when there is a polarizability change as the particle rotates relative to the incident beam.

“INDIRECT” STRUCTURAL METHODS

Optical spectroscopy (IR, visible, UV, Raman, luminescence, LIBD)

Investigation of the IR-Vis-UV spectrum of nanoparticles can yield considerable information about physical and electronic structure of the materials. IR spectroscopy is mainly useful for examining the bending and stretching vibrational modes of particular molecular units within the particles, e.g., surface dangling bonds or low coordination species, adsorbed or bonded water, and passivating organic coatings. An example of the use of FTIR is the verification of unterminated Se atoms on the surface of CdSe nanoparticles in agreement with EXAFS analysis (Carter et al. 1997). Semiconductor nanoparticles are commonly studied in the UV-Vis range where band gaps and localized electronic states can be probed with such wavelengths. One of the interesting phenomena found in semiconductor materials in this size range is that of “quantum confinement.” This means that as particles are reduced in size the delocalization of electrons within energy bands is restricted by the physical size. As delocalization reduces electronic energy, confinement increases electronic state energies and gives rise to an increased HOMO-LUMO (highest unoccupied/lowest unoccupied molecular orbital) gap. The gap energy is roughly equivalent to the energy where absorption begins to increase, presumably via transitions to an exciton state just within the gap. This is well exemplified in CdS nanoparticles (Rockenberger et al. 1997) and CdSe nanocrystals (Carter et al. 1997; Murray et al. 1993), spectra of the latter being shown in Figure 36. Further, as particles decrease in size the absorption spectrum becomes increasingly structured with sharper features, due to a progressive change from a band-like electronic structure to a molecular-like electronic structure. The quantum confinement effect also operates in insulator nanocrystals such as the anatase form of TiO₂ (Reddy et al. 2001). See the chapter by Jacobs and Alivisatos for more details concerning the quantum confinement phenomenon. The nature of particular transition metal sites can often be characterized by interpretation of the IR-Vis electronic absorption spectrum, e.g., determining the distortion of a site due to strain or unusual coordination at a surface that shifts the 3d or other absorption band positions. Interactions between metal ions, and ligand-metal charge transfer can also be evaluated with electronic absorption spectroscopy. However this type of study is possible mainly for transition metal doped semiconductors or insulators, such as TiO₂ and Al₂O₃, and does not appear to have been explored with such types of nanocrystals to date.

A consequence of absorption in the ultraviolet for many nanocrystals is the emission of the absorbed light as luminescence. In these cases, photoluminescence spectroscopy can yield both electronic structure information as well as details of excited electronic

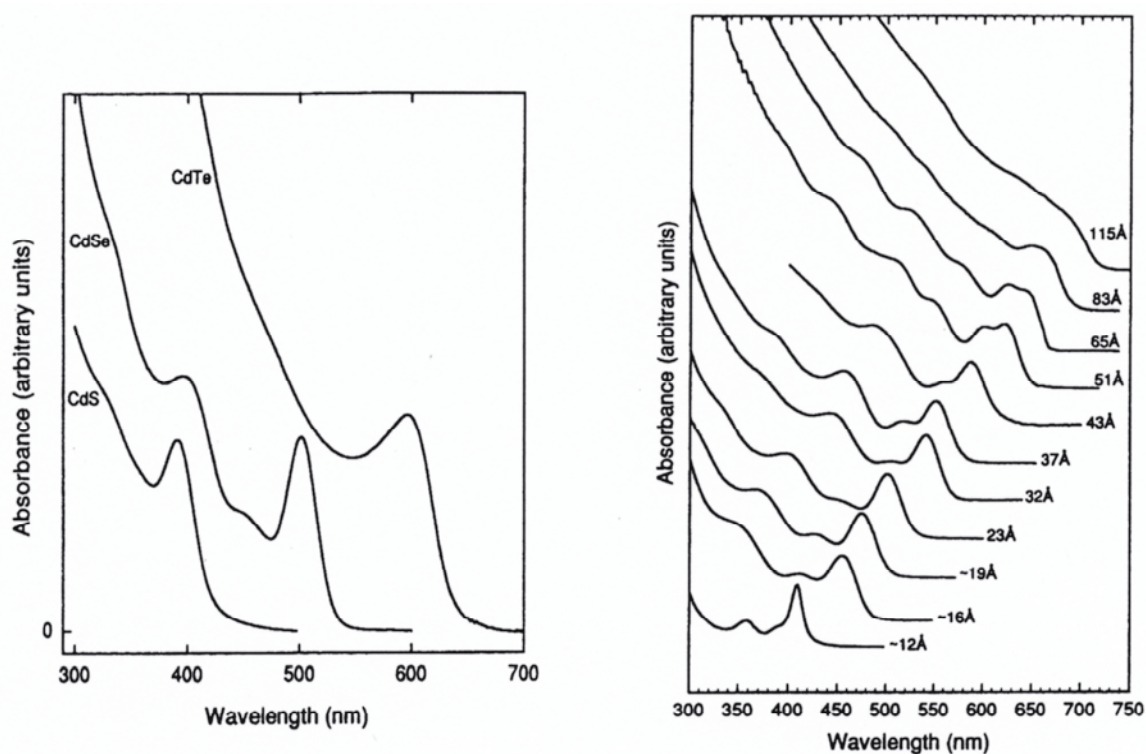


Figure 36. Optical spectra of Cd-X nanoparticles. Left: Effect of composition. Right: Effect of particle size. Quantum confinement effects create the shift in absorption edge. After Murray et al. (1993).

state lifetimes and modes of energy transfer within the structure. Examples of this are photoluminescence of ZnS nanoparticles studied by Wu et al. (1994), and Mn^{2+} doped ZnS nanoparticles by Bhargava et al. (1994). In the latter study, the doped nanocrystals were found to have higher quantum efficiency for fluorescence emission than bulk material, and a substantially smaller excited state lifetime. In the case of environmental nanoparticles of iron and manganese oxides, photoluminescence due to any activator dopant would be quenched by magnetic coupling and lattice vibrations. This reduces the utility of photoluminescence studies to excited state lifetimes due to particle-dopant coupling of various types. The fluorescence of uranyl ion sorbed onto iron oxides has been studied in this way, but not as a function of particle size.

Raman spectroscopy is an optical technique that can give information both on local vibrational states of particular molecular groupings, and on resonances of the entire particle at low frequencies that can be used to estimate particle size (Turkovic et al. 1997). Raman studies have been used to characterize capping materials on nanoparticles, but use of Raman to verify nanoparticle structure, and especially surface structure, has not been thoroughly developed.

Laser induced breakdown detection (LIBD) is a relatively new tool that allows the size distribution of nanoparticles to be determined under dilute conditions where standard optical techniques do not have enough sensitivity. The method is straightforward, and involves setting up a highly focussed laser beam to just below the threshold for plasma formation in the particle medium (generally water). As the threshold energy for breakdown for solids is lower than for liquids, the passage of a colloidal particle into the beam will cause breakdown and the emission of an acoustic wave which can be detected for each breakdown event. The acoustic wave energy is related to particle size, and thus

by thorough sampling one can build up a knowledge of the distribution of sizes in a colloid or nanoparticle solution (Bundschuh et al. 2001).

Soft X-ray spectroscopy

At wavelengths shorter than UV, photons are identified as having ‘vacuum ultraviolet’ or VUV energies (>10 eV). Still shorter wavelengths are called ‘soft’ X-rays up to about a few KeV. VUV-soft X-ray spectroscopy is ideal for probing the electronic structure of materials by a wide variety of methods due to the inherent fine structure for absorption edges and valence band spectra at these energies, and the high energy resolution available with grating spectrometers. In particular, density of state calculations for nanoparticles and for nanoparticle surfaces can be examined by direct observation and compared to theoretical calculations. This is an enormous field of research encompassing a large number of experimental technologies, and almost an equal number of theoretical and semi-empirical analysis methodologies. The greatest amount of work in this field has been done on nanoparticulate thin-film semiconductor materials, although dispersed nanoparticulates have also been examined. Examples of the type of work possible is shown in Figures 37 and 38. One question about nanoparticles has been how they react structurally to the effects of large surface forces, such as high effective confining pressures. Hamad et al. (1999) collected soft X-ray Cd and In spectra at the $M_{4,5}$ edges that showed a continuous broadening of features as particle size decreased (Fig. 37). This seemingly goes against the expected trend of spectral structure becoming more clarified and sharp as molecular dimensions are approached. From comparison of the XPS and edge spectra, where the former shows much less broadening, it was deduced that the broadening is due to the final electronic state rather than the core state (initial state). This implies that the broadening is due to aspects of the crystal structure which affect bonding

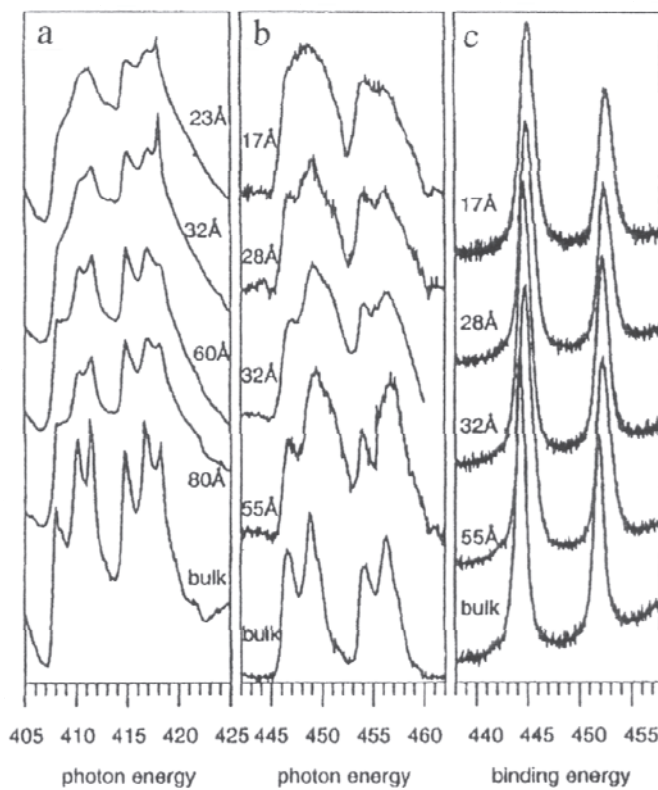


Figure 37. Soft X-ray spectra of (a) Cd and (b) In $M_{4,5}$ edges compared to (c) In 3d XPS spectra. Strong effects of particle size are seen in the soft X-ray edge structure. After Hamad et al. (1999).

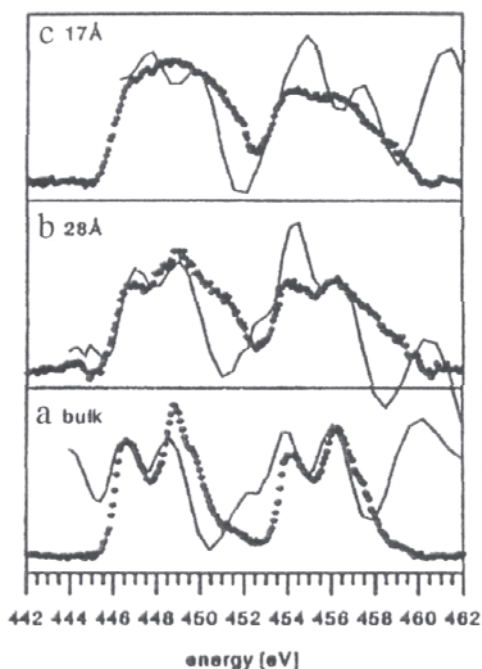


Figure 38. Multiple scattering calculation of the soft X-ray spectrum of different sizes of spherical InAs nanoparticles and InAs bulk (solid lines). The Feff 7 calculations reproduce major features and broadening, but do not model the details well. After Hamad et al. (1999).

electrons. In order to model this effect, Hamad et al (1999) used a multiple scattering calculation based on a nanocrystallite model with relaxed surface bond angles. Such relaxation leads to breakdown of symmetry and an increase in the types of multiple-scattering paths (see XANES discussion earlier) and ultimately to a blurring due to the diversity of unresolvable MS states (Fig. 38). Much less work has been done in soft X-ray spectroscopy of insulators, and essentially none for mineralogical nanomaterials. However, the soft X-ray spectra of anatase (TiO_2) was studied both as bulk and 20-nm nanoparticles by Hwu et al. (1997). These authors found energy shifts and intensity changes on the Ti $L_{2,3}$ edge spectra compared to a rutile (TiO_2) spectrum, but little broadening relative to bulk material on either the Ti $L_{2,3}$ or O K edges. In their case it seems as though the anatase nanocrystals are very little modified from the bulk phase.

Although VUV-soft X-ray techniques yield considerable information on valence and overall electronic structure, they have traditionally been useable only under vacuum conditions (and generally UHV conditions). This means that nanomaterials prepared by aqueous methods must be dried before spectroscopy can be performed, which can seriously affect the nature of the surface chemistry, surface structure and aggregation state. For this reason attempts are being made to develop facilities capable of performing these spectroscopic techniques under environmental conditions, e.g., 20 torr H_2O partial pressure. This is a critical need for studies of geological and soil-related nanomaterials. Such ‘high pressure’ studies can be accomplished in two ways, by use of differential pumping techniques to allow the higher pressure at the sample, but reduced pressure over the rest of the spectrometer, and by using photon-only methodology. The lower pressure is needed to allow electrons ejected from the sample to be measured (e.g., in photoemission studies) or allow passage of very highly absorbed photons. A promising technology is the use of emission spectroscopy to obtain valence structure. A recent general review of much soft X-ray spectroscopy and emission spectroscopy covers the issues in much detail (de Groot 2001).

Mössbauer/NMR spectroscopy

Resonance gamma ray spectroscopy is a powerful technique for the determination of

perturbations to the nuclear spin state levels of certain nuclei. It yields similar information to NMR, but is applicable to magnetic systems, and does not generally require the use of strong external magnetic fields. Mössbauer spectroscopy is especially useful for studies of the state of Fe in materials, and has been used extensively in the study of fine particulate magnetic behavior. This technology is explained in detail in the chapter by Rancourt. NMR is a powerful tool for determination of coordination numbers for ^{29}Si species in glasses and fine particles. Relatively new is the use of ^{17}O NMR spectra to define structural linkages in nanoparticles and small titanium oxo clusters, and yield insight into surface Ti-oxygen species (Scolan et al. 1999).

SOME OUTSTANDING ISSUES

Can crystal chemistry systematics be applied to nanoparticles?

Crystal chemical rules have been applied successfully to glass structure and to small units of structure used as models of larger structures. In both cases the rules seem to apply about as well as with extended bulk solids. Burdett et al. (1981) and Burdett and McLarnan (1984) have made an effort to explain some crystal chemical concepts (including the Pauling rules) in terms of modern bonding and quantum theory, with good success. Hence there ought not to be anything inherently difficult in treating nanoparticles much like other crystalline solids. What has yet to be tested is the use of crystal chemical rules to describe surface structures, an aspect crucial to nanocrystal structure, but this is limited by our knowledge of surfaces in the absolute sense. For example, bond valence analysis was used earlier to discuss how a surface might relax with oxygen termination and protonation. At present we have few reliable studies that show if such changes occur and the magnitude of them. Hence we cannot yet test our systematics for accurate predictions.

Can we meaningfully compare nanoparticle surfaces with bulk crystal surfaces (i.e., are nanoparticles just like small units of a bulk crystal surface)?

We know already that nanocrystals do not behave like large surfaces for several reasons: The bulk electrostatics for a small crystallite differs from that of a large flat plate, and the surface energy is not independent of crystallite size. These issues may mean that considerable rethinking of our electrical double layer modeling is required for nanocrystallite surfaces. Also the structure of a small crystallite will be affected by processes that are much slower or nonexistent in large crystal surfaces, such as Ostwald ripening, atomic rearrangements, strain effects and quantum effects. This means we must be cautious in comparing large crystal surfaces with nanocrystal surfaces of the same nominal composition. However, it is important to understand how mineral surface structure and reactivity are altered by size reduction, and this can be approached from both limiting cases: baseline structure and reactivity from the large single crystal surface, and molecular reassembly and dynamics from small molecular clusters.

Is the local structure of water different near nanoparticles? Is this significant in defining nanoparticle surface/bulk structure and perhaps stability?

Water structure differs markedly from the bulk at surfaces, and for crystallites on the order of 1 nm there could be significant structure enforced by strong hydrophilic or hydrophobic interactions. On large surfaces there is evidence for water restructuring and possible densification, both of which damp out with a few nm distance from the surface. Models have also predicted high diffusivity along the surface that is significantly smaller than diffusive mixing in the "layers" or partially ordered water normal to the interface. For small nanoparticles it is possible that solvation structures (see e.g., Israelachvili

1992), more common about highly charged molecules in aqueous solution, might modify the water structure. Water can form certain arrangements of cage-like solvation environments, and these might be favored by particular surface charges, particle diameters and surface terminations. Is it also important to consider the action of hydrogen bonding at nanocrystal surfaces in stabilizing surface structure.

Just as certain molecules are able to passivate the surfaces of semiconducting nanocrystals, water may act as an effective stabilizing agent with certain size nanocrystals under the right conditions.

Do highly defective structures have aspects in common with nanoparticles?

For example: Do “nanoporous materials” have similarities to clustered nanoparticles either structurally or energetically?

It is possible that many of the poorly crystallized structures found in natural environments are better defined as aggregates of nanoparticles, than as defective crystal structures. In fact, it is the general desire to define structures within the context of the latter case that limits our openness to consider aggregated and perhaps somewhat recrystallized materials as the stable (or long term metastable) form of minerals. Very critical to dealing with these issues are the thermodynamic properties and reaction kinetics on the molecular scale at the water-mineral interface, most of which are still unavailable and daunting to obtain. An interesting case is ferrihydrite which has seen detailed study to understand its not only defective, but also highly variable microstructure and crystal structure (Drits et al. 1993; Manceau and Drits 1993; Drits et al. 1993).

Outstanding problems that need to be addressed

This chapter has touched on a few of the problems associated with nanoparticle and nanocrystal structure, growth and stability. There is a wide gap in our knowledge of how nanoparticles in the environment form, aggregate and otherwise react. The molecular-level aspects of surface structures, non-stoichiometry, surface relaxation, passivation and surface water structure and dynamics are still being initially explored in simple idealized high purity crystal surfaces. Hence characterization of natural nanoparticle materials will be a consummate challenge for years to come. However we can readily identify areas where study is likely to have important connections for environmental geochemistry. These include sorption and complexation reactions of small Fe- and Mn-oxhydroxides, surface passivation of these and other nanominerals via natural organic phases, oriented aggregation processes as a new pathway for nanocrystallite growth, biomimetic pathways for the organization of nanocrystals and tissues or organic binding agents, and enzymatic alteration of crystal growth, aggregation and crystal structure stability. Fortunately our tools for these investigations have never been more powerful, and the near future holds much promise for excellent advances in our simulation capacity for surface and crystal structure, bonding, growth and electronic structure.

ACKNOWLEDGMENTS

Jill Banfield contributed mightily to the content of this chapter, and I thank her for many discussions, suggestions, and for initial review. Discussions with Jim Rustad, Hoi-Ying Holman and David Shuh were also most helpful. Carol Taliaferro helped with finalizing corrections to figures, figure captions, references and text. This project was supported by the Office of Science, Office of Basic Energy Sciences, Division of Chemical Sciences, Geosciences Research Program of the U.S. Department of Energy under contract DE-AC03-76-SF00098, and by LDRD funding from Lawrence Berkeley National Laboratory.

REFERENCES

- Abruna HD (1991) X-ray Absorption Spectroscopy in the Study of Electrochemical Systems. *In* Electrochemical Interfaces. Abruna HD (ed) VCH Publishers, New York
- Albertini G, Carsughi F, Casale C, Fiori F, La Monaca A, Musci M (1993) X-ray and neutron small-angle scattering Investigation of nanophase vanadium-titanium oxide particles. *Phil Mag B* 68:949-955
- Alexandrowicz Z (1993) How to reconcile classical nucleation theory with cluster-cluster aggregation. *Physica A* 200:250-257
- Alivisatos AP (1997) Scaling law for structural metastability in semiconductor nanocrystals. *Ber Bunsenges Phys Chem* 101:1573-1577
- Auer S, Frenkel D (2001) Prediction of absolute crystal-nucleation rate in hard-sphere colloids. *Nature* 409:1020-1023
- Azaroff LV (1968) *Elements of X-ray Crystallography*. McGraw-Hill, New York
- Banfield JF, Welch SA, Zhang H, Ebert TT, Penn RL (2000) Aggregation-based crystal growth and microstructure development in natural iron oxyhydroxide biomineralization products. *Science* 289:751-754
- Benaissa M, Jose-Yacamán M, Xiao TD, Strutt PR (1997) Microstructural study of hollandite-type MnO₂ nano-fibers. *Appl Phys Letters* 70:2120-2122
- Bhargava RN, Gallagher D, Hong X, Nurmikko A (1994) Optical properties of manganese-Doped nanocrystals of ZnS. *Phys Rev Letters* 72:416-419
- Bish DL, Post JE (eds) (1989) *Modern Powder Diffraction*. Reviews in Mineralogy vol 20, 369 p. Mineralogical Society of America, Washington, DC
- Becker R, Döring W (1935) Kinetische behandlung der Keimbildung in übersättigten Dispersionen. *Ann Phys* 24:719-752
- Brasher LL, Kaler EW (1996) A small-angle neutron scattering (SANS) contrast variation investigation of aggregate composition in cationic surfactant mixtures. *Langmuir* 12:6270-6276
- Brown GE Jr, Heinrich VE, Casey WH, Clark DL, Eggleston C, Felmy A, Goodman DW, Grätzel M, Maciel G, McCarthy MI, Nealon KH, Sverjensky DA, Toney MF, Zachara JM (1999) Metal oxide surfaces and their interactions with aqueous solutions and microbial organisms. *Chem Rev* 99:77-174
- Brown GE Jr., Calas G, Waychunas GA, Petiau J (1988) X-ray absorption spectroscopy: Applications in mineralogy and geochemistry. *Rev Mineral* 18:431-512
- Brown ID, Shannon RD (1973) Empirical bond-strength-bond-length curves for oxides. *Acta Crystallogr A* 29:266-282
- Bundschuh T, Knopp R, Kim JI (2001) Laser-induced breakdown detection (LIBD) of aquatic colloids with different laser systems. *Colloids Surfaces A* 177:47-55
- Burdett JK, McLarnan TJ (1984) An orbital interpretation of Pauling's rules. *Am Mineral* 69:601-621
- Burdett JK, Price GD, Price SL (1981) The factors influencing solid state structure. An interpretation using pseudopotential radii maps. *Phys Rev B* 24:2903-2912
- Calas G, Brown GE Jr, Waychunas GA, Petiau J (1987) X-ray absorption spectroscopic studies of silicate glasses and minerals. *Phys Chem Minerals* 15:19-29
- Carter A, Bouldin CE, Kemner KM, Bell MI, Woicik JC, Majetich SA (1997) Surface structure of cadmium selenide nanocrystallites. *Phys Rev B* 55:13822-13828
- Caruso F (2001) Nanoengineering of Particle Surfaces. *Adv Mater* 13:11-22
- Casanove M-J, Lecante P, Snoeck E, Mosset A, Roucau C (1997) HREM and WAXS study of the structure of metallic nanoparticles. *J Physique III* 7:505-515
- Chen LX, Rajh T, Jäger W, Nedeljkovic J, Thurnauer MC (1999) X-ray absorption reveals surface structure of titanium dioxide nanoparticles. *J Synch Rad* 6:445-447
- Cheng B, Kong J, Luo J, Dong Y (1993) *Materials Science Progress* 7:240-243 (in Chinese)
- Chu B, Liu T (2000) Characterization of nanoparticles by scattering techniques. *J Nanoparticle Res* 2:29-41
- Clem PJ, Fisher JC (1958) *Acta Metall* 3:347
- Connolly S, Fullam S, Korgel B, Fitzmaurice D (1998) Time-resolved small-angle X-ray scattering studies of nanocrystal superlattice self-assembly. *J Am Chem Soc* 120:2969-2970
- deGroot F (2001) High-resolution X-ray emission and X-ray absorption spectroscopy. *Chem Rev* 101:1779-1808
- Davis JA, Kent DB (1990) Surface complexation modeling in aqueous geochemistry. *Rev Mineral* 23:177-260
- Derjaguin BV (1934) Untersuchungen über die Reibung und Adhäsion. *Kolloid Zeits* 69:155-164
- Drits VA, Sakharov BA, Manceau A (1993) Structure of ferrihydrite as determined by simulation of X-ray diffraction. *Clay Mineral* 28:209-222
- Drits VA, Sakharov BA, Salyn, AL and Manceau A (1993) Structural model for ferrihydrite. *Clay Mineral* 28:185-207

- Edelstein AS, Cammarata RC (1996) *Nanomaterials: Synthesis, Properties and Applications*. Institute of Physics, Bristol, UK
- Eden M (1961) A two-dimensional growth process. 4th Berkeley Symp Math, Stat, Prob 4:223-239
- Eng PJ, Trainor TP, Brown GE, Waychunas GA, Newville M, Sutton SR, Rivers ML (2000) Structure of the hydrated α -Al₂O₃ (0001) surface. *Science* 288:1029-1033
- Frenkel AI (1999) Solving the structure of nanoparticles by multiple-scattering EXAFS analysis. *J Synch Rad* 6:293-295
- Fritsche H-G, Buttner T (1999) Modification of the lattice contraction of small metallic particles by chemical and/or geometrical stabilization. *Z Phys Chem* 209:93-101
- Gao P, Gleiter H (1987) High resolution electron microscope observation of small gold particles. *Acta Metall* 35:1571-1575
- Glusker JP, Trueblood KN (1985) *Crystal Structure Analysis*. 2nd edition. Oxford Univ Press, Oxford, UK
- Gnutzmann V, Vogel W (1990) Surface oxidation and reduction of small platinum particles observed by *in situ* X-ray diffraction. *Z Physik D (Atoms, Molecules, Clusters)* 12:597-600
- Greenwood NN (1970) *Ionic Crystals Lattice Defects and Nonstoichiometry*. Butterworths, London
- Guinier A (1963) *X-ray Diffraction in Crystals, Imperfect Crystals, and Amorphous Bodies*. W H Freeman, San Francisco
- Hadjipanayis GC, Siegel RW (1994) *Nanophase Materials: Synthesis-Properties-Applications*. NATO ASI Series 260. Kluwer Academic Publ, Dordrecht, The Netherlands
- Halsey TC (2000) Diffusion-limited aggregation: A model for pattern formation. *Phys Today*, Nov 2000, p 36-41
- Hamad KS, Roth R, Rockenberger J, van Buuren T, Alivisatos AP (1999) Structural disorder in colloidal InAs and CdSe nanocrystals observed by X-ray absorption near-edge spectroscopy. *Phys Rev Letters* 83:3474-3477
- Harfenist SA, Wang ZL, Alvarez MM, Vezmar I, Whetten RL (1997) Three-dimensional superlattice packing of faceted silver nanocrystals. *Nanophase and nanocomposite materials II. Mater Res Soc Symp Proc* 457:137-142
- Hartman P (1973) *Crystal Growth: An Introduction*. North-Holland Publishing Co, Amsterdam
- Herring C (1951) Some theorems on the free energies of crystal surfaces. *Phys Rev* 82:87-93
- Hettema H, McFeaters JS (1996) The direct Monte Carlo method applied to the homogeneous nucleation problem. *J Chem Phys* 105:2816-2827
- Hiemenz PC, Rajagopalan R (1997) *Principles of Colloid and Surface Chemistry*, 3rd edition. Marcel Dekker, New York
- Hofmeister H, Huisken F, Kohn B (1999) Lattice contraction in nanosized silicon particles produced by laser pyrolysis of silane. *Eur Phys J D* 9:137-140
- Hwu Y, Yao YD, Cheng NF, Tung CY, Lin HM (1997) X-ray absorption of nanocrystal TiO₂. *Nanostruc Mater* 9:355-358
- Hyeon-Lee J, Beaucage G, Pratsinis SE, Vemury S (1998) Fractal analysis of flame-synthesized nanostructured silica and titania powders using small-angle X-ray scattering. *Langmuir* 14:5751-5756
- Israelachvili JN (1991) *Intermolecular and Surface Forces*, 2nd edition. Academic Press, New York
- Israelachvili JN, Pashley RM (1982) The hydrophobic interaction is long range decaying exponentially with distance. *Nature* 300:341-342
- Kaszuba M (1999) The measurement of nanoparticles using photon correlation spectroscopy and avalanche photodiodes. *J Nanoparticle Res* 1:405-409
- Khanna SN, Bucher JP, Buttet J, Cyrot-Lackmann F (1983) Stability and lattice contraction of small platinum particles. *Surface Sci* 127:165-174
- Kirkpatrick RJ (1981) Kinetics of crystallization of igneous rocks. *Rev Mineral* 8:321-398
- Klug HP, Alexander LE (1974) *X-ray Diffraction Procedures*, 2nd edition. Wiley Interscience, New York
- Kortright J, Warburton W, Bienenstock A (1983) Anomalous X-ray scattering and its relationship to EXAFS. *Springer Ser Chem Phys* 27:362-372
- Krill CE, Ehrhardt H, Birringer R (1997) Grain-size stabilization in nanocrystalline materials. *In Chemistry and Physics of Nanostructures and Related Non-Equilibrium Materials*. Ma E, Fultz B, Shull R, Morral J, Nash P (eds) Minerals, Metals and Materials Society, Warrendale, Pennsylvania
- Lee PA, Citrin PH, Eisenberger P (1981) Extended X-ray absorption fine structure—its strengths and limitations as a structural tool. *Rev Mod Phys* 53:769-806
- Li D-H, Ganczarczyk J (1989) Fractal geometry of particle aggregates generated in water and wastewater treatment processes. *Environ Sci Technol* 23:1385-1389
- Li JC, Ross DK, Howe LD, Stefanopoulos KL, Fairclough JPA, Heenan R, Ibel K (1994) Small-angle neutron-scattering studies of the fractal-like network formed during desorption and adsorption of water in porous materials. *Phys Rev B* 49:5911-5917

- Liu J (2000) Scanning transmission electron microscopy of nanoparticles. *In* Characterization of Nanophase Materials. Wang ZL (ed) p 81-132. Wiley-VCH, Weinheim, FRG
- Linford RG (1973) Surface thermodynamics of solids. *In* Green M (ed) Solid State Surface Science 2: p 1-152. Dekker, New York
- Mahanty J, Ninham BW (1976) Dispersion Forces. Academic Press, New York
- Manceau A, Drits VA (1993) Local structure of ferrihydrite and ferroxhyte by EXAFS spectroscopy. *Clay Mineral* 28:165-184
- Marasll N, Hunt JD (1998) The use of measured values of surface energies to test heterogeneous nucleation theory. *J Crystal Growth* 191:558-562
- Martin JE, Wilcoxon JP, Odinek J, Provencio P (2000) Control of interparticle spacing in gold nanoparticle superlattices. *J Phys Chem B* 104:9475-9486
- McGrath KM (2001) Probing material formation in the presence of organic and biological molecules. *Adv Mater* 13:989-992
- Meakin P (1992) Aggregation kinetics. *Physica Scripta* 46:295-331
- Milligan WW, Hackney SA, Ke M, Aifantis EC (1993) *In situ* studies of deformation and fracture in nanophase materials. *Nanostruct Mater* 2:267-276
- Miranda Salvado IM, Margaca FMA, Teixeira J (1996) Structure of mineral gels. *J Molec Struct* 383: 271-276
- Montano P, Shenoy GK, Alp EE, Schulze W, Urban J (1986) Structure of copper microclusters isolated in solid argon. *Phys Rev Letters* 56:2076-2079
- Murray CB, Kagan CR, Bawendi MG (1995) Self organization of CdSe Nanocrystallites into three-dimensional quantum dot superlattices. *Science* 270:1335-1338
- Murray CB, Norris DJ, Bawendi MG (1993) Synthesis and characterization of nearly monodisperse CdE (E=S, Se, Te) Semiconductor nanocrystallites. *J Am Chem Soc* 115:8706-8715
- Nanda KK, Behera SN, Sahu SN (2001) The lattice contraction of nanometre-sized Sn and Bi particles produced by an electrochemical technique. *J Phys Condens Matter* 13:2861-2864
- Nikolakis V, Kokkoli E, Tirrell M, Tsapatsis M, Vlachos DG (2000) Zeolite growth by addition of subcolloidal particles: modeling and experimental validation. *Chem Mater* 12:845-853
- Onodera SJ (1992) Lattice parameters of fine copper and silver particles. *J Phys Soc Japan* 61:2191-2193
- Ostwald W (1897) Studien über die Bildung und Umwandlung fester Körper. *Z Phys Chemie* 22:289-330
- Pecora R (2000) Dynamic light scattering measurements of nanometer particles in liquids. *J Nanoparticle Res* 2:123-131
- Penn RL, Banfield JF (1999) Morphology development and crystal growth in nanocrystalline aggregates under hydrothermal conditions: Insights from titania. *Geochim Cosmochim Acta* 63:1549-1557
- Penn RL, Banfield JF (1998a) Imperfect oriented attachment: dislocation generation in defect-free nanocrystals. *Science* 281:969-971
- Penn RL, Banfield JF (1998b) Oriented attachment and growth, twinning, polytypism, and formation of metastable phases: Insights from nanocrystalline TiO₂. *Am Mineral* 83:1077-1082
- Post JE, Bish DL (1989) Rietveld refinement of crystal structures using powder X-ray diffraction data. *Rev Mineral* 20:277-308
- Raghaven V, Cohen M (1975) Solid-state phase transformations. *In* Hannay NB (ed) Treatise on Solid State Chemistry 5:67-128
- Reinhard D, Hall BD, Berthoud P, Valkealahti S, Monot R (1998) Unsupported nanometer-sized copper clusters studied by electron diffraction and molecular dynamics. *Phys Rev B* 58:4917-4926
- Reinhard D, Hall BD, Berthoud P, Valkealahti S, Monot R (1997) Size-dependent icosahedral-to-fcc structure change confirmed in unsupported nanometer-sized copper clusters. *Phys Rev Letters* 79:1459-1462
- Reddy M, Reddy G, Manorama SV (2001) Preparation, characterization, and spectral studies on nanocrystalline anatase TiO₂. *J Solid State Chem* 158:180-186
- Rieker T, Hanprasopwattana A, Datye A, Hubbard P (1999) Particle size distribution inferred from small-angle X-ray scattering and transmission electron microscopy. *Langmuir* 15:638-641
- Rietveld HM (1969) A profile refinement method for nuclear and magnetic structures. *J Appl Crystallogr* 2:65-71
- Rockenberger J, Tröger L, Rogach AL, Tischer M, Grundmann M, Eychmüller A, Weller H (1998) The contribution of particle core and surface to strain, disorder and vibrations in thiolcapped CdTe nanocrystals. *J Chem Phys* 108:7807-7815
- Rockenberger J, Tröger L, Kornowski A, Vossmeier T, Eychmüller A, Feldhaus J, Weller H (1997) EXAFS Studies on the size-dependence of structural and dynamic properties of CdS nanoparticles. *J Phys Chem B* 101:2691-2701
- Sayers DE, Lytle FW, Stern EA (1970) Point scattering theory of X-ray K absorption fine structure. *Adv X-ray Analysis* 13:248-271

- Sayers DE, Stern EA, Lytle FW (1971) New technique for investigating noncrystalline structures: Fourier analysis of the extended X-ray absorption structure. *Phys Rev Letters* 27:1204-1207
- Sayle DC, Watson GW (2000) Simulated amorphisation and recrystallization: Nanocrystallites within meso-scale supported oxides. *J Mater Chem* 10:2241-2243
- Scherrer P (1918) *Nachr Göttinger Gesell* 98
- Schreyer D, Chatelain A (1985) Lattice contraction in small particles of $\text{SrCl}_2:\text{Gd}^{3+}$: explicit size effect in EPR and Raman spectroscopy. *Surface Sci* 156:712-719
- Schultz JM (1982) *Diffraction for Materials Scientists*. Prentice-Hall, Englewood Cliffs, NJ
- Schwartz LH, Cohen JB (1987) *Diffraction from Materials*. Springer-Verlag, Berlin
- Scolan E, Magnenet C, Massiot D, Sanchez C (1999) Surface and bulk characterization of titanium-oxo clusters and nanosized titania particles through ^{17}O solid state NMR. *J Mater Chem* 9:2467-2474
- Sekerka RF (1993) Role of instabilities in determination of the shapes of growing crystals. *J Crystal Growth* 128:1-12
- Sekerka RF (1973) Morphological stability. In *Crystal Growth: An Introduction*. Hartman P (ed) p 403-443. North-Holland Publishing Co, Amsterdam
- Singer PC, Stumm W (1970) Acidic mine drainage. *Science* 167:1121-1123
- Smoluchowski MV (1918) Versuch einer mathematischen Theorie der koagulationskinetik kolloider Lösungen. *Z Phys Chemie* 92:129-168
- Sposito G (1984) *The Surface Chemistry of Soils*. Oxford :University Press, New York
- Stanley HE, Ostrowsky N (1986) *On Growth and Form*. NATO ASI Ser E: Applied Sciences, vol 100. Kluwer Academic Publ, Dordrecht, The Netherlands
- Stumm W (1987) *Aquatic Surface Chemistry*. John Wiley, New York
- Sun S, Murray CB (1999) Synthesis of monodisperse cobalt monocrystals and their assembly into magnetic superlattices. *J Appl Phys* 85:4325-4330
- Sutherland DN (1970) Chain formation of fine particle aggregates. *Nature* 226:1241-1242
- Suzuki Y, Banfield JF (1999) Geomicrobiology of uranium. *Rev Mineral* 38:393-432
- Talanquer V, Oxtoby DW (1994) Dynamical density functional theory of gas-liquid nucleation. *J Chem Phys* 100:5190-5200
- Thomas DN, Judd SJ, Fawcett N (1999) Flocculation modelling: A review. *Water Res* 33:1579-1592
- Thomas JG, Siegel RW, Eastman JA (1990) Grain boundaries in nanophase palladium: high resolution electron microscopy and image simulation. *Scripta Metall Mater* 24:201-206
- Thurn-Albrecht T, Meier G, Muller-Buschbaum P, Patkowski A, Steffen W, Grubel G, Abernathy DL, Diat O, Winter M, Koch MG, Reetz MT (1999) Structure and dynamics of surfactant-stabilized aggregates of palladium nanoparticles under dilute and semidilute conditions: Static and dynamic X-ray scattering. *Phys Rev E* 59:642-649
- Tranquanda JM, Ingalls R (1983) Extended X-ray-absorption fine-structure study of anharmonicity in CuBr. *Phys Rev B* 28:3520-3528
- Tsunekawa S, Ito S, More T, Ishikawa K, Li Z-Q, Kawazoe Y (2000a) Critical size and anomalous lattice expansion in nanocrystalline BaTiO_3 particles. *Phys Rev B* 62:3065-3070
- Tsunekawa S, Ishikawa K, Li Z-Q, Kawazoe Y, Kasuya A (2000b) Origin of anomalous lattice expansion in oxide nanoparticles. *Phys Rev Letters* 85:3440-3443
- Turkovic A, Ivanda M, Popovic S, Tonejc A, Gotic M, Dubcek P, Music S (1997) Comparative Raman, XRD, HREM and SAXS studies of grain sizes in nanophase TiO_2 . *J Molec Struct* 410/411:271-273
- ten Wolde PR, Frenkel D (1997) Enhancement of protein crystal nucleation by critical density fluctuations. *Science* 277:1975-1978
- Verwey EJW, Overbeek JTG (1948) *Theory of the Stability of Lyophobic Colloids*. Elsevier, Amsterdam
- Volmer M, Weber A (1925) Klimbildung in übersättigten gebilden. *Z Phys Chem* 119:277-301
- Wadsley AD (1963) Inorganic nonstoichiometric compounds. In *Mandelcorn L (ed) Nonstoichiometric Compounds*. Academic Press, New York
- Wang ZL (2000) *Characterization of Nanophase Materials*. Wiley-VCH, Weinheim, FRG
- Warren BE (1969) *X-ray Diffraction*. Addison-Wesley, Reading, Massachusetts
- Warren BE, Averbach BL (1950) The effect of cold-work distortion on X-ray patterns. *J Appl Phys* 21:595-599
- Waychunas GA (1987) Synchrotron radiation XANES spectroscopy of Ti in minerals: Effects of Ti bonding distances, Ti valence, and site geometry on absorption edge structure. *Am Mineral* 72:89-101
- Waychunas GA, Fuller CC, Davis JA, Rehr JJ (2001) Surface complexation and precipitate geometry for aqueous Zn(II) sorption on ferrihydrite: II. XANES analysis. *Geochim Cosmochim Acta* (in press)
- Waychunas G, Davis J, Reitmeyer R (1999) GIXAFS study of Fe^{3+} sorption and precipitation on natural quartz surfaces. *J Synchrotron Rad* 6:615-617

- Waychunas GA, Fuller CC, Rea BA, Davis JA (1996) Wide angle X-ray scattering (WAXS) study of "two-line" ferrihydrite structure: Effect of arsenate sorption and counterion variation and comparison with EXAFS results. *Geochim Cosmochim Acta* 60:1765-1781
- Weissmuller J (1996) Characterization by scattering techniques and EXAFS. *In* *Nanomaterials: Synthesis, Properties and Applications*. Edelstein AS, Cammarata RC (eds) p 219-276. Institute of Physics Bristol, UK
- Wilson AJC (1963) *Mathematical Theory of X-ray Powder Diffraction*. Philips Technical Library, Eindhoven, The Netherlands
- Wu M, Gu W, Li W, Zhu X, Wang F, Zhao S (1994) Preparation and characterization of ultrafine zinc sulfide particles of quantum confinement. *Chem Phys Letters* 224:557-562
- Wulff G (1901) Zur Frage der Geschwindigkeit des Wachstums und der Auflösung der Krystallflächen. *Z Kristallogr* 34:449-530
- Witten TA, Sander LM (1981) Diffusion-limited aggregation, a kinetic critical phenomenon. *Phys Rev Letters* 47:1400-1403
- Xiao TD, Strutt PR, Benaissa M, Chen H, Kear BH (1998) Synthesis of high active-site density nanofibrous MnO₂-base materials with enhanced permeabilities. *Nanostruct Mater* 10:1051-1061
- Yeadon M, Ghaly M, Yang JC, Averback RS, Gibson JM (1998) "Contact epitaxy" observed in supported nanoparticles. *Appl Phys Letters* 73:3208-3210
- Yin JS, Wang ZL (1997) Ordered self-assembling of tetrahedral oxide nanocrystals. *Phys Rev Letters* 79:2570-2573
- Young RA (1993) *The Rietveld Method*. Oxford University Press, Oxford, UK
- Zanetti D, Hall BD, Ugarte D (2000) X-ray Characterization of Nanoparticles. *In* *Characterization of Nanophase Materials*. Wang ZL (ed) p 13-36. Wiley-VCH, Weinheim, FRG
- Zangwill A (1988) *Physics at Surfaces*. Cambridge University Press, Cambridge, UK
- Zhang H, Banfield JF (2000) Understanding polymorphic phase transformation behavior during growth of nanocrystalline aggregates: insights from TiO₂. *J Phys Chem B* 104:3481-3487
- Zhao J, Huggins FE, Feng Z, Huffman GP (1994) Ferrihydrite: Surface structure and its effects on phase transformation. *Clays Clay Minerals* 42:737-746
- Zoltai T, Stout JH (1984) *Mineralogy: Concepts and Principles*. Burgess Publishing, Minneapolis, Minnesota